Doctoral Dissertation

Doctoral Program in Civil and Environmental Engineering (36th Cycle)

Finite Fracture Mechanics and Phase Field Models for Predicting Fatigue, Fracture and Debonding in Composite Structures

By

Amir Mohammad Mirzaei

******

Supervisors:
Prof. Pietro Cornetti, Supervisor
Prof. Alberto Sapora, Co-Supervisor

Doctoral Examination Committee:
Prof. A. Doitrand, INSA Lyon
Prof. P. Lonetti, Università della Calabria
Prof. M.R. Ayatollahi, Iran University of Science and Technology
Prof. A. Campagnolo, Università di Padova
Prof. M. Borri Brunetto, Politecnico di Torino

Politecnico di Torino
2024

Declaration

I hereby declare that the contents and organization of this dissertation constitute my own original work and does not compromise in any way the rights of third parties, including those relating to the security of personal data.

Amir Mohammad Mirzaei

2024

* This dissertation is presented in partial fulfillment of the requirements for **Ph.D. degree** in the Graduate School of Politecnico di Torino (ScuDo).

I would like to dedicate this thesis to my loving wife, Sara, and my supportive parents.

Acknowledgment

In expressing my heartfelt gratitude, I extend my sincerest thanks to Prof. Pietro Cornetti, whose expertise, understanding, and kindness added considerably to my experience as a PhD student. His willingness to give his time so generously has been very much appreciated. I am indebted to his invaluable guidance throughout this journey, which was not only instrumental in shaping this thesis but also profoundly influential in my personal and professional growth. Last but not least, I sincerely appreciate the trust, freedom, and support that Prof. Pietro Cornetti gave me during the project.

I would also like to extend my profound gratitude to Prof. Alberto Sapora for his invaluable co-supervision and support throughout my doctoral studies. His meticulous attention to detail has significantly contributed to the refinement of my work. His contributions have been pivotal not only to the success of my thesis but also to my development as a researcher and thinker.

I extend my sincere appreciation to Prof. Majid Reza Ayatollahi for his invaluable guidance during my Master's program. His mentorship was instrumental in shaping my approach to research and significantly enhanced my skills as a researcher. I am grateful for his commitment to excellence and his role in fostering my academic development.

I am deeply grateful to Prof. Rasul Bagheri for his mentorship during my undergraduate studies, particularly for guiding me through the process of writing my first research paper, an experience that laid the foundation for my academic writing skills.

I extend my profound gratitude to Prof. De Lorenzis for her guidance and mentorship during my secondment at ETH Zurich. Her expertise and insights have enriched my research experience, particularly in numerical analyses.

I appreciate Mr. Bernardo López Romano’s support during my industrial secondment at FIDAMC (Fundación para la Investigación, Desarrollo y Aplicación de Materiales Compuestos), Madrid.

Finally, I acknowledge the funding from the European Union’s Horizon 2020 research and innovation program under the Marie Skłodowska-Curie grant agreement No 861061 – NEWFRAC Project.

Abstract

The applications of composite materials and structures have recently risen due to their exceptional mechanical properties and multifunctional capabilities. Nevertheless, a thorough analysis of their failure mechanisms, particularly under complex loading conditions, remains a significant challenge. Fatigue, as the most common failure mode in real-world structures, encompasses these complex conditions and continues to be a focal point of research. Precise estimation of fatigue life is essential for the design and maintenance of mechanical systems and structures, as it determines the maximum loading cycles a material can endure before failure. The primary aim of this thesis is to study fatigue and fracture of composite structures. Conventional methods addressing this issue often suffer from being time-consuming, lacking universality, or exhibiting reliability concerns. This thesis introduces innovative criteria based on Finite Fracture Mechanics to first analyze debonding failure and then address fatigue failure in composite structures. Additionally, a fatigue analysis leveraging the powerful numerical approach of Phase Field is conducted.

Focusing on composite structures, debonding emerges as a fundamental failure mode influencing the structure's ultimate load-bearing capacity. As a starting point, FFM is employed to analyze debonding behavior in composite structures, specifically in the direct shear test – a pivotal test for understanding debonding in externally bonded systems. A comparison with the cohesive zone models enriches this analysis. Given the presence of geometric discontinuities such as cracks, notches, and holes in mechanical components – whether by design or due to external factors – it is crucial to analyze their role as stress concentrators, affecting the structural durability and functionality. Subsequently, FFM is developed by the author to estimate the finite fatigue life of notched elements in isotropic materials, for the first time. The next step extends the model to assess the fatigue lifetime of notched laminated composites. With a comprehensive experimental campaign on notched carbon fiber laminated composites, validation is performed. Finally, the Phase Field model, having been recently adapted for fatigue, is examined and validated through experimental data to derive the Paris curve, based on available experimental data in the literature.

Regarding the outcomes, for analyzing the debonding in composite materials using direct shear tests, closed-form solutions are proposed to fully study the effect of different parameters. The results highlight the importance of considering residual strength (friction) in the analysis even at debonding onset. The models demonstrate high accuracy in predicting the failure load in experimental data, based on the interface mechanical properties obtained from a single test. Furthermore, to extend FFM to the finite fatigue life regime, the effectiveness of the methodology is first confirmed through various experimental data encompassing a wide range of notch geometries (such as circular holes, U- and V-notches), loading scenarios (including tension and bending), load ratios, and materials (like steel, aluminum, and samples produced through additive manufacturing). Due to the low computational cost of the model, parametric studies on the effect of notch geometry on fatigue life are performed. Then, without relying on any fitting parameters from experimental data and only employing standard tests, as well as utilizing (semi-analytical) stress and energy fields, the FFM model is employed to study the fatigue lifetime of notched orthotropic plates. Despite the complexity of the problem, high accuracy is achieved, and results demonstrate a consistent behavior with the conventional hole size effect, i.e., the number of cycles to failure for a given stress amplitude decreases as the hole radius increases. Finally, the robustness and reliability of the Phase Field approach as a computational tool for predicting the fatigue failure of structures are proved when its results are compared to experimental data. This research paves the way for more efficient and reliable design and maintenance protocols in aerospace, automotive, and civil engineering industries, where the lifetime and safety of composite structures are paramount.

Contents

List of Figures

List of Tables

Chapter 1

Introduction

1.1 Background and motivation

Composite structures are considered one of the most crucial topics in mechanical engineering due to their superior ability to combine strength, stiffness, and lightness. These structures, achieved by layering or joining two or more distinct materials, offer mechanical properties that often surpass those of their individual constituents. This integration enables tailored mechanical behaviors, making such composite configurations indispensable in several engineering applications, ranging from aerospace assemblies to civil infrastructure. However, their complex nature presents unique challenges, particularly in the domain of fatigue, fracture, and debonding. It is worth highlighting that the history of composites stretches back to the very beginnings of human civilization, exemplified by the ancient technique of reinforcing clay with straw to make bricks. On the one hand, joining points—often resulting from the shape of the bond or the mismatch between the mechanical properties of the joined materials—act as stress concentrations and are frequently the most critical points for failure analysis. On the other hand, geometrical discontinuities commonly found in structures, such as holes and notches, act as stress concentrators and can be the hot spots that trigger fractures.

In this thesis, two main approaches called Finite Fracture Mechanics (FFM) and Phase Field are employed to study failure in several problems. FFM is a failure criterion that predicts failure by simultaneously fulfilling stress and energy conditions. It is based on the idea that crack advancement occurs by discrete amount, contrary to the concept of infinitesimal crack growth (Griffith's approach). FFM is especially powerful at handling structures with discontinuities, such as notches. The model was introduced for static loading and later extended to the fatigue limit regime. However, it has not been employed to estimate the finite

fatigue life of structures yet. Besides the physically sound bases, FFM can be easily integrated with analytical solutions to provide results quickly, which is advantageous for parametric studies.

On the other hand, the Phase Field (PF) model is known as a computational approach that employs a gradient-based fracture representation. Some of the advantages of the approach are: (a) eliminating the challenges of explicit crack tracking, (b) robust numerical implementation, (c) handling of arbitrary crack initiation and growth. Although the model has been extended to estimate fatigue loading, its proper validation with experimental data is pending, owing to the approach's high computational demand. In this thesis, the PF model is employed to derive the Paris Curve, utilizing available experimental data.

It is worthwhile to mention that this project received funding from the European Union's Horizon 2020 research and innovation program under the Marie Skłodowska-Curie grant agreement No. 861061 – NEWFRAC Project. The NEWFRAC training network represents a pioneering European initiative aimed at advancing predictive capabilities for failure in heterogeneous systems through a comprehensive computational framework. This framework uniquely integrates Finite Fracture Mechanics and Phase Field modeling strategies, targeting the enhancement of failure prediction across different scales in varied engineering systems. The network offered 13 PhD positions, distributed across a consortium of prestigious academic and industrial institutions in five European countries (France, Germany, Italy, Portugal, and Spain) and two associated countries (Israel and Switzerland), facilitating a multidisciplinary and multisectoral training environment. For more detailed information, you can visit the NEWFRAC Training Network's website at https://www.newfrac.eu/.

Prior to moving to the introduction of the approaches and conducting bibliographical research, this thesis first introduces some common expressions used throughout the thesis. Subsequently, the models themselves are presented.

1.2 Some common definitions in fracture and fatigue

Fracture and fatigue are key concerns in materials science and engineering, playing a crucial role in evaluating structural integrity. Although both concepts deal with how materials fail, they are influenced by different factors.

1.2.1 Fracture

Fracture denotes the breaking apart of a material due to an external force or stress. The rate of occurrence and the nature of this separation can vary based on

the type of applied stress and the inherent properties of the material. Traditionally, fracture is divided into two primary types:

1. Brittle Fracture: It can be described as a property exhibited by materials that fracture with limited or negligible preceding plastic deformation. Such fractures are abrupt; glass can be mentioned as a typical brittle material. Considering symmetrical loading condition, Mode I, the fractured surface in this case is often flat and aligns perpendicularly to the applied stress direction.

2. Ductile Fracture: In contrast to its brittle counterpart, a ductile fracture is characterized by significant plastic deformation occurring prior to the fracture event. Metals, for instance, often undergo this type of fracture. A notable characteristic of ductile fractures is the necking phenomenon, where the material's cross-sectional area reduces before the final fracture.

1.2.2 Fatigue

Fatigue arises when materials undergo repetitive and fluctuating stresses over an extended duration, typically at amplitudes significantly lower than the material's yield strength. Unlike a single, isolated event such as fracture, fatigue results from the cumulative impact of numerous loading and unloading cycles. Broadly, the fatigue phenomenon can be divided into three main phases:

1. Initiation: During this initial stage, tiny cracks begin to form, often at locations where stress concentrations occur, such as surface irregularities, inclusions, or notches. In these small areas, the appearance of cracks sets the stage for the development of persistent slip bands. These bands propagate along the plane of maximum shear, oriented at a 45-degree angle from the direction of the applied load, under the influence of cyclic loading.

2. Propagation: Following initiation, these small cracks progressively grow with each subsequent loading cycle. The rate of growth depends on the amplitude of cyclic stress and the mechanical properties of the material.

3. Final Failure: After enduring a specific number of cycles, the crack reaches a critical size, leading to the sudden failure of the structure.

1.2.3 Wöhler Curve and Basquin Equation

The study of material fatigue and fracture mechanics has evolved significantly over the past century. One of the foundational concepts in fatigue analysis is the Wöhler curve [1], named after the German engineer August Wöhler. Running parallel in importance to the Wöhler curve is the Basquin equation [2], which provides a mathematical representation of the Wöhler curve. Understanding these

concepts and their relationship is crucial for predicting the fatigue life of materials under cyclic loading.

Wöhler curve: The Wöhler curve, also known as the SN (Stress-Number of cycles) curve, is a graphical representation that describes the relationship between the amplitude of a cyclic stress and the number of cycles to failure of a material. Typically, the curve is plotted with stress amplitudes on the y-axis and the logarithm of the number of cycles to failure on the x-axis. It is worth noting that Wöhler did not present the results of his studies as a curve, and this was done in 1936 by Kloth and Stroppel [3]. The curve typically exhibits three distinct regions:

1. Low-cycle fatigue (LCF): Here, the material fails after a relatively small number of cycles. In this case, the stress amplitude is high, and the failure is characterized by repeated plastic deformation.

2. Transition region: This is a region where the material's behavior shifts from LCF to High-cycle fatigue. The transition point is usually in between 10^3 and 10^4 cycles.

3. High-cycle fatigue (HCF): In this region, the material can withstand a large number of cycles (at lower stress amplitudes) and is characterized by elastic deformation.

It is important to note that the Wöhler curve is specific to a particular material and loading condition. Environmental factors, like temperature and humidity, as well as microstructural properties of the material, can influence the shape and characteristics of the curve.

Basquin Equation: The high-cycle fatigue region of the Wöhler curve is often approximated as a straight line on a log-log plot, and this linear relationship can be described by the Basquin equation [2]. The equation is given by a power law like $\sigma = a\ N^b$, where: σ is the stress amplitude, a is the fatigue strength coefficient, representing the stress amplitude at which failure occurs after a single reversal of stress, N is the number of cycles to failure, and b is the fatigue strength exponent, typically a negative value, which indicates the slope of the line in the log-log plot.

By fitting experimental SN data to this equation, one can derive the fatigue strength coefficient and the fatigue strength exponent for a specific material. These parameters are crucial for predicting the fatigue life of materials under various loading conditions.

1.2.4 Paris Curve

The Paris-Erdogan Law [4], commonly referred to as the Paris curve, offers a fundamental approach to understanding the sub-critical crack growth behavior

under cyclic loading. This relationship, established through rigorous yet empirical studies, links the rate of crack growth to the cyclic range of stress intensity factor, providing a foundational framework for fatigue crack propagation analysis. Mathematically, the Paris Law is represented as $\mathrm{d}a/\mathrm{d}N = c\,\Delta K^m$, where $\mathrm{d}a/\mathrm{d}N$ is the incremental crack growth per loading cycle, ΔK symbolizes the range of the stress intensity factor, c and m are empirically derived material constants, with c often representing a scaling factor and m characterizing the sensitivity of crack growth to the stress intensity factor range. The Paris region is typically characterized by a near-linear trend on a log-log plot of $\mathrm{d}a/\mathrm{d}N$ against ΔK. Outside this region, the crack growth rate can either accelerate rapidly (leading to catastrophic failure) or decelerate to a threshold below which no significant crack growth is observed. It is also essential to recognize the limitations and applicability of the Paris Law. The Paris curve's significance lies in its ability to predict the fatigue life of engineering components. By determining the material constants c and m through experimental tests and fitting the data to the Paris Law, engineers and researchers can estimate the crack propagation rate under different stress conditions, enabling more accurate life predictions and safer design practices.

1.2.5 Debonding

Debonding is a phenomenon especially related to composite structures which refers to the separation or loss of bond between distinct layers or components of the composite. Such separation can be the result of various factors, including mechanical stresses, thermal fluctuations, or environmental degradation. In adhesive joints and laminated composites, debonding can critically affect structural integrity. Consequently, a robust understanding and predictive capability concerning debonding is essential for optimizing design, enhancing durability, and foreseeing maintenance requirements of composite structures. The multifaceted nature of debonding, influenced by material properties, geometrical considerations, and external conditions, typically necessitates a multidisciplinary approach.

1.3 Fundamental failure criteria

For the sake of simplicity, the analysis in this section focuses solely on Mode I crack propagation. In analyzing brittle or quasi-brittle materials, two failure criteria are commonly employed. The first one is based on stress state, is typically referred to as Rankine's criterion [5] and it is represented by the equation:

$$\sigma = \sigma_c \tag{1-1}$$

In simple terms, failure occurs if the maximum principal (positive) normal stress σ attains the material's tensile strength σ_c, at least in one point. The second

criterion, commonly known as Griffith criterion, is based on energy and is expressed by the equation:

$$\mathcal{G} = \mathcal{G}_c \tag{1-2}$$

This criterion states that failure occurs when the crack-driving force $\mathcal{G}$ meets the crack resistance $\mathcal{G}_c$. Here, $\mathcal{G}_c$ is known as the fracture energy, which is the energy required to form a unit fracture surface. According to Irwin's formula, this energy-based criterion can also be described using the stress intensity factor K_I and the fracture toughness K_{Ic}, as represented by:

$$K = K_{Ic} \tag{1-3}$$

Rankine's criterion is effective for analyzing bodies without cracks, while the energy-based (Griffith) criterion is suitable for bodies that have a sufficiently large crack. However, both criteria have limitations. Specifically, the stress criterion predicts a null failure load for a body containing a crack, as the stress field becomes singular at the crack tip. Conversely, the energy-based criterion predicts an infinite failure load for a crack-free body, since the stress-intensity factor is zero when there is no crack. Clearly, the aforementioned criteria are effective for extreme cases, such as bodies with no cracks or those with large cracks. However, they are not applicable for intermediate scenarios, such as bodies with short cracks or sharp notches.

To address these limitations, various failure criteria have been introduced in the literature. For numerical applications involving quasi-brittle materials, one notable model is the Fictitious Crack Model (FCM), introduced by Hillerborg et al. [6]. This model considers both the tensile strength and fracture energy of the material in question. The FCM, along with the strictly related Cohesive Zone Model, necessitates the implementation of a specialized numerical algorithm within structural design codes. So, it offers a highly versatile tool for the analysis of structures made from quasi-brittle materials.

Simpler criteria can also be proposed by introducing a material characteristic length l_f. This facilitates obtaining analytical results, especially for straightforward geometries, or allows for the coupling of the failure criterion with a linear elastic analysis conducted via computer simulations, such as the Finite Element Method. The role of the characteristic length l_f is to incorporate the fracture toughness into the stress-based criterion or the tensile strength into the energy-based criterion. These models are explored in more detail in the following section. For clarity,

consider the scheme presented in Fig. 1-1. In this scheme, the crack is subjected to Mode I loading, and it extends along the x-axis and has a length of 2*a*.

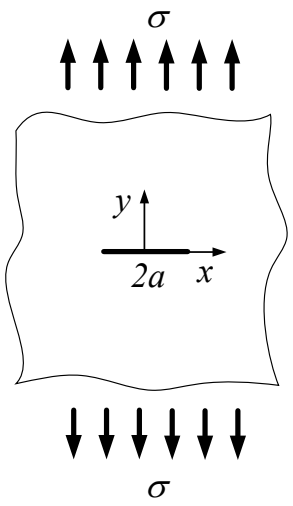

Fig. 1-1. A schematic view of a central crack in an infinite plate under remote stress of σ.

1.4 Theory of Critical Distances and Quantized Fracture Mechanics

In the stress-based failure criterion, failure is expected to occur when the average stress within a segment of length l_{LM} ahead of the crack tip reaches the critical value σ_c. In other words, failure is achieved when the force resultant over a segment of length l_{LM} located in front of the crack tip attains the critical value $\sigma_c \times l_{LM}$. It is worth noting that the stress criterion has historical roots in the work of Neuber [7] and Novozhilov [8]. The criterion can be expressed mathematically as follows:

$$\int_a^{a+l_{LM}} \sigma_y(x)\,\mathrm{d}x = \sigma_c\, l_{LM} \tag{1-4}$$

Clearly, this criterion reverts to Eq. (1-1) for a specimen without a crack under tensile loading. Conversely, the value of the material length l_{LM} must be determined by imposing Eq. (1-3) for a relatively large crack, i.e., $a \gg l_{LM}$. In this scenario, the asymptotic stress field $\sigma_y = K_I / \sqrt{2\pi(x-a)}$ can be employed. Substituting this into Eq. (1-4) yields:

$$l_{LM} = \frac{2}{\pi}\left(\frac{K_{Ic}}{\sigma_c}\right)^2 \tag{1-5}$$

To yield accurate results for intermediate cases, the stress field used in Eq. (1-4) should be the exact solution, rather than the asymptotic one applicable as $x \to a$. For example, in the case of a central through-crack in an infinite body, Westergaard's solution should be employed. When an exact analytical solution is not available, the stress field can be determined numerically using finite element analysis. It should be noted that Eq. (1-5) was proposed by Taylor, refining this criterion further. The method is termed the Theory of Critical Distances, a name stemming from the fact that failure is assessed over a material-dependent distance.

The energy criterion, as defined by Eq. (1-6), was pioneered by Pugno and Ruoff [9] under the name of Quantized Fracture Mechanics. According to this criterion, failure occurs when the energy available over the crack extension length (l_E) attains the critical value $\mathcal{G}_c \times l_E$. This can be mathematically formulated as follows:

$$\int_a^{a+l_E} \mathcal{G}(a)\,\mathrm{d}a = \mathcal{G}_c\, l_E \qquad \text{or} \qquad \int_a^{a+l_E} K_I^2(a)\,\mathrm{d}a = K_{Ic}^2\, l_E \tag{1-6}$$

Clearly, this criterion reverts to Eq. (1-3) for a specimen with a large crack. Conversely, the value of the material length l_E must be determined by imposing Eq. (1-1) for a specimen with a vanishing crack, $a = 0$. In this context, considering only through-cracks in two-dimensional geometries, the asymptotic value for the stress-intensity factor K_I is given by $K_I = c\sigma\sqrt{\pi a}$, where c is a dimensionless factor called shape factor. It is equal to 1 for center cracks and 1.122 for edge cracks. Substituting this expression into Eq. (1-6) results into:

$$l_E = \frac{2}{\pi}\left(\frac{K_{Ic}}{c\,\sigma_c}\right)^2 \tag{1-7}$$

To obtain meaningful results, the function describing the stress intensity factor in Eq. (1-6) should be exact, rather than asymptotic, as a approaches zero. However, it is important to note that when the stress-intensity factor vs. crack length (a) functions are readily available in SIF handbooks, Eq. (1-6), the energy criterion, is much simpler to apply compared to Eq. (1-4), the stress criterion. This is because an analytical solution for the stress field needed in Eq. (1-4) is often not available, therefore, requiring finite element analysis for each specific crack length a.

A second observation regarding the failure criteria discussed above is that the characteristic lengths (Eqs. (1-5) and (1-7)) serve as indicators of the material's brittleness. For example, from Eq. (1-4), it becomes evident that a very small characteristic length, implies that the failure load is primarily influenced by the asymptotic stress field, leading to a brittle structural behavior governed by material toughness (Eq. (1-3)). Conversely, a very large characteristic length suggests that the failure load is influenced by the entire stress field, resulting in a ductile structural behavior governed by material strength (Eq. (1-1)). In essence, the brittleness of the structural behavior is determined by the ratio of the material length to a characteristic length of the structure itself. This ratio aligns with the brittleness number introduced by Carpinteri [10].

The physical interpretation of the two criteria (Eqs. (1-4) to (1-6)) is straightforward: fracture does not propagate in a continuous manner but rather through finite extensions of the crack, the length of which is a material constant. From a physical standpoint, it is worth noting that many, if not all, fracture processes involve discontinuous crack growth instead of smooth, continuous extension. This is observed at least in the initial stages of the fracture process, as documented for various materials such as metals [11], polymers [12], and bones [13]. These discontinuous crack advancements are likely influenced by the material's microstructure, such as barrier spacing or grain boundaries, contributing to phenomena like snap-back. However, a complete understanding of these microstructural processes remains elusive.

It is noteworthy that the crack extensions, as defined by Eqs. (1-5) and (1-7) for the stress and energy criteria, are identical for a center crack but exhibit slight differences for an edge crack. Simulations conducted in [14] revealed that while the predictions made by these two criteria are generally similar, they are not identical.

1.4.1 TCD for finite fatigue life estimation

To employ the TCD approach within the static loading, input data include σ_c and K_{Ic}. To expand its application to finite fatigue life failure, one needs access to the critical stress and SIF amplitude as functions of the number of cycles until failure, as outlined in [15]. Wöhler curve for an unnotched specimen can serve as a representation of how the critical stress varies with the number of cycles until failure:

$$\sigma_f = \sigma_f(N) = a_s \, N^{-b_s} \tag{1-8}$$

Taking inspiration from Basquin equation [2], it is possible to assume a power-law relationship with respect to N for the critical SIF, K_{If} [16,17]:

$$K_{If} = K_{If}(N) = a_k \, N^{-b_k} \tag{1-9}$$

It is worth noting that Eq. (1-9) is equivalent to using a critical distance $l_{f,\,LM}$ that varies with the number of cycles to failure, as described by a power-law equation. Eq. (1-10) illustrates that the parameters a_l and b_l are straightforwardly related to a_s, b_s, a_k, b_k:

$$l_{f,LM} = l_{f,LM}(N) = \frac{2}{\pi}\left(\frac{K_{If}}{\sigma_f}\right)^2 = a_l \, N^{-b_l} \tag{1-10}$$

Indeed, in the original paper [15], the Authors directly employed Eq. (1-10) rather than Eq. (1-9), deriving the function $l_{f,LM}(N)$ through an inverse calibration method utilizing stress-life data associated with the sharpest notched sample. Subsequently, by substituting σ_c and $l_{f,LM}$ in Eq. (1-4) with σ_f and $l_{f,LM}$ one gets:

$$\int_a^{a+l_{f,LM}} \sigma_y(x)\,\mathrm{d}x = \sigma_f \, l_{f,LM} \tag{1-11}$$

With a known nominal stress amplitude for the sample, σ_y, there exists a single unknown variable N, whose solution determines the number of cycles to failure, N_f.

In order to obtain the two free parameters in $l_{f,\,LM}$ (Eq. (1-10)), namely a_l and b_l (or equivalently, a_k and b_k for K_{If}), necessitates a minimum of two data points. In [15], two distinct methods were suggested for this calibration process. The first method involved the use of two extreme scenarios in the finite fatigue life regime, specifically the static and fatigue limits. The second method utilized stress-life (SN) data obtained from a notched sample across a wide range of finite fatigue lives to calibrate the parameters. In this thesis, both approaches are employed.

1.5 Finite Fracture Mechanics criterion

The coupled stress and energy criterion, Finite Fracture Mechanics (FFM), seeks to bridge the shortcomings inherent in the stress-based and energy-based criteria when they are independently taken into account. In both approaches, the introduction of the internal length l accommodates limit cases –namely, the long crack failure load for the stress criterion and the no crack failure load for the energetic criterion. However, the fulfillment of one criterion typically implies the violation of the other. Specifically, when the stress-based criterion is met, the energy released during the crack extension may not necessarily equal $\mathcal{G}_c \times l_E$,

violating the energy balance. Conversely, when the energy-based criterion is satisfied, the resultant of the stresses acting on the crack extension might not align with the product $\sigma_c \times l_{LM}$.

Thus, the need arises for a coupled approach that harmonizes these two facets to yield a more comprehensive failure criterion. The idea is to establish a framework in which both the stress and energy conditions are satisfied, with the characteristic length, l_c, being not only a material constant but a structural variable:

$$\begin{cases} \int_a^{a+l_c} \sigma_y(x)\,\mathrm{d}x \geq \sigma_c\, l_c \\ \int_a^{a+l_c} K_I^2(a)\,\mathrm{d}a \geq K_{Ic}^2\, l_c \end{cases} \tag{1-12}$$

Eq. (1-12) states that failure occurs when two conditions are met. First, the stress in a segment of length l_c is larger than $\sigma_c \times l_c$. Second, the energy available for the crack to grow in that segment is greater than $\mathcal{G}_c \times l_c$. Eq. (1-12) consists of two inequalities with two unknowns, and meeting both conditions is both necessary and sufficient for the crack to grow. It can be straightforwardly verify that the lowest load at which both inequalities are met is when they are rigorously satisfied [18]. In other words, in the context of what are referred to as *positive geometries*, that is the predominant scenario, the set of inequalities presented in Eq. (1-12) transforms into a pair of equations with two variables: the failure load (for instance, the critical remote stress, which is implicitly embedded in the stress field and the SIF) and the critical crack advance.

Note that a similar criterion was proposed by Leguillon [19,20] to predict the failure load in a three-point bending beam with re-entrant corners of varying opening angles. In Leguillon's approach, the stress condition is based on a pointwise criterion. However, in this thesis, the focus is only on Eq. (1-12).

1.5.1 FFM for fatigue limit estimation

More recently, an adaptation of FFM has been introduced to estimate the fatigue limit of notched elements. This adaptation was achieved by substituting the mechanical properties, typically observed in static loading, with their respective counterparts at the fatigue limit [21,22]:

$$\begin{cases} \frac{1}{l_R}\int_0^{l_R} \Delta\sigma_y(x)\,\mathrm{d}x \geq \Delta\sigma_0 \\ \frac{1}{l_R}\int_0^{l_R} \Delta K_I^2(a)\,\mathrm{d}a \geq \Delta K_{th}^2 \end{cases} \tag{1-13}$$

In this equation, $\Delta\sigma_0$ shows the fatigue limit or the high-cycle fatigue strength related to the unnotched specimen, while ΔK_{th} stands for the threshold value of the SIF range related to the cracked sample. It should be noted that both material attributes ($\Delta\sigma_0$ and ΔK_{th}) should correspond to the same load ratio, R. Similar to FFM for static loading, Eq. (1-13) once more demonstrates a system with two unknowns: the critical crack advance l_{Rf}, and the fatigue strength $\Delta\sigma_{Rf}$, implicitly embedded in $\Delta\sigma_y$ and ΔK_I.

1.6 Phase Field approach

The Phase Field model provides a continuum-based framework for approximating fracture phenomena, thereby eliminating the need for explicit tracking of the crack interface. In this methodology, material heterogeneities, such as cracks, are characterized by a smooth function that delineates the evolution of damage, d, between two reference states: intact material and a fully developed crack, see Fig. 1-2.

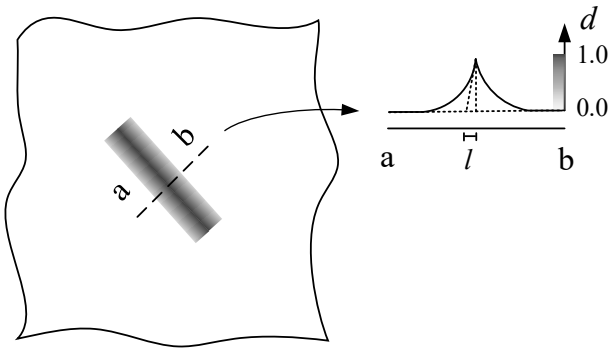

Fig. 1-2. Regularized crack approximation based on Phase Field approach.

The theoretical foundation of the Phase Field model for fracture is rooted in the principles of variational mechanics, as established by Francfort and Marigo [23] in 1998 and subsequently refined by Bourdin et al. [24] in 2000. The model comprehensively captures the entire sequence of crack initiation, propagation, and branching by minimizing the system's energy functional. This minimization yields a set of coupled partial differential equations (PDEs) that govern both the mechanical deformation and the evolution of the Phase Field (damage).

To start, assume the following conditions for the problem: isothermal conditions, negligible inertial effects, smooth time-dependent loading, and brittle fracture conditions. These assumptions allow for the application of specific energetic principles associated with rate-independent systems [25], including an

energy balance, a dissipation inequality, and a stability criterion, applied to a well-defined set of energetic variables. Additionally, the study assumes that small strains are present and that all dissipative processes are irreversible. Following the assumptions, for a linear elastic body, the internal energy density, W, can be written as:

$$W(\boldsymbol{\varepsilon}(\boldsymbol{u}), d) = \psi_{el}(\boldsymbol{\varepsilon}(\boldsymbol{u}), g(d)) + \varphi(d) \tag{1-14}$$

where ψ_{el} and φ are the elastic energy density and fracture energy density of the solid. $\boldsymbol{\varepsilon}$ represents the infinitesimal strain tensor, which can be calculated as the gradient of the displacement field, $\boldsymbol{u}$. The variable d serves as a scalar indicator for the Phase Field (damage) parameter, with its value fluctuating between 0 and 1, to represent intact and fractured material. The function g is a non-increasing function which controls the shift in the material's mechanical properties from an intact to a fractured state. Its value should be one for the intact state, and zero for the broken state. While various functions have been proposed in the literature [26,27], in this thesis, the most well-established relationship is used:

$$g(d) = (1-d)^2 \tag{1-15}$$

Focusing on fracture energy density, it can be written as [24]:

$$\varphi(d) = \frac{\mathcal{G}_c}{4\, c_w}\left(\frac{w(d)}{l} + l\left|\nabla d\right|^2 \right) \tag{1-16}$$

where

$$c_w = \int_0^1 \sqrt{w(\delta)}\, \mathrm{d}\delta \tag{1-17}$$

The parameter l is the key parameter that characterizes the width of the diffuse interface between different phases or domains, see Fig. 1-2. In other words, it sets the length scale over which the transition between different phases occurs. $\mathcal{G}_c$ represents the fracture toughness, and the non-decreasing function w is called dissipation function that describes the rate at which energy is dissipated or lost in the system due to irreversible processes. In other words, the energy dissipation due to the formation of new cracks in the material is governed by the dissipation function. The function should be equal to zero for the intact state, and equal to unity for the broken state. Here, focus is on two widely-used models for the dissipation function, which are called AT1 and AT2 [28]. In AT1, $w(d)=d$ and $c_w=2/3$, while in AT2, $w(d)=d^2$ and $c_w=1/2$. Note that the AT1 model was introduced to reproduce a constitutive behavior that includes an initial linear elastic branch, while for AT2, $w'(0)$ is equal to zero, which implies a vanishing threshold for the onset of damage. As a result, the material model does not feature an initial linear elastic branch.

Considering D-dimensional body Ω, by integrating over its domain, energy functional can be written as:

$$E_l(\boldsymbol{u}, d) = \int_\Omega \psi_{el}(\boldsymbol{\varepsilon}(\boldsymbol{u}), g(d))\, \mathrm{d}\boldsymbol{x} + \frac{G_c}{4\, c_w} \int_\Omega \left(\frac{w(d)}{l} + l \left| \nabla d \right|^2 \right) \mathrm{d}\boldsymbol{x} \tag{1-18}$$

Γ-convergence ensures that the regularized energy functional, E_l, is a valid approximation to the unregularized functional, particularly as l approaches zero. It provides a rigorous way to understand how the solutions to a regularized problem approximate the solutions to the original. Specifically, Γ-convergence results guarantee that both the minimum values (minima) and the configurations that achieve these minimum values (minimizers) of E_l will converge to the corresponding minima and minimizers of the unregularized functional when l tends to zero.

Utilizing the energy functional in Eq. (1-18) and incorporating the irreversibility condition, $\dot{d} \geq 0$, results in the governing equations. These equations address both the balance of momentum and the evolution of the Phase Field, along with their corresponding boundary conditions. For more information, see [29,30].

1.6.1 Decomposition of the elastic strain energy density

To account for the asymmetry in materials behavior under tension and compression, a decomposition of the elastic strain energy into active and inactive components is required. This is an important feature, especially in fatigue, where the material undergoes several tension and compression cycles. For this reason, the elastic strain energy density can be written as:

$$\psi_{el}(\boldsymbol{\varepsilon}(\boldsymbol{u}), g(d)) = g(d)\, \psi^{+}_{el,0}(\boldsymbol{\varepsilon}) + \psi^{-}_{el,0}(\boldsymbol{\varepsilon}) = \psi^{+}_{el}(\boldsymbol{\varepsilon}, d) + \psi^{-}_{el,0}(\boldsymbol{\varepsilon}) \tag{1-19}$$

In this context, $\psi^{+}_{el,0}(\boldsymbol{\varepsilon})$ and $\psi^{-}_{el,0}(\boldsymbol{\varepsilon})$ represent the active and inactive segments of the undamaged elastic strain energy density $\psi_{el,0}$. Consequently, the stored elastic strain energy density in a damaged material is divided into an active component $\psi^{+}_{el,0}(\boldsymbol{\varepsilon}, g(d)) = g(d)\, \psi^{+}_{el,0}(\boldsymbol{\varepsilon})$, which undergoes degradation, and an inactive component $\psi^{-}_{el,0}(\boldsymbol{\varepsilon})$ which remains unaffected by the Phase Field parameter. In the following, some of the common decompositions are mentioned.

Isotropic split [24]**.** It is the simplest model which allows for the degradation of the entire elastic strain energy density. As a result, it allows the material to undergo damage under both tension and compression.

$$\psi^{+}_{el,0}(\boldsymbol{\varepsilon}) = \frac{1}{2}\lambda\, tr^2(\boldsymbol{\varepsilon}) + \mu\, tr(\boldsymbol{\varepsilon}^2), \qquad \psi^{-}_{el,0}(\boldsymbol{\varepsilon}) = 0 \tag{1-20}$$

where λ and μ are Lamé parameters.

Volumetric/Deviatoric split [31]**.** In this model, the degradation function impacts only the energy density associated with the deviatoric component and the positive volumetric portion of the strain tensor. The mathematical expression of it can be given as:

$$\psi^{+}_{el,0}(\boldsymbol{\varepsilon}) = \frac{1}{2}\boldsymbol{B}\left\langle tr(\boldsymbol{\varepsilon})\right\rangle^2_{+} + \mu\, tr(\boldsymbol{\varepsilon}_{dev} : \boldsymbol{\varepsilon}_{dev})^2, \qquad \psi^{-}_{el,0}(\boldsymbol{\varepsilon}) = \frac{1}{2}\boldsymbol{B}\left\langle tr(\boldsymbol{\varepsilon})\right\rangle^2_{-} \tag{1-21}$$

where $\boldsymbol{B} = \lambda + 2\,\mu/3$ represents the bulk modulus of the body, and $\langle\ \rangle$ represents the Macaulay bracket.

Spectral Split [32]**.** This model distinguishes between the degraded and undegraded segments of the energy density by employing the spectral decomposition of the strain tensor, represented as $\boldsymbol{\varepsilon}^{\pm} = \sum_{a=1}^{3}\left\langle \varepsilon_a \right\rangle_{\pm} \boldsymbol{n}_a \otimes \boldsymbol{n}_a$, where ε_a and $\boldsymbol{n_a}$ are the eigenvalues and eigenvectors of the strain, respectively. Thus, the model can be cast as:

$$\psi^{\pm}_{el,0}(\boldsymbol{\varepsilon}) = \frac{1}{2}\lambda\left\langle tr(\boldsymbol{\varepsilon})\right\rangle^2_{\pm} + \mu\left[tr(\boldsymbol{\varepsilon}^{\pm})^2\right] \tag{1-22}$$

No-Tension Split [33]**.** This model is simple and effective to mimic the behavior of brittle and quasi-brittle materials, such as masonry. These materials are typically strong in compression but weak in tension. The no-tension split allows the model to capture this behavior by degrading the energy associated with tensile strains, while leaving the energy associated with compressive strains undegraded.

$$\psi^{\pm}_{el,0}(\boldsymbol{\varepsilon}) = \frac{1}{2}\lambda\, tr^2(\boldsymbol{\varepsilon}^{\pm}) + \mu\left[tr(\boldsymbol{\varepsilon}^{\pm})^2\right], \qquad \boldsymbol{\varepsilon}^{\pm} = sym_{\pm}(\boldsymbol{\varepsilon}) \tag{1-23}$$

1.6.2 Relations between parameters

In Phase Field modeling, a fundamental approach is to examine a one-dimensional (1-D) homogeneous solution since the problem can be solved analytically. This analysis, rooted in the work presented in [29], allows for the derivation of the relations between the peak stress σ_c, the fracture toughness $\mathcal{G}_c$, the Young modulus E and the regularization length l for both AT1 and AT2 models:

$$\sigma_c^{AT1} = \sqrt{\frac{3E\mathcal{G}_c}{8l}} \tag{1-24}$$

$$\sigma_c^{AT2} = \frac{9}{16}\sqrt{\frac{E\mathcal{G}_c}{3l}} \tag{1-25}$$

1.7 Cohesive Zone Modelling

One of the fundamental assumptions in the energy (Griffith) criterion is the concept of stress singularity, which assumes an instantaneous change in stress along the crack path as the crack grows. According to Griffith's original formulation, points along the crack path move abruptly from a state of full integrity to complete fracture. This assumption has been shown to be inconsistent with experimental observations, where stress fields near the crack tip exhibit a finite range [34].

This limitation restricts the Griffith criterion's predictive capability for crack initiation. In this model, if the stress at a point undergoes an instantaneous change, the energy dissipated during the process must reach a finite value instantaneously, drawing from the energy released during crack propagation. This is consistent with the concept of the energy release rate $\mathcal{G}$, which is a key quantity in fracture mechanics [35]. However, as mentioned before, this condition is only feasible when a crack of finite length exists. In contrast, due to the differential scaling between energy dissipation and release, the Griffith criterion is not applicable for a crack with negligible length. Therefore, if this assumption is relaxed – meaning that the stresses can evolve in a more gradual manner – the energy required to create a new crack surface with an infinitesimal area can be met continuously, following a predetermined trajectory. This concept is the basis for Cohesive Zone Models (CZMs), initially introduced by Dugdale in 1960 [36] and Barenblatt in 1962 [37]. These models establish laws that correlate the separation of crack faces with the stresses transmitted across them, usually named traction-separation laws.

Generally, CZMs define the normal tractions σ along the cohesive zone as functions of the relative displacements s between the two surfaces, $\sigma = \sigma(s)$. These tractions become zero when the relative displacements reach a critical value s_f. In case of symmetric cracking under Mode I loading conditions, a crucial characteristic of the CZM is that the area beneath the cohesive law curve is equivalent to the fracture energy. This relationship can be mathematically expressed as follows:

$$\mathcal{G}_c = \int_0^{s_f} \sigma(s)\,\mathrm{d}s \tag{1-26}$$

Based on this, there exists a direct relationship among the fracture energy, the cohesive law, and the final displacement. Possessing information on any two of these three parameters is sufficient to comprehensively define the problem. Similar equation as Eq. (1-26) can be written for Mode II of fracture; however mixed modes problems might be much more changing within this approach.

In a broader context, the CZM can be seen as a specific application of damage mechanics, with some key conceptual differences. In CZM, damage is limited to a set number of defined surfaces, known as cohesive zones. The dimensionless separation parameter s/s_f, often represented as δ, acts as a damage variable that controls the constitutive law for the material. In CZM, the area experiencing damage is called the process zone. This term is especially relevant for cracked bodies, as this is the area where irreversible processes mainly occur.

In supporting the assumption of a continuous separation law and the presence of cohesive tractions, analysis of the microstructural features is useful. For example, in concrete, interactions among its components mainly lead to the formation of isolated microcracks and other phenomena. This reduces the material's ability to endure tractions. Detailed studies, such as those by Otsuka and Date [38], offer a complete understanding of the process zone in concrete. In composite materials, the existence of a process zone is also linked to the different behaviors of its components. Long fibers in the composite can act as traction bridges, helping to maintain a significant part of the material’s ability to bear loads. Interestingly, Huo et al. [39] proposed an approach to extract the traction-separation law based on digital image correlation (DIC). It is important to note that the form of the cohesive law is closely related to the material’s microstructure and how it fails. So, in addition to basic failure properties like strength and fracture energy, the specific form of the cohesive law also depends on the material. Many different forms have been proposed to accurately describe the behavior of specific materials or to address particular problems. For the sake of simplicity, the focus is on pure Mode I loading conditions. Some of the most commonly used forms of the cohesive law are discussed in the following and their shapes are presented in Fig. 1-3:

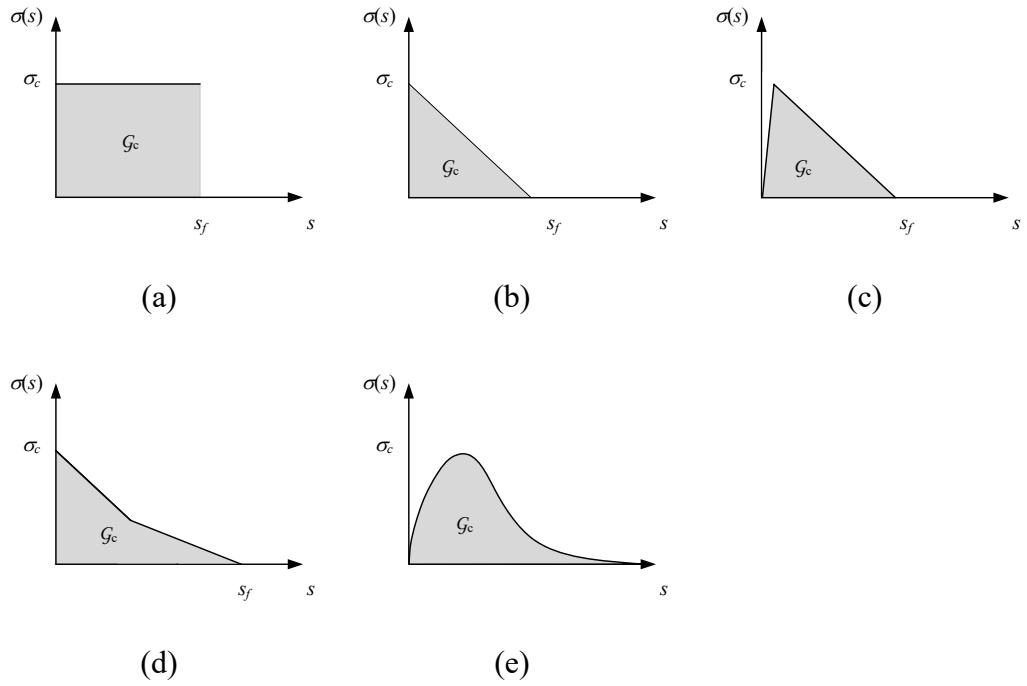

Fig. 1-3. Some of the common cohesive laws. (a) Dugdale (constant), (b) Linear softening, (c) Triangular, (d) Bilinear, (e) Exponential.

Constant cohesive law [36]**:** The Constant Cohesive Law represents a simplistic yet effective approach for understanding and describing fracture processes, especially near the crack tip, where the behavior of materials under stress becomes critical. Initially proposed by Dugdale, this model is pivotal in addressing the plastic deformation occurring near the crack tip by capping the tractions at a predefined yield strength. By doing so, the model effectively mitigates the unrealistic stress singularities observed at the crack tip. This is particularly beneficial as it provides a more realistic representation of the stress distribution around the crack tip, aiding in the prediction and analysis of crack propagation and failure under various loading conditions. Furthermore, thanks to its simplicity, the Dugdale model lends itself well to analytical or semi-analytical solutions.

Linear softening cohesive law [6]**:** It was introduced by Hillerborg, and is significantly useful when it comes to modeling fracture processes in concrete or similar materials, a behavior that has been substantiated through experimental findings. Basically, this model delineates the behavior of concrete as linear elastic as far as the tractions remain below the tensile strength. Once the tensile strength is reached, a linear softening phase ensues, extending up to a specified softening point, denoted as s_f. The simplicity and empirical relevance of the Linear Softening model provide a useful tool for understanding and analyzing the fracture behavior of several materials.

Triangular cohesive law [40]**:** It was proposed by Geubelle and Baylor, and offers a more nuanced representation of material behavior under stress, especially in comparison to the Linear Softening law. This model consists of an initial linear hardening phase characterized by a finite slope, before transitioning to a softening phase similar to that of the Linear Softening model. The inclusion of an initial hardening phase not only reflects a more accurate behavior of certain materials under loading but also introduces an additional parameter into the model – the slope of the hardening phase. This additional parameter necessitates a definition, which adds a layer of complexity to the modeling process. However, this slope is often included for the sake of computational convenience, allowing for a smoother transition from the initial loading to the softening phase, and is typically set at a high value to ensure its impact on the overall modeling results is minimized. This high value helps in maintaining a near-constant stress level until the material reaches its tensile strength, after which the softening behavior dominates.

Bilinear Softening cohesive law: The Bilinear Softening cohesive law extends the concept of linear softening by introducing two distinct slopes during the softening phase, aiming to account for the mechanisms that cause an increase in fracture toughness with crack growth [41]. In this law, an extra parameter is introduced to define the transition between the two slopes, effectively dividing the traditional concept of fracture energy into initial and total fracture energy. The initial fracture energy is associated with the energy required to initiate crack propagation, while the total fracture energy encompasses the energy needed to sustain crack growth up to the point of material failure. Note that the second slope is typically less steep, and could represent a slowed rate of traction reduction, possibly due to mechanisms like crack bridging or other toughening mechanisms that come into play in the last cracking stage.

Exponential cohesive law [42]**:** The Exponential law proposed by Needleman in 1990 is a noteworthy model within cohesive zone modeling, characterized by an exponential form of traction-separation relationship. This law builds upon the concept of universal binding energy correlation, a notion initially brought forward by Rose et al. [43] in 1981. The universal binding energy correlation is a theoretical framework that relates the cohesive energy (or binding energy) between atoms to their separation distance, providing insight into the interatomic forces and the resultant material behavior at a macroscopic scale. The Exponential law leverages this concept to derive an exponential function that accurately represents the traction-separation relationship in a material as it undergoes fracture.

1.8 Connection analysis of Phase Field, FFM, and CZM approaches

In recent years, several attempts have been made to combine different models, leveraging the strengths of each. Regarding Phase Field and CZM, the Phase Field

regularized Cohesive Zone Model (PF-CZM), initially developed by Wu [44] and further elaborated by Wu and Nguyen [45], stands out as a pioneering approach applicable to both brittle and cohesive fractures. Compared to traditional discrete CZMs, such as those proposed by Wells and Sluys [46] and Wu and Li [47], the PF-CZM offers several advantages: it eliminates the need to track crack surfaces, avoids the penalty stiffness associated with intrinsic CZMs, and prevents crack face penetration. For a comprehensive discussion, refer to [48].

Considering the Phase Field model and Finite Fracture Mechanics (FFM), Doitrand et al. [49,50] reformulated the Phase Field approach to require the material tensile strength as input instead of the internal length classically used in Phase Field models. This reformulation addresses the challenge of identifying distinct internal length scales for various testing configurations of the same material, obviating the need to choose or identify an internal length. The implementation of this reformulated Phase Field method, termed Length-Free Phase Field (LF-PF), closely resembles the classical approach. However, the key distinction lies in substituting the internal length with a formulated expression incorporating the material's characteristic length and a normalized tensile strength term. This normalized term depends on the Poisson's ratio and the local principal stress ratio experienced by the material.

To the author’s best knowledge, there is no existing approach that couples FFM and CZM. However, it is noteworthy that despite their different mechanisms—continuous versus discrete crack growth—the energy expended to create a new unit fracture surface, G_c, is the same for both models. This condition is not typically met by simple strength criteria or by the Theory of Critical Distances. Furthermore, both CCM and FFM consider tensile strength: CCM incorporates it through the shape of the cohesive law, while FFM includes it in the stress condition expression. To date, there has been excellent correspondence between CCM with a constant cohesive law and FFM using a point-wise stress requirement, as well as between CCM with a linearly descending cohesive law and FFM using an average stress condition [51].

1.9 Problem statement and research objectives

In recent years, composite laminates have emerged as paramount in advanced structural engineering, mainly due to their superior mechanical properties and multifunctionality. However, a comprehensive understanding of their failure mechanisms, especially under complex loading conditions, remains unsolved. One of the complex loading conditions which is also the most common failure mode in real structures is fatigue, and is still an open topic of study. Accurately estimating fatigue life is crucial in the design and maintenance of a wide range of mechanical

systems and structures. This assessment determines the number of loading cycles a material can withstand before failure. The preliminary objective of the thesis is to study fatigue and fracture in composite structures. The previous methods to analyze such problems are usually time-consuming, lack generality across various problems, or are not completely reliable. For this reason, the thesis focuses on proposing a novel fatigue failure criterion, grounded in Finite Fracture Mechanics, which has already demonstrated accuracy in the failure analysis of notched components under static loading conditions. Furthermore, in the last part of the thesis, we propose an approach to study fatigue failure based on the Phase Field model.

Focusing on composite structures, debonding can be one of the main failure modes that defines the final load bearing of the structure. Therefore, first, FFM is extended to study the debonding behavior in composite structures, specifically the direct shear test, which is the most important test for studying debonding behavior in the external strengthening of existing structures. For this problem, a comparison with the cohesive zone model will also be provided for a complete analysis. Then, the FFM will be extended to estimate finite fatigue life of notched components in isotropic materials. Considering that the geometric discontinuities, including cracks, notches, and holes, are prevalent in mechanical structures, and since these discontinuities act as stress concentrators, they significantly influence the load-bearing capacity and operational lifetime of the structural component. Therefore, providing an accurate yet simple criterion has high value. Next, the proposed model for isotropic materials will be extended to obtain the fatigue lifetime of notched laminated composites. To validate the model, an extensive experimental program on notched carbon fibre laminated composites is conducted. Finally, the Phase Field model, which was recently extended to fatigue, is examined and validated by experimental data to obtain the Paris curve for isotropic materials.

The significance of this research goes beyond academic boundaries, extending to the practical problems of mechanical engineering and materials science. By offering a more reliable method for studying fatigue and fracture in composite structures, the thesis aims to reinforce safety standards in structural designs, thereby potentially preventing catastrophic failures, where the economic implications are also substantial. A precise understanding of fatigue can lead to an optimized maintenance schedule, providing significant savings by identifying when intervention is truly necessary. In an era increasingly conscious of environmental sustainability, the research promises an additional benefit: by developing structures with extended lifetimes, we can reduce material consumption and waste, promoting eco-friendly construction. This study also stands to invigorate future research,

serving as a foundational base upon which subsequent inquiries can develop. Industries such as aerospace and automotive can have valuable insights from our findings, refining their design strategies and material choices. Additionally, the thesis has an educational benefit. The methodologies and insights derived from this research can enrich academic curriculums, equipping the next wave of engineers and scientists with cutting-edge knowledge.

1.10 Structure of the Thesis

This thesis is organized to provide an exhaustive exploration of fatigue and fracture in composite structures, emphasizing the contributions of both the Finite Fracture Mechanics and the Phase Field approaches.

Chapter 1: Introduction.

The chapter presents some fundamental expressions within the domain of fatigue and fracture mechanics. It emphasizes the essential role of fracture mechanics in the engineering landscape, the challenges faced in current research, and then introduces the FFM and Phase Field methodologies, elucidating their respective merits, limitations, and potential intersections. The chapter provides a precise definition of the research objectives and an elaboration on the significance of the undertaken study.

Chapter 2: Literature Review.

This chapter provides a detailed chronological overview of the developments of FFM and Phase Field approaches. It systematically traces the evolution of key ideas and milestones, offering a comprehensive historical perspective that enriches the reader's understanding.

Chapter 3: Analytical Modeling of Debonding Mechanism in Direct Shear Tests Accounting for Residual Strength.

This chapter delves into the complexities of the debonding mechanism, specifically within the context of direct shear tests. This chapter acknowledges the importance of considering residual strength and utilizes analytical modeling to rigorously investigate this issue. Following an introductory section that contextualizes the importance of understanding debonding mechanisms, the chapter outlines the methodologies for modelling debonding by FFM and CZM, presents the results, engages in comprehensive discussions, and concludes with key takeaways from the study.

Chapter 4: Extension of Finite Fracture Mechanics Approach to Assess the Lifetime of Notched Components.

The focus of this chapter is to extend the FFM approach to assess the lifetime of notched components. Understanding the behavior of notches is crucial due to their presence in mechanical structures. After presenting the main idea behind, the model is developed and validated using five different sets of experimental data from the literature, encompassing a wide range of materials, notched geometries, loading conditions, and ratios for a wide range of fatigue lives.

Chapter 5: Extension of Finite Fracture Mechanics and Theory of Critical Distances to Fatigue Life Prediction of Notched Orthotropic Composite Laminates.

Starting from the previous chapter concepts and results, Chapter 5 extends FFM and integrates the Theory of Critical Distances to predict the fatigue life of notched orthotropic laminated composites. To validate the model, extensive ad hoc experimental tests were conducted, and the results are also presented in this chapter.

Chapter 6: Implementation of Phase Field to Model Fatigue of Brittle Materials.

The penultimate chapter of the main body focuses on the implementation of the Phase Field approach, particularly concerning the fatigue behavior of brittle materials. Recognizing the challenges associated with modeling such behavior, the chapter employs the Phase Field to offer new insights. Then, the model is validated by experimental data from literature.

Chapter 7: Conclusion and Future Work.

This chapter presents the main insights from the preceding chapters, drawing coherent conclusions. It further outlines prospective directions for subsequent research in the field of fatigue and fracture of composite structures.

Chapter 2

Literature Review

Fatigue and fracture mechanics have occupied an important position in mechanical engineering and materials science for decades. Over the years, as the understanding of fractures and fatigue in materials and structures has expanded, a significant body of research has accumulated. This chapter offers a review of studies related to Finite Fracture Mechanics (FFM) and the Phase Field model, presenting a structured overview of theoretical developments and the latest updates. It aims to establish a solid foundation for discussions in subsequent chapters. By examining both the historical and current state of FFM and Phase Field approaches, this literature review highlights ongoing challenges and potential opportunities for future research.

2.1 Finite Fracture Mechanics

In this section, a historical review on the formation of FFM is first presented, and its application for notched components is mentioned. Then, the studies by FFM for analyzing the debonding behavior and failure in laminated composites are presented.

Over many years, various approaches have been proposed to estimate the lifetime of materials weakened by different types of notches, affecting their resistance to failure. One of the most successful methods, introduced by Neuber [7] in Germany, is now commonly referred to as the Theory of Critical Distances (TCD). Neuber's method starts with the idea that the elastic stress caused by stress concentration is not as high as what is suggested by continuum mechanics theory. Based on this idea, Neuber suggested that to find the actual stress impacting the failure process, one should average the stress near the peak of the stress concentration over elements like crystals or structural particles. A few years later, Peterson [52] offered a simpler application of this concept. He argued that the reference stress, which should be compared to the material's strength, can be easily calculated at a specific distance from the tip of the stress concentrator. Several years later, the concept was reformulated to include both classical and Linear Elastic Fracture Mechanics. To this end, Taylor [53] introduced a formula for determining the critical distance, broadening the scope of the approach for assessing the fatigue strength of notched components. The updated methodology is termed the Theory of Critical Distances (TCD). Within this framework, the approach by Neuber [7] is

called the line (averaged) method, and the approach by Peterson [52] is called the point method. Based on the work by Taylor, for static loading conditions, the critical distance for brittle materials is a function of a characteristic length and can be obtained as a function of fracture toughness, K_{Ic}, and the ultimate strength of a plain specimen, σ_c, as $l_{ch} = (1/\pi)\,(K_{Ic}/\sigma_c)^2$. Clearly the characteristic length is only a function of material properties. The critical distance for the point method is $l_{PM} = 1/2\ l_{ch}$, and for line method is $l_{LM} = 2\ l_{ch}$.

Due to its simplicity and robustness, the TCD has been developed for a variety of problems. In the context of static loading, the strength of notched samples under mixed-mode loading conditions was accurately estimated by the TCD in [54]. The approach proved effective not only in predicting the failure load but also in determining the direction of crack propagation. Using analytical stress fields, Smith et al. [55] demonstrated the influence of T-stress on failure predictions by TCD for PMMA. The study highlighted that the impact of T-stress increases with greater dominance of Mode II loading. More recently, an extensive experimental program on blunt V-notches was conducted by Ayatollahi and Torabi [56] to verify the TCD approach for estimating the failure load of brittle materials. In a different application, TCD was adapted to predict static failures in notched low-carbon steel specimens undergoing large-scale plastic deformations [57]. The study confirmed the high accuracy of TCD-based predictions – within a 15% error margin – using post-processed results from linear-elastic Finite Element Analysis. A marginally higher level of precision was achieved when incorporating elasto-plastic analysis. As the use of additively manufactured materials is becoming more and more common, the TCD approach has been extended to assess the failure of notched samples made of acrylonitrile butadiene styrene (ABS) [58]. The study showed that the effects of different manufacturing angles can be neglected by averaging material properties. Despite this simplification, the model was found to offer acceptable accuracy in failure predictions.

Besides, TCD has been developed to predict the finite fatigue life of structures. This development is grounded in the pivotal concept that the critical distance diminishes as the number of cycles increases, adhering to a power-law behavior [15]. The two parameters that describe this dependency are functions of both the material and the loading ratio. Owing to the dependence of both the critical distance and fatigue strength on the number of cycles, an iterative method was proposed to determine the number of cycles until failure. Subsequently, the model was expanded to encompass multiaxial loading conditions by integrating the TCD with the critical plane approach [59]. To validate the model, several experimental fatigue tests were conducted under combined tension and torsion in both in-phase and out-of-phase scenarios. It is worth mentioning that due to the robustness of the model, the TCD has been recently applied to various fatigue conditions, ranging from torsional [60] to variable amplitude loading [61–63].

As previously discussed, within the static framework, the TCD relies on a critical length, hypothetically intrinsic to the material. This becomes problematic in specific configurations, such as small size devices, where this material length scale approaches or even surpasses the dimensions of the structure. To address this limitation, Leguillon [20] proposed a coupled fracture criterion commonly known as FFM. Analogous to TCD, FFM posits that crack extension takes place by finite increments. However, unlike TCD, FFM calculates the failure load and the critical distance by simultaneous fulfillment of two different criteria: a stress condition and an energy condition. As a result, the finite crack extension evolves into a structural parameter, thereby incorporating geometric considerations. This stands in contrast to the TCD methodology, where the critical distance remains solely a material parameter. Cornetti et al. [18] developed independently a similar criterion, but in this criterion the stress condition is in average form, while in Leguillon's proposed method [20], the stress at a point (similar to point method in TCD) should not exceed the material strength. The superior accuracy of FFM over TCD for sharp V-notches under Mode I was shown by Carpinteri et al. [64]. Subsequently, the FFM model successfully employed for static failure prediction of blunt notches under Mode I [65,66] and mixed mode loading conditions [67]. Notably, Sapora et al. [68] employed several experimental data sets on sharp V-notched samples under mixed-mode loading, to illustrate the accuracy of the FFM model. It is worthwhile to mention that Doitrand and Leguillon [69] extended the FFM criterion to estimate crack initiation by means of 3D finite element modeling. For a review on FFM and its applications, please refer to [70,71].

Moving from static to cyclic loading, the model was successfully extended to fatigue limit regime by Sapora et al. [21,22,72]. They checked the validity and accuracy of FFM for different notched geometries (from sharp cracks to blunt V-notches) under Mode I loading conditions. Studies by Shen et al. [73] and Liu et al. [74] have drawn comparisons between TCD and FFM predictions concerning the fatigue limit of V-notched components. These investigations revealed that while both criteria yield comparable results, FFM demonstrates superior precision for blunter notches, given that the critical distance is influenced by the radius of curvature. It is beneficial to highlight that several research papers in the literature [75,76] have validated that the critical distance is intrinsically linked to geometrical properties, contrary to the foundational assumptions of TCD. It is worth noting that based on an analogy between the Dugdale model [36] and the FFM criterion, Murer and Leguillon [77,78] tried to extend the FFM to fatigue loading conditions, but the model was not validated by the experimental results. This extension was achieved by considering a gradual degradation process along the presumed crack path. Notably, the model identifies a parameter that aligns the rate of crack advance with the Paris Law for pre-existing long cracks.

The literature on the applications of FFM to interface failures and debonding in composite structures is rich and evolving. Cornetti et al. [79] for the first time

extended FFM for determining the debonding load in composite structures using an elastic interface model. Another study extended this by applying FFM to a composite structure called double pull-push shear test, which is an important configuration in the context of reinforcement tests in civil engineering [80]. The paper employs Timoshenko beam theory and a Linear Elastic Brittle Interface Model (LEBIM), to predict the critical load for debonding. Interestingly, a comparative study between CCM and FFM for predicting debonding in double cantilever beam (DCB) test showed that both methods closely match in their predictions [81]. This paper also compares these approaches with simple and enhanced beam theories, highlighting the superiority of predictions by CCM and FFM for less brittle interfaces. In [82], a new numerical procedure based on LEBIM and FFM was developed by demonstrating its applicability in 2D Boundary Element Method codes. Furthermore, a hybrid method based on Leguillon's approach has been proposed to assess interface debonding, focusing on the integrity of adhesive bonds under severe thermal loading conditions [83]. Following the extension of FFM to 3D failure analyses [69], Doitrand and Leguillon [84] compared the results of 2D and 3D FFM formulation to predict crack initiation in scarf adhesive joints.

In the context of laminated composites, Camanho et al. [85] used FFM to study the size effect in open-hole laminated composites. Their work demonstrated the effectiveness of FFM in accurately predicting experimental results. Subsequently, FFM has been applied to assess the failure of laminated composites across diverse structural configurations, including but not limited to, mechanically fastened joints [86], irregular multi-bolt composite repairs [87], open-holed laminates subjected to mixed-mode loading [88], and those exhibiting R-curve behavior [89]. Further validation of FFM's robustness and reliability was provided by Reinoso et al. [90], who conducted a comparative analysis between FFM and Phase Field approaches on notched thin-ply laminates, affirming higher accuracy of FFM for the considered problem. It is worth emphasizing that all the investigations mentioned, which are based on the FFM model, have analyzed failure under static loading. In this thesis, the application of FFM is extended for the first time to the finite fatigue life regime.

2.2 Phase Field approach

The variational Phase Field approach to fracture, originally introduced by Bourdin et al. [24] in 2000 as a regularization of Francfort and Marigo's variational fracture formulation proposed in 1998 [23], has recently emerged as a transformative force in computational fracture mechanics, enabling new insights and capabilities in this field. The computational framework that arises from this variational Phase Field model eliminates the need for complex crack-tracking algorithms and additional criteria for managing phenomena such as crack branching or merging. As a result, the approach offers a unique flexibility in fracture simulations, which is likely a primary factor contributing to its success. Another

advantage of the Phase Field is its inherent ability to manage both crack nucleation and propagation. Nevertheless, the comprehension of the intrinsic nucleation criteria and the deliberation on their physical relevance are still complex and open issues. These aspects remain the focal points of ongoing debate within the Scientific Community.

Variational Phase Field models can be categorized as a distinct subset of gradient-damage models, incorporating a length-scale parameter. Γ-Convergence analyses indicate that as this parameter (length-scale) approaches zero, the global minimizers of the damage energy functional converge towards the global minimizers of energy for the sharp interface in Griffith model. In the context of rate-independent processes, this convergence principle extends to quasi-static evolutions through time-discretization, as elucidated by Giacomini [91]. However, it is crucial to note that this convergence is only achieved in terms of global minimizers, necessitating that the current state attains the lowest feasible energy level among all permissible alternatives at a given time increment. This concept of global minimization underpins the variational approach originally proposed by Francfort and Marigo [23] and plays a fundamental role mathematically, facilitating the application of direct methods in the calculus of variations. Nonetheless, the requirement for global minimality is incompatible with both experimental observations and numerical practices. Numerically, the pursuit of global minimization is impractical for large-scale computations, and existing numerical methods aim to identify local minimizers of the energy functional. Physically, local minimization – or meta-stability – emerges as a more fitting criterion for identifying states that are experimentally observable. These considerations were initially foreseen in the works by Bourdin et al. [24] and Francfort and Marigo [23], and have been elaborated upon in subsequent publications, see Francfort et al. [92] and additional Authors (e.g., Larsen [93]; Negri [94]).

Within the variational Phase Field framework, crack nucleation is synonymous with the localization of the Phase Field variable. In a quasi-static evolution, when local minimization is employed as the criterion for selecting stable states, such localization events correspond to the destabilization of a solution characterized by nearly uniform damage levels. The nucleation loading refers to the stage at which the existing solution branch no longer acts as a local minimum for the energy functional. Importantly, this nucleation load may not align with the critical load derived from an evolution law that employs global minimization as its stability criterion.

In the context of local minimization, the critical load is dependent on the internal length scale of the Phase Field model. Conversely, when global minimization is considered, the critical load converges to a value that is independent of this regularization length. Several researchers have adopted the concept of local minimization as a stability criterion, calibrating this internal length scale to induce

nucleation at a specific stress level under uniaxial conditions – essentially equating it to the known uniaxial tensile strength of the material at hand. This perspective, viewing the length scale as a material parameter, has been incorporated in multiple studies, including but not limited to those by Amor et al. [31], Borden et al. [95], Mesgarnejad et al. [96], Nguyen et al. [97], Pham et al. [29,98,99], Tanné et al. [28], and Wu et al. [100]. The influence of this length scale is analogous to the impact of the process zone size in cohesive fracture models. The investigation led by Tanné et al. [28] in 2018 stands as the most exhaustive study concerning crack nucleation under mode-I loading within the context of variational Phase Field models for brittle fracture. The authors posited that, given the aforementioned interpretation of the length scale and the utilization of local minimizers as a stability criterion, variational Phase Field models can accurately predict crack nucleation under mode-I conditions across a diverse array of geometries and notch types for various brittle materials.

Focusing on fatigue loading, in the current landscape of Phase Field fracture modeling, the phenomenon of fatigue is principally characterized by two key phenomenological considerations. These are predicated on the introduction of additional fatigue-related stored energies and dissipation potentials, which are functions of specific history variables. In the latter approach, a fatigue history variable is formulated as a locally accumulated quantity, serving as the argument for a fatigue degradation function that alters the dissipation potential relative to the static scenario. The primary distinctions among existing formulations lie in the definitions of the dissipation potentials and the fatigue history variables. In [101–103], the approach introduces an extra potential for fatigue dissipation that does not depend on the gradient of the Phase Field variable. Rather, this potential is determined by the Phase Field and fatigue history variables. These variables accumulate over time, reflecting changes in both damage and elastic strains. Within this framework, studies have been conducted to explore the effects of aging [102] and temperature [101] under cyclic loading conditions.

A novel approach to modeling fatigue failure, based on the variational Phase Field model, is presented in [104,105]. In this model, standard Phase Field dissipation potentials are modified to allow for a decrease in the material's fracture toughness as the corresponding fatigue scalar history variable increases. The accumulation of this fatigue history variable can be based on various factors, such as elastic strains [104], elastic strain energy density [105,106], or the notched-strain concept [107]. This innovative modification in modelling fracture resistance has led to the generation of phenomenological observations and curves that describe fatigue behavior, including the Wöhler curve, Paris law, and the Palmgren-Miner rule [105]. Recent extensions of this approach have incorporated considerations for residual stresses [108] and elasto-plastic deformations [109].

Conversely, the incorporation of fatigue effects is achieved by defining a fatigue-related stored energy term within the total energy of the system. In this context also, the uniqueness of the presented formulations relies on the specific definition of the fatigue-related stored energy and its associated dependencies. In reference [110], an auxiliary fatigue damage variable is introduced, whose evolution is empirically modeled in accordance with the Miner rule and the Chaboche concept. A corresponding fatigue-related energy term is then defined, which is a function of both this additional fatigue variable and the Phase Field variables. This formulation ultimately results in a fatigue driving force that appears in the Phase Field evolution equation, as well as an additional term in the constitutive relation accounting for fatigue-induced micro-stresses. In the study of fatigue behavior in rubber materials [111], the energetic contribution of the fatigue mechanism is dependent on the Phase Field variable and an accumulated history variable. This history variable is based on the elastic strain energy density. Separate from these two approaches, a novel framework is developed in [112] that employs a modified J-integral-based crack growth rate and stress intensity factor behavior. This modification serves to inform the kinetic law that governs the Phase Field evolution, offering yet another avenue for the study of fatigue phenomena. Considering the various models proposed based on the Phase Field approach under cyclic loading, it is noted that they have either not been validated or have been validated with limited experimental data due to high computational costs. In this thesis, a comprehensive validation and analysis of the model will be provided.

Chapter 3

Debonding Analyses of Direct Shear Tests[1]

3.1 Introduction

One effective approach to increase or restore the load-bearing capacity of an existing structure is the implementation of external reinforcements. Fiber-Reinforced Polymers (FRPs) are particularly advantageous in this context due to properties such as their high strength-to-weight ratio. More importantly, FRP plates and sheets have gained significant attention for their application in structural strengthening in recent years, largely due to their ease and speed of application. However, FRPs are not without limitations; they exhibit significant mechanical mismatch with the structure, and the epoxy resins possess poor fire resistance. To address these challenges, Fiber-Reinforced Cementitious Matrix (FRCM) composites have been recently considered, offering a promising alternative for structural reinforcement.

A crucial challenge in structural strengthening is preventing the debonding of FRP or FRCM from the existing structure, as this directly impacts the load-bearing capacity. The direct shear test, also known as the pull-push test, is commonly used to investigate debonding in such structures. In this test the material interface is mainly subjected to shear forces, minimizing the effects of peeling stress [80]. Notably, in the literature, the one-dimensional shear-lag model has been widely used for this test [113]. In this chapter, the shear-lag model is applied using four different approaches, each accounting for residual strength; an aspect which is particularly important in FRCM systems. In these systems, debonding generally occurs when the fiber net detaches from the cementitious matrix. The friction between the components is considered to contribute to residual strength. Regarding analytical investigations into the debonding process, various approaches have been adopted to model FRP-to-concrete joints. Yuan et al. [114] utilized a bilinear

[1] Some parts of this chapter have been adapted from our work previously published as "Mirzaei, A. M., Corrado, M., Sapora, A., and Cornetti, P., 2021, Analytical Modeling of Debonding Mechanism for Long and Short Bond Lengths in Direct Shear Tests Accounting for Residual Strength, Materials (Basel). 14(21)."

cohesive law (without accounting for residual strength) to model the pull-push test, while Cornetti and Carpinteri [115] employed a linear-exponential softening law for the same problem. This subject was further addressed by Biscaia et al. [116] using an exponential softening law. Additionally, D'Antino et al. [117] applied a trilinear cohesive crack model to experimental data concerning PBO FRCM composites [118]. In related studies, two simpler constitutive interface laws were implemented in [119,120] to tackle the same debonding problem. Cornetti et al. [79] adopted FFM [18] to analytically determine the delamination load during pull-push tests (without residual stress), revealing that FFM outcomes closely align with those obtained through cohesive crack models.

The primary objective of this investigation is to undertake a parametric study examining bond behavior in direct shear tests, with a focus on the influence of residual strength. The next section will elaborate mathematical formulations, providing closed-form expressions for load values during the debonding process, maximum debonding load relative to bond length, and effective bond length. These formulations will be derived by using three distinct interface cohesive laws and a finite fracture mechanics approach.

3.2 Mathematical modelling

To provide simple closed-form equations for parametric studies, a one-dimensional model is considered, which can be applied to various strengthening systems, as depicted in Fig. 3-1. These systems include: (a) FRP plates, (b) Near Surface Mounted (NSM) reinforcements, (c) embedded bars, and (d) FRCM systems. Given that both the total area and the perimeter of the reinforcement differ depending on the specific case, the equations are derived to be universally applicable across all geometries. For illustrative clarity, let us focus on the geometry in Fig. 3-1(a). However, the validation using experimental data will specifically focus on FRCM tests, denoted as geometry (d), where the influence of residual strength, which is the main focus in this study, is most pronounced.

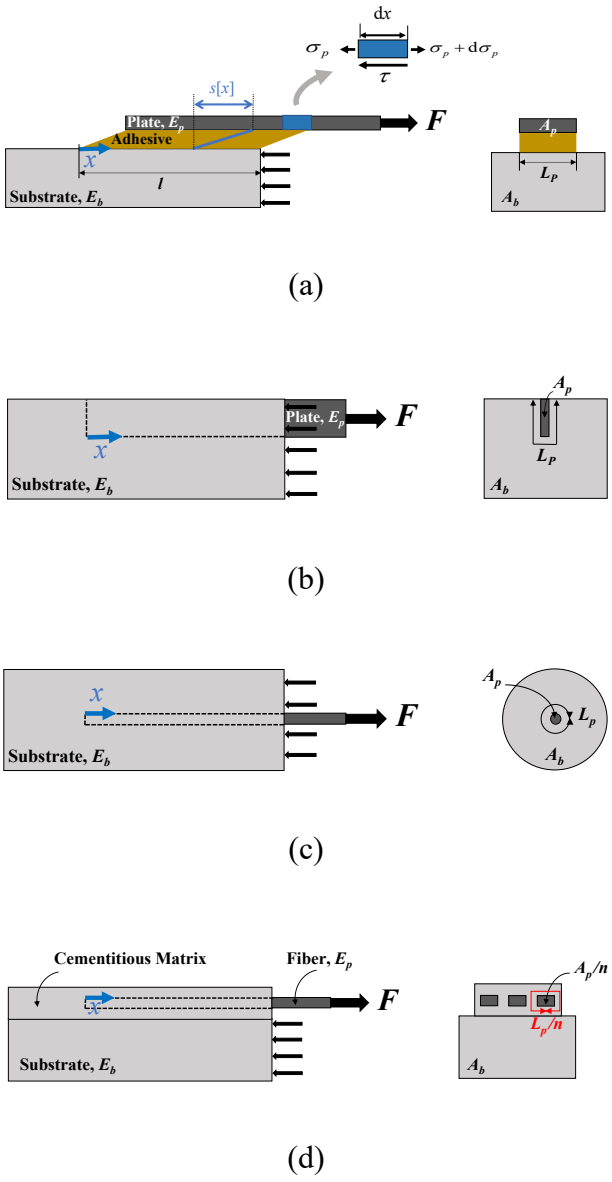

Fig. 3-1. Schematic representation of direct shear tests for various strengthening systems: (a) Externally Bonded FRP Plate, (b) NSM Reinforcement, (c) Embedded Bar, (d) FRCM Strengthening System Featuring $n = 3$ Longitudinal Fibers. To simplify the illustration, details of the adhesive layer are enlarged and provided only in configuration (a), while constraints designed to prevent block uplifting are omitted for clarity.

To formulate the governing equation for this problem, the horizontal equilibrium equations can be employed for an arbitrary element within the reinforcement and for the composite system of the reinforcement and substrate (see Fig. 3-1(a), [121]):

$$A_p \, \mathrm{d}\sigma_p - \tau \, L_p \, \mathrm{d}x = 0 \tag{3-1}$$

$$\sigma_p \, A_p + \sigma_b \, A_b = 0 \tag{3-2}$$

In this formulation, the subscripts p and b denote the reinforcement and the substrate block, respectively. The parameters A_p and A_b illustrate the cross-sectional areas of the reinforcement and the substrate, while L_p represents the bonded perimeter. Linear elastic behavior is assumed for all components. Using σ for normal stress, E for Young's modulus, and u for displacement along the longitudinal axis x, the stress-strain relationship can be expressed as $\sigma_i = E_i \, (\mathrm{d}u_i / \mathrm{d}x)$, where $i = p, b$. The shear stress at the interface between the substrate and the reinforcement is denoted by τ. Employing analytical manipulation, these relations yield the following governing second-order differential equation:

$$\frac{\mathrm{d}^2 s}{\mathrm{d}x^2} - L_p \frac{1+\rho}{E_p \, A_p} \tau[s] = 0 \tag{3-3}$$

In this formulation, $\rho = E_p \, A_p \, / \, E_b \, A_b$ represents the mechanical fraction of the reinforcement relative to the substrate. Additionally, s denotes the relative longitudinal displacement between the reinforcement and the substrate, expressed as $s = u_p - u_b$. The normal stress within the reinforcement is described as follows:

$$\sigma[s] = \sigma_p[s] = \frac{E_p}{1+\rho} \frac{\mathrm{d}s}{\mathrm{d}x} \tag{3-4}$$

For further details regarding the mathematical manipulations, refer to [122]. In Eq. (3-3), the bond-slip law, $\tau[s]$, is considered as an inherent property of the bonding system, serving as a constitutive (cohesive) law for the interface. This study explores three distinct cohesive law models: the Equivalent-Linear Elastic Brittle Interface Model (EL), the Dugdale Model (DM), and the Rigid-Linear Softening Model (RL). Additionally, a fourth approach using Rigid Finite Fracture Mechanics Model (RF) is included. All models take into account the presence of residual strength. Subsequent sub-sections will introduce and apply each model to the analysis of reinforcement debonding. It is noteworthy that these models are all based on three key parameters: the fracture energy, G_c, the shear strength, τ_c, and the residual strength, τ_r.

3.2.1 Equivalent- Linear Elastic Brittle Interface Model (EL)

Utilizing the Equivalent-Linear Elastic Brittle Interface Model, the interface is modeled as an array of linear springs, each characterized by a stiffness represented by *k*. Eq. (3-5) outlines the governing constitutive law for this interface.

$$\tau[s]=\begin{cases} k\,s, & s \le s_f \\ \tau_r, & s > s_f \end{cases} \tag{3-5}$$

In this formulation, s_f refers to the final relative displacement which can be defined as the displacement at which the shear stress drops to the residual strength level. Given that the primary governing equation (Eq. (3-3)) is a second-order differential equation, two boundary conditions are required for obtaining the relative displacement, *s*. In accordance with Fig. 3-2 and Eq. (3-4), the boundary conditions can be set as:

$$\sigma[0]=0 \rightarrow s'[0]=0 \tag{3-6}$$

$$\sigma[l-a]=\frac{F-\tau_r\,a\,L_p}{A_p} \qquad \rightarrow \qquad s'[l-a]=\frac{1+\rho}{E_p\,A_p}\left(F-\tau_r\,a\,L_p\right) \tag{3-7}$$

In this equation, *a* represents the length of the debonded or cracked region, where the stress distribution remains constant at τ_r. Based on these boundary conditions, the relative displacement can be expressed as:

$$\begin{aligned} s[x]=&\left(F-a\,L_p\,\tau_r\right)\sqrt{\frac{1+\rho}{E_p\,A_p\,L_p\,k}} \\ &\times \operatorname{csch}\left[(l-a)\sqrt{\frac{k\,L_p(1+\rho)}{E_p\,A_p}}\right]\cosh\left[x\sqrt{\frac{k\,L_p(1+\rho)}{E_p\,A_p}}\right] \end{aligned} \tag{3-8}$$

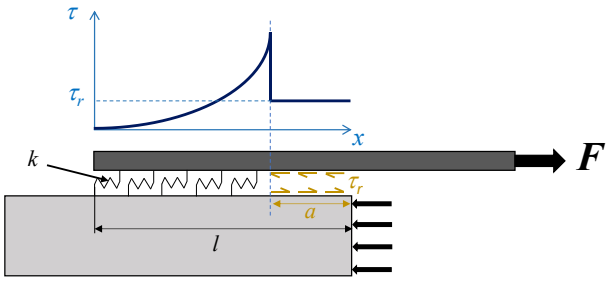

Fig. 3-2. Distribution of shear stress along the interface for a debonding crack of length *a*.

The associated stress can be determined by multiplying Eq. (3-8) by the interface stiffness, *k*. The maximum stress occurs at the boundary between the undamaged area and the frictional region, specifically at $x = l–a$.

$$\tau_{\max} = k\, s[l-a] = \left(F - a\, L_p\, \tau_r\right)\sqrt{\frac{k(1+\rho)}{E_p\, A_p\, L_p}}\,\coth\left[(l-a)\sqrt{\frac{k\, L_p(1+\rho)}{E_p\, A_p}}\right] \tag{3-9}$$

Note that Eqs. (3-8) and (3-9) are applicable for any value of *k*. The current model is termed *Equivalent* because, unlike in the Linear Elastic Brittle Interface Model where the interface stiffness *k* is an independent parameter, in the EL model *k* is dependent on other interface properties as indicated in Eq. (3-11). Specifically, in the EL model (refer to Fig. 3-3(a)), both the stiffness *k* and the final displacement s_f are functions of $\mathcal{G}_c$, τ_c, and τ_r as follows:

$$s_f = \frac{2\,\tau_c\,\mathcal{G}_c}{(\tau_c - \tau_r)^2} \tag{3-10}$$

$$k = \frac{(\tau_c - \tau_r)^2}{2\,\mathcal{G}_c} \tag{3-11}$$

The bond-slip, τ-s, behavior of the interface, as modeled by the EL approach, is illustrated in Fig. 3-3(a).

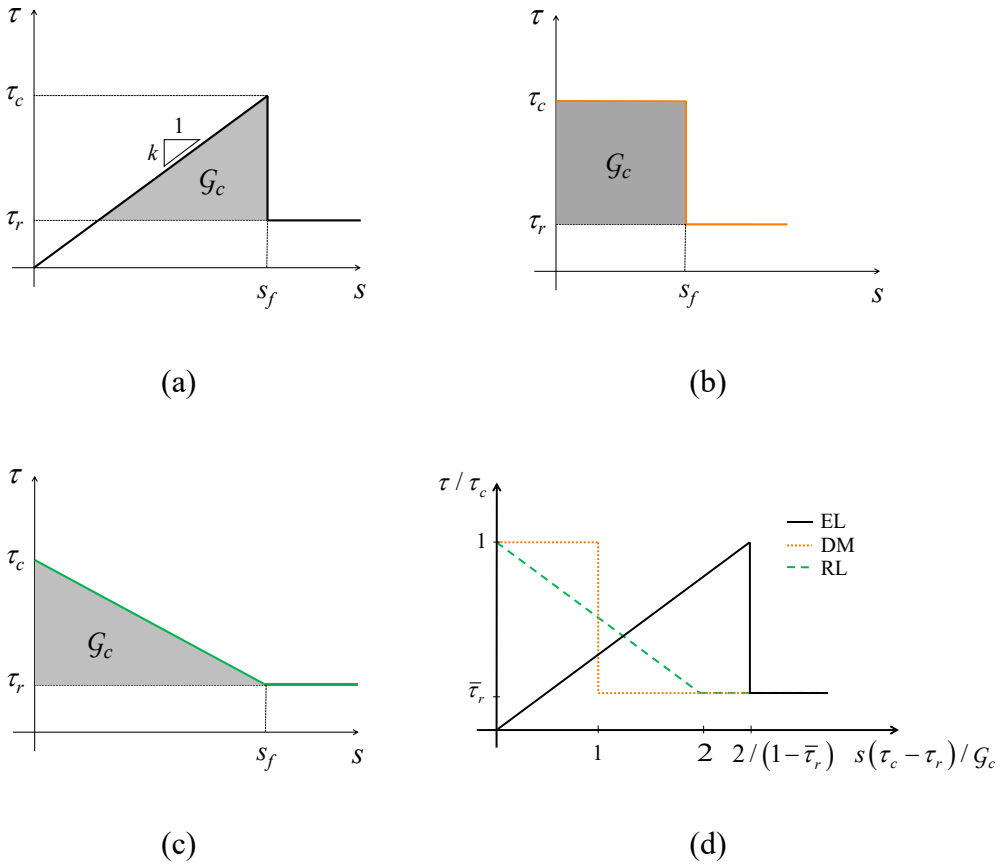

Fig. 3-3. Cohesive laws for the interface based on: (a) Equivalent Linear Elastic Brittle Interface Model (EL), (b) Dugdale Model (DM), (c) Rigid Linear Softening Model (RL). (d) A dimensionless comparison of the models.

It is worth noting that to justify the utilization of the grey area as the interface's fracture energy, one can assess the work needed for crack closure in an infinitesimal step. The stress needed to close the crack is $\tau_c - \tau_r$, and the corresponding displacement is $(\tau_c - \tau_r) / k$. This accounts for the grey triangle observed in Fig. 3-3(a), as corroborated by [120,123,124]. Similarly, the strain energy release rate $\mathcal{G}$ represents the elastic energy released by the spring at the crack tip. Therefore:

$$\mathcal{G} = \frac{(\tau_{max} - \tau_r)^2}{2k}, \quad \mathcal{G}_c = \frac{(\tau_c - \tau_r)^2}{2k} \tag{3-12}$$

Crack propagation takes place when $\mathcal{G}$ meets $\mathcal{G}_c$. In light of Eq. (3-12), this essentially means that the crack grows when $\tau_{max}=\tau_c$. Before advancing further, it is convenient to normalize the variables involved by introducing reference load and length values. The reference load can be defined as:

$$F_c^{\infty} = \sqrt{\frac{2 G_c E_p A_p L_p}{1+\rho}} \tag{3-13}$$

It can be demonstrated that, in scenarios lacking residual strength, F_c^{∞} serves as the upper limit for the debonding load, typically attained for infinite (very large) bond lengths. This maximum is not a function of the bond-slip law, and solely depends on the fracture energy, as supported by different studies such as Cornetti et al. [79].

Accordingly, the characteristic length is specified as follows:

$$l_{ch} = \frac{F_c^{\infty}}{\tau_c L_p} = \frac{1}{\tau_c}\sqrt{\frac{2 G_c E_p A_p}{(1+\rho) L_p}} \tag{3-14}$$

Eq. (3-14) demonstrates that l_{ch} serves as the bond length that can withstand F_c^{∞} under conditions of uniform interfacial shear stress distribution equal to the interface shear strength, τ_c.

Dimensionless auxiliary variables may now be introduced in the following manner:

$$\bar{F} = \frac{F}{F_c^{\infty}}, \quad \lambda = \frac{l}{l_{ch}}, \quad \alpha = \frac{a}{l_{ch}}, \quad \bar{\tau}_r = \frac{\tau_r}{\tau_c} \tag{3-15}$$

Therefore, the debonding load can be rewritten as:

$$\bar{F} = \frac{\tanh\left[(\lambda-\alpha)(1-\bar{\tau}_r)\right]}{1-\bar{\tau}_r} + \alpha\,\bar{\tau}_r \tag{3-16}$$

3.2.1.1 Maximum load vs. bond length

The maximum load during debonding, F_c, is a critical design parameter as it dictates the ultimate load-bearing capacity of the joint. Upon examination of Eq. (3-16), it becomes evident that this maximum load is attained at the initiation of the crack ($a = 0$) when the bond length falls below a certain threshold, denoted as $\lambda < \lambda_{lim}$, where:

$$\lambda_{lim} = \frac{1}{\left(1-\bar{\tau}_{\mathrm{r}}\right)} \operatorname{arccosh}\left[\frac{1}{\sqrt{\bar{\tau}_{\mathrm{r}}}}\right] \tag{3-17}$$

For bond lengths exceeding λ_{lim}, the crack length at which the maximum load is attained can be determined by setting the derivative of the debonding load, as per Eq. (3-16), with respect to the crack length a to zero. Thus, the crack length that maximizes the load is given by:

$$\alpha = \lambda - \lambda_{lim} \tag{3-18}$$

Consequently, the maximum or critical load F_{c} can be obtained by substituting Eq. (3-18) into Equation (3-16). To summarize, according to the EL, the expression for the maximum load is as follows:

$$\bar{F}_{\mathrm{c}} = \frac{F_{\mathrm{c}}}{F_{\mathrm{c}}^{\infty}} = \begin{cases} \dfrac{1}{1-\bar{\tau}_{\mathrm{r}}} \tanh\left[\lambda\left(1-\bar{\tau}_{\mathrm{r}}\right)\right], & \lambda \le \lambda_{lim} \\ \dfrac{1}{\sqrt{1-\bar{\tau}_{\mathrm{r}}}} + \bar{\tau}_{\mathrm{r}}\left(\lambda - \lambda_{lim}\right), & \lambda > \lambda_{lim} \end{cases} \tag{3-19}$$

It should be noted that in dimensionless terms, the maximum load is solely dependent on the normalized bond length and the ratio between the residual and undamaged strengths. This characteristic is consistent across the subsequent models discussed. The relationship between the maximum load and bond length, according to Eq. (3-19), is graphically represented in Fig. 3-4 for $\bar{\tau}_r$ = 0, 0.15. In the figure, the limit value of the bond length, λ_{lim}, is depicted for $\bar{\tau}_r$ = 0.15, while it approaches infinity for $\bar{\tau}_r$ = 0.

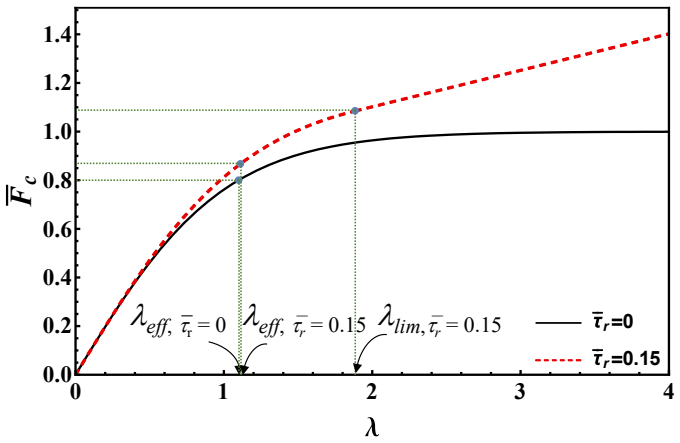

Fig. 3-4. Graphical representation of the maximum load as a function of bond length according to EL for $\bar{\tau}_r$ = 0, 0.15.

3.2.1.2 Effective Bond Length

Fig. 3-4 reveals that the maximum load experiences a sharp increase for smaller values of bond length, subsequently showing a decline in slope until reaching a constant value for bond lengths greater than the limit value, as indicated in Eq. (3-17). In the regime of small bond lengths, the slope is proportional to the undamaged strength, τ_c, whereas for longer bond lengths, the slope correlates with the residual strength τ_r.

To address this behavior, it is useful to introduce the concept of an effective bond length. This is a length beyond which any increment in the load is constrained. In the context of the EL, it is not advisable to equate the effective bond length with the limit bond length from Eq. (3-17), as the latter becomes infinite when τ_r approaches zero. A more practical approach is to define the effective length as the bond length that can sustain β percent of the load at the transitional point between short and long bond lengths, denoted as λ_{lim}. Further analytical work leads to the following expression for the effective bond length:

$$\lambda_{eff} = \frac{1}{1-\bar{\tau}_r}\,\mathrm{Arctanh}\left[\beta\sqrt{1-\bar{\tau}_r}\right] \tag{3-20}$$

In the EL model, the effective bond length is evidently dependent on β. Given that the value of Arctanh[1] is infinite, selecting high β values (nearing unity) may yield impractically large effective bond lengths. To mitigate this and generate realistic estimates of effective bond lengths by considering the residual strength, a β value of 80% was selected. This choice is illustrated in Fig. 3-4, where the

effective bond lengths are accentuated for both frictionless and frictional cases, $\bar{\tau}_r = 0, 0.15$.

Though the EL model has been previously introduced in existing literature, the present study offers an original contribution through Eq. (3-19), which presents the critical load. Additionally, the method for determining the effective bond length, as outlined in Eq. (3-20), is postulated to be more accurate. This updated approach incorporates friction, thus potentially providing a more reliable estimate than the simplified $\lambda_{eff} \cong 4$ presented in [119,120].

3.2.2 Dugdale Model (DM)

In the DM, it is assumed that a constant shear stress, τ_c, is presented within the cohesive process zone. Once the relative displacement s attains its critical threshold s_f, debonding happens, causing the shear stress to drop to the residual strength τ_r.

$$\tau[s] = \begin{cases} \tau_c, & s \le s_f \\ \tau_r, & s > s_f \end{cases} \tag{3-21}$$

and

$$s_f = \frac{\mathcal{G}_c}{\tau_c - \tau_r} \tag{3-22}$$

The bond-slip relationship based on the DM is depicted in Fig. 3-3(b). Similarly, the shaded area illustrates the fracture energy of the interface.

For the calculation of the fracture load during debonding, the initial step is to obtain the minimum bond length necessary for a fully developed process zone. Appropriate boundary conditions for this computation are traction-free and no-slip conditions at $x = 0$.

$$s[0] = 0 \tag{3-23}$$

$$\sigma[0] = 0 \rightarrow s'[0] = 0 \tag{3-24}$$

Utilizing Eqs. (3-3) and (3-21) (for $s < s_f$) along with the boundary conditions (3-23) and (3-24), the distribution of slip is determined as follows:

$$s[x]=\frac{x^2(1+\rho)\tau_c L_p}{2E_p A_p} \tag{3-25}$$

For a fully developed process zone, the necessary bond length can be determined using the condition that at the end of this length, the relative slip equals s_f, as depicted on the left side of Fig. 3-5. Notably, in this figure, the area beneath the curve of shear stress distribution illustrates the debonding load. Furthermore, for bond lengths exceeding the fully developed process zone, subsequent increases in load are minimal (as seen in stages (c) to (e) in Fig. 3-5) and are attributable only to residual strength. As a result, this length can be designated as the effective bond length l_{eff} for the DM model. Therefore, by setting $s[l_{eff}] = s_f$ and applying Eqs. (3-14), (3-22) and (3-25), the effective bond length is determined as follows:

$$\lambda_{eff}=\frac{l_{eff}}{l_{ch}}=\frac{1}{\sqrt{1-\bar{\tau}_r}} \tag{3-26}$$

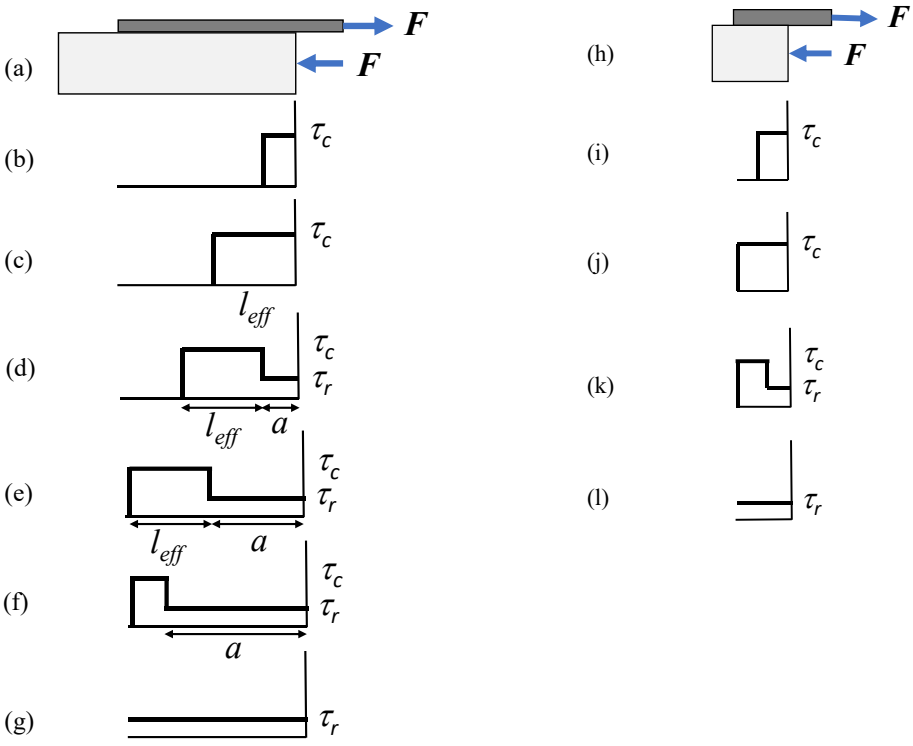

Fig. 3-5.The shear stress distribution across various debonding stages according to the DM. Stages (a) to (g) correspond to long bond lengths ($l > l_{eff}$), whereas stages (h) to (l) are applicable for short bond lengths ($l < l_{eff}$).

Considering conditions described above, two distinct scenarios appear: one for long bond lengths ($l > l_{\text{eff}}$), represented on the left side of Fig. 3-5, and another for short bond lengths ($l < l_{\text{eff}}$), represented on the right side of the figure. Considering long bond lengths, subsequent calculations reveal that the load during the debonding (stages (c) to (g)) can be calculated as follows:

$$\bar{F} = \begin{cases} \dfrac{1}{\sqrt{1-\bar{\tau}_r}} + \alpha\,\bar{\tau}_r, & 0 < \alpha \le \lambda - \lambda_{eff} \\ (\lambda - \alpha) + \alpha\,\bar{\tau}_r, & \lambda - \lambda_{eff} < \alpha < \lambda \end{cases} \tag{3-27}$$

3.2.2.1 Maximum load vs. bond length

According to Eq. (3-27), the maximum load is attained when α is equal to ($\lambda - \lambda_{eff}$), corresponding to stage (e) in Fig. 3-5, left column. Conversely, for short bond lengths, the maximum load is realized at the onset of debonding, specifically at stage (j) in Fig. 3-5, right column. Therefore, the following expression holds:

$$\bar{F}_c = \frac{F_c}{F_c^{\infty}} = \begin{cases} \lambda, & \lambda \le \lambda_{eff} \\ \dfrac{1}{\sqrt{1-\bar{\tau}_r}} + \bar{\tau}_r\left(\lambda - \lambda_{eff}\right), & \lambda > \lambda_{eff} \end{cases} \tag{3-28}$$

In Fig. 3-6, the relationship between maximum load and bond length for $\bar{\tau}_r = 0$, 0.15 is depicted based on Eq. (3-28). The effective bond length, λ_{eff}, is also marked in the figure for reference. It is noteworthy to mention that the maximum load corresponding to the limit/effective bond length based on EL and DM models is identical and exceeds F_c^{∞} when friction is taken into account.

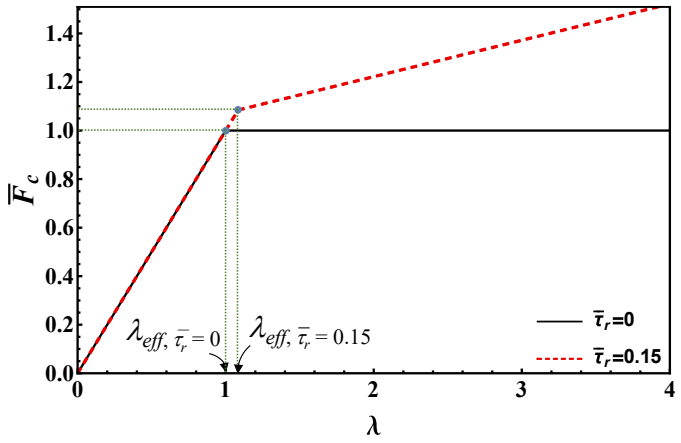

Fig. 3-6. Graphical representation of the maximum load as a function of bond length according to DM for $\bar{\tau}_r$ = 0, 0.15.

3.2.3 Rigid-Linear Softening Model (RL)

In the RL, depicted in Fig. 3-3(c), the interface exhibits a linear softening behavior. Specifically, the shear stress decreases linearly from τ_c to τ_r as the relative displacement, s, transitions from 0 to s_f. The bond-slip law governing this behavior in the RL model is expressed as follows:

$$\tau[s]=\begin{cases}\tau_c-(\tau_c-\tau_r)\dfrac{s}{s_f}, & s\le s_f\\ \tau_r, & s>s_f\end{cases} \tag{3-29}$$

The final (relative) displacement based on RL model can be written as:

$$s_f=\frac{2\,G_c}{\tau_c-\tau_r} \tag{3-30}$$

Similar to DM, to calculate the debonding load in the RL, it is necessary to first establish the minimum bond length for a fully developed softening zone, denoted as l_{eff}. The boundary conditions applied are no-slip and traction-free at x = 0, as specified in Eqs. (3-23) and (3-24). By employing the RL constitutive law for $s < s_f$, Eq. (3-29), and inserting it into the governing Eq. (3-3), the distributions of relative slip and shear stress along the interface can be derived as follows:

$$s[x]=s_f\frac{1-\cos\left[\dfrac{x}{l_{ch}}(1-\bar{\tau}_r)\right]}{1-\bar{\tau}_r} \tag{3-31}$$

$$\tau[x] = \tau_c \cos\left[\frac{x}{l_{ch}}\left(1-\bar{\tau}_r\right)\right] \tag{3-32}$$

Fig. 3-7 illustrates the distribution of shear stresses at various stages of debonding according to the RL.

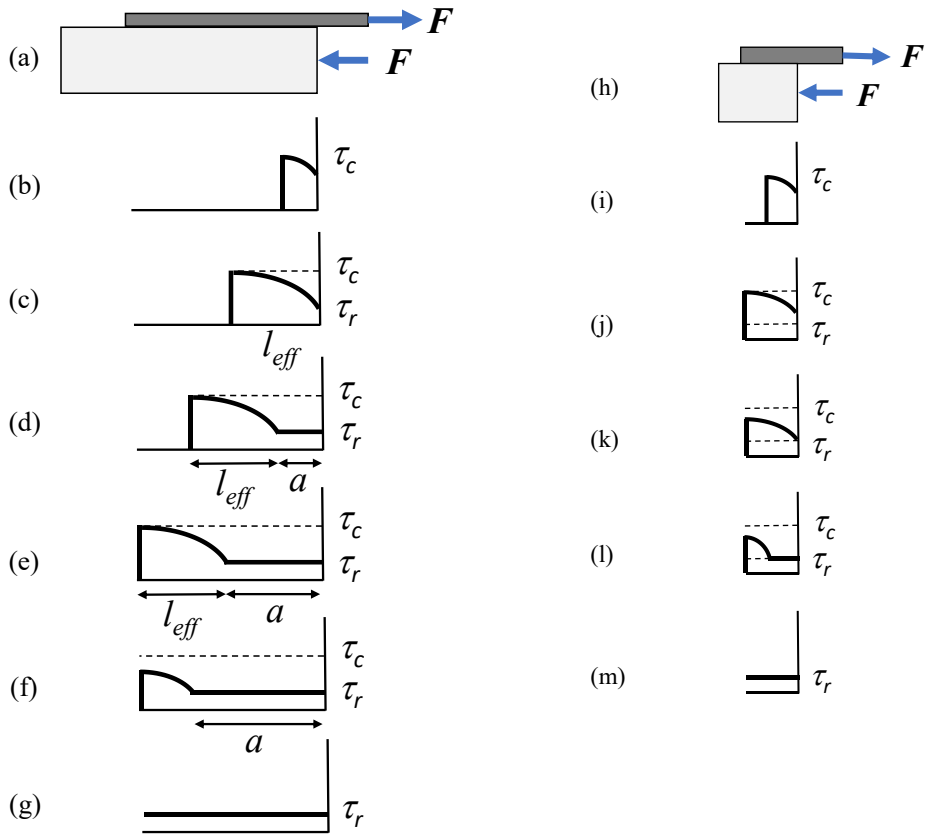

Fig. 3-7. The shear stress distribution across various debonding stages according to the RL. Stages (a) to (g) correspond to long bond lengths ($l > l_{eff}$), whereas stages (h) to (m) are applicable for short bond lengths ($l < l_{eff}$).

For the RL model, the length required for a completely developed softening zone, l_{eff}, can be determined by setting $s[l_{eff}] = s_f$ in Eq. (3-31). Alternatively, this length can also be obtained by setting $\tau[l_{eff}] = \tau_r$ in Eq. (3-32). Consequently, the expression for l_{eff} can be formulated as follows:

$$\lambda_{eff} = \frac{l_{eff}}{l_{ch}} = \frac{\arccos\left[\bar{\tau}_r\right]}{1-\bar{\tau}_r} \tag{3-33}$$

For bond lengths greater than $l > l_{eff}$ (as illustrated on the left side of Fig. 3-7, the applied load during the stages of debonding (from stage stages (c) to (e)) can be calculated using the following equation:

$$\bar{F} = \frac{F}{F_c^{\infty}} = \frac{L_p \int_0^{l_{eff}} \tau[x]\,\mathrm{d}x + \tau_r\, a\, L_p}{\tau_c\, l_{ch}\, L_p} = \sqrt{\frac{1+\bar{\tau}_r}{1-\bar{\tau}_r}} + \alpha\,\bar{\tau}_r, \qquad 0 < \alpha \le \lambda - \lambda_{eff} \tag{3-34}$$

For stages (e) to (g), where $\alpha > \lambda - \lambda_{eff}$, solving Eq. (3-3) within the softening zone is required (employing Eq. (3-29) for the constitutive behavior). The related boundary conditions for this scenario are described by Eq. (3-24) alongside the following additional condition:

$$s\left[l-a\right] = s_f \tag{3-35}$$

Consequently, the relative slip $s[x]$ for $0 < x < l-a$ is obtained. Its derivative evaluated at the right boundary reads:

$$s'\left[l-a\right] = \frac{s_f}{l_{ch}}\,\bar{\tau}_r\,\tan\left[\frac{l-a}{l_{ch}}\left(1-\bar{\tau}_r\right)\right] \tag{3-36}$$

Following the solution of Eq. (3-3) in the frictional zone – employing the second row of Eq. (3-29) and utilizing the boundary conditions expressed in Eqs. (3-35) and (3-36) – continuity in stress and displacement at $x = l-a$ is ensured. Consequently, the relative slip $s[x]$ for the interval $l-a < x < l$ is determined. By assessing its derivative at the loaded end, the applied load for stages (e) to (g) can ultimately be computed using Eq. (3-4).

$$\bar{F} = \frac{\bar{\tau}_r}{1-\bar{\tau}_r}\tan\left[\left(\lambda-\alpha\right)\left(1-\bar{\tau}_r\right)\right] + \alpha\,\bar{\tau}_r, \qquad \lambda - \lambda_{eff} < \alpha < \lambda \tag{3-37}$$

Eqs. (3-34) and (3-37) delineate the behavior of the applied load during the debonding process as specified by the RL.

3.2.3.1 Maximum load vs. bond length

For bond lengths that are less than the effective bond length $\lambda < \lambda_{eff}$, it is evident from Fig. 3-7 (right column) that the peak load is reached at stage (j). At this stage,

the entire interface undergoes softening, and the shear stress at the origin is $\tau[0] = \tau_c$. This can be expressed by employing Eq. (3-32).

$$F_c = L_p \int_0^l \tau[x]\,\mathrm{d}x = \frac{\sin\left[\lambda\left(1-\bar{\tau}_r\right)\right]}{1-\bar{\tau}_r}\tau_c\, l_{ch}\, L_p \tag{3-38}$$

For long bond lengths where $\lambda > \lambda_{eff}$, the peak load is attained at stage (e). The value of the maximum load can be determined by substituting $\alpha = \lambda - \lambda_{eff}$ into either Eq. (3-34) or Eq. (3-38). In summary, the equation for the maximum load can be represented as follows:

$$\bar{F}_c = \frac{F_c}{F_c^{\infty}} = \begin{cases} \dfrac{1}{1-\bar{\tau}_r}\sin\left[\lambda\left(1-\bar{\tau}_r\right)\right], & \lambda \le \lambda_{eff} \\ \sqrt{\dfrac{1+\bar{\tau}_r}{1-\bar{\tau}_r}} + \bar{\tau}_r\left(\lambda - \lambda_{eff}\right), & \lambda > \lambda_{eff} \end{cases} \tag{3-39}$$

The behavior of maximum load versus bond length based on the RL model is depicted in Fig. 3-8, utilizing Eq. (3-39) for $\bar{\tau}_r$ = 0, 0.15. Notably, the maximum load associated with the effective bond length – represented by the first term in the second row of Eq. (3-34) – is higher in the RL model than those predicted by either the EL or DM models.

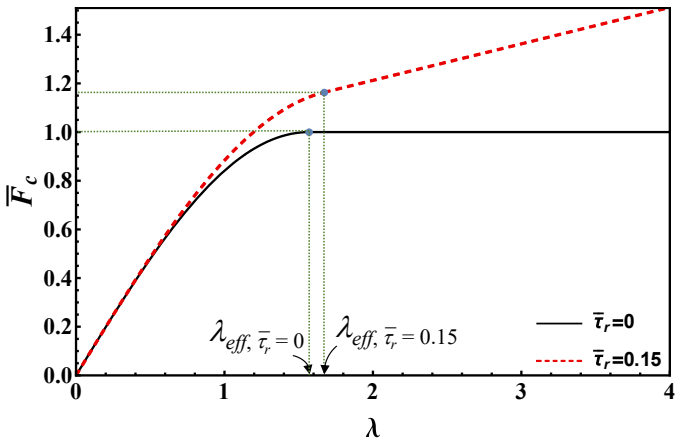

Fig. 3-8. Graphical representation of the maximum load as a function of bond length according to RL for $\bar{\tau}_r$ = 0, 0.15.

3.2.4 Rigid-Finite Fracture Mechanics Model (RF)

In this section, FFM is employed to examine the debonding process during the direct shear test. Although the model has been introduced previously, key parameters are presented again for the sake of completeness. As mentioned, in FFM, crack propagation is assumed to occur in discrete increments, denoted by l_c. The discrete energy balance for such a test can be written as:

$$L_p \int_a^{a+l_c} \mathcal{G}(a')\,\mathrm{d}a' \geq \mathcal{G}_c\, L_p\, l_c \tag{3-40}$$

To facilitate both simplicity and a basis for comparison with rigid Cohesive Zone Models, such as DM and RL, a rigid interface is also considered for this model. This can be achieved by utilizing Eqs. (3-9) and (3-11) and setting $k \to \infty$:

$$\mathcal{G} = \frac{(\tau_{max} - \tau_r)^2}{2\,k} \underset{k\to\infty}{=} \frac{1+\rho}{2E_p\, A_p\, L_p}\left(F - a\, L_p\, \tau_r\right)^2 \tag{3-41}$$

By inserting Eq. (3-41) into Eq. (3-40), the dimensionless form of the equation is derived as follows:

$$\bar{F}^2 - \bar{\tau}_r(2\alpha+\delta)\bar{F} + \bar{\tau}_r^2(3\alpha^2 + 3\alpha\delta + \delta^2) \geq 1 \tag{3-42}$$

In this equation, $\delta = l_c/l_{ch}$. The second (stress) condition for crack propagation stipulates that the average stress exerted over the crack advancement, l_c, must exceed the interfacial strength, τ_c. Given that the interface is characterized as rigid, the force within the plate is transferred to the block precisely at the crack tip, ($x = l–a$). Therefore, the stress criterion is determined as follows:

$$\frac{F - \tau_r\, a\, L_p}{L_p\, l_c} \geq \tau_c \tag{3-43}$$

Employing Eq. (3-42), in conjunction with the dimensionless from of Eq. (3-43), provides the debonding load. This load can be regarded as the minimum value that fulfills the system of inequalities:

$$\begin{cases} \overline{F} \geq \left((\alpha + \delta/2)\overline{\tau}_r + \sqrt{1 - (\overline{\tau}_r \delta)^2/12} \right) \mathrm{H}\left[(\lambda - \alpha) - \delta \right] \\ \overline{F} \geq \delta + \overline{\tau}_r \alpha \end{cases} \tag{3-44}$$

The inclusion of the Heaviside function H[·] in the system of inequalities accounts for the special case of complete failure, where $l_c = l–a$. In this situation, the energy condition is inherently satisfied.

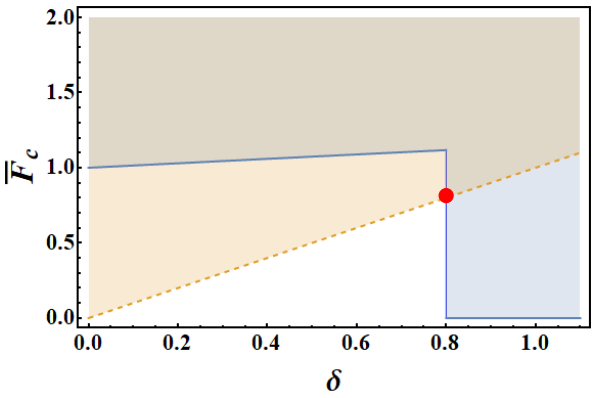

(a)

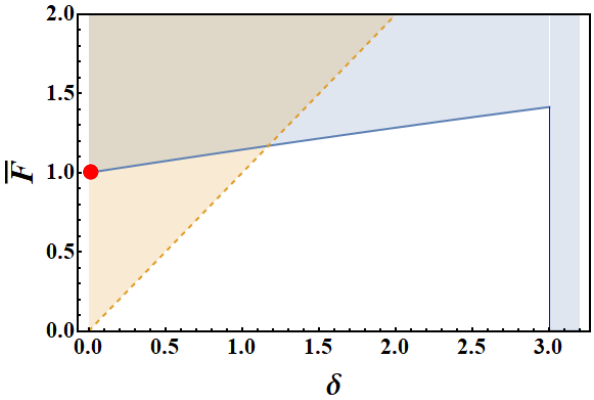

(b)

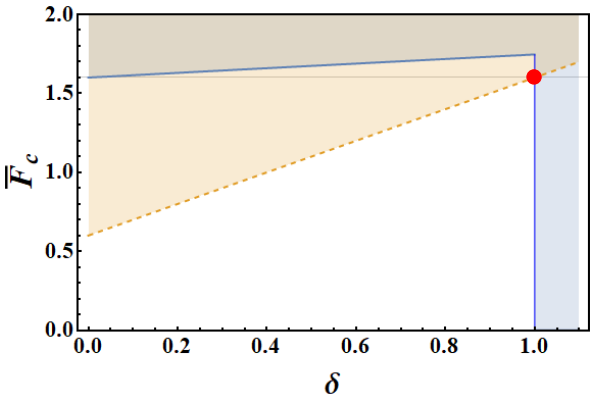

(c)

Fig. 3-9. Graphical depiction of inequality system: continuous lines indicate the energy condition (first inequality), while dashed lines show the stress requirement (second inequality). The red dot marks the minimum load, identifying the debonding load and corresponding crack growth. Normalized load vs. crack advance per RF model for (a) short bond length ($\lambda = 0.8$) at debonding onset ($\alpha = 0$); (b) long bond length ($\lambda = 3$) at debonding onset ($\alpha = 0$, stable crack growth); (c) long bond length ($\lambda = 3$) at maximum load ($\alpha = 2$) where crack growth becomes unstable. For all the cases, it is assumed that $\bar{\tau}_r = 0.3$.

To identify the maximum load, F_c, during the debonding process, two scenarios can be employed. The first scenario occurs when the normalized bond length, λ, is less than 1. In this case, the maximum load is attained at the onset of debonding, $\alpha = 0$, as illustrated in Fig. 3-9(a). The corresponding dimensionless load $\bar{F}_c$ is $\delta = \lambda$, and crack propagation occurs in an unstable manner under load control, leading to instantaneous debonding across the entire interface. Conversely, for long bond lengths where $\lambda > 1$, the minimum point of the system in Eq. (3-44) is realized for infinitesimal crack growth $\delta = 0$ and a dimensionless unit load, as shown in Fig. 3-9(b). In this scenario, the debonding process is stable as the load required for debonding increases with the crack length a. However, as demonstrated in Fig. 3-9(c), the debonding becomes unstable when α attains the value λ–1. At this point, the crack increment, δ, jumps from 0 to 1. The corresponding maximum load in this case is $\bar{F}_c = 1 + \bar{\tau}_r (\lambda - 1)$.

Based on the observations made earlier, it is evident that for long bond lengths, the debonding load is determined by the energy condition (the first equation in system (3-44)) with an infinitesimal crack increment $\delta = 0$ as long as $\alpha < \lambda - 1$. Conversely, the stress condition (the second equation in system (3-44)) governs when $\alpha > \lambda - 1$, where the crack advance is equal to the ligament ($\delta = \lambda - \alpha$).

$$\bar{F} = \begin{cases} 1 + \alpha \bar{\tau}_r, & \alpha \le \lambda - 1 \\ (\lambda - \alpha) + \alpha \bar{\tau}_r, & \alpha > \lambda - 1 \end{cases} \tag{3-45}$$

It should be noted that the second row in Eq. (3-45)(3-44) is consistent with the corresponding term in the DM.

3.2.4.1 Maximum load vs. bond length

Based on the prior analysis, the relationship between maximum load and bond lengths is as follows:

$$\bar{F}_c = \frac{F_c}{F_c^{\infty}} = \begin{cases} \lambda, & \lambda \le 1 \\ 1 + \bar{\tau}_r (\lambda - 1), & \lambda > 1 \end{cases} \tag{3-46}$$

Eq. (3-46) is depicted in Fig. 3-10 to show the relationship between maximum load and bond length based on RF model for $\bar{\tau}_r = 0, 0.15$. The RF model consistently yields an effective bond length of unity ($\lambda_{eff} = 1$), making it independent of residual strength. The maximum load corresponding to this effective bond length is F_c^{∞}, which is lower than the predictions by previous models.

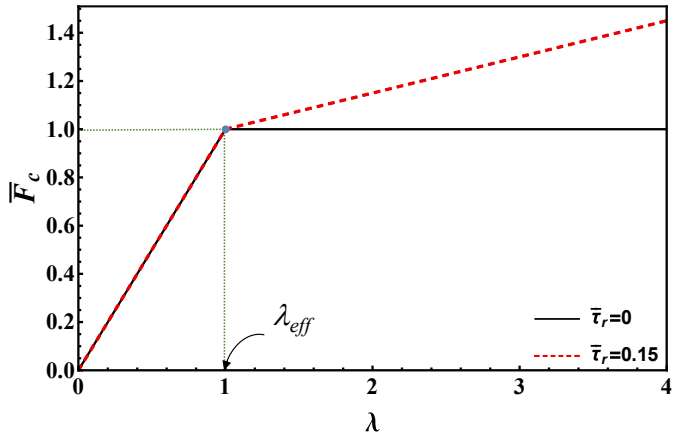

Fig. 3-10. Graphical representation of the maximum load as a function of bond length according to RL for $\overline{\tau}_r$ = 0, 0.15.

3.3 Results and discussion

This section explores parametric studies focusing on the impact of residual strength and bond length on the maximum debonding load. Furthermore, the relationships involving effective bond length are revisited more closely. The variations in load during the debonding process are evaluated based on different theoretical models. Finally, the results of the theoretical equations are compared with experimental data from the literature for validation.

3.3.1 Maximum debonding load vs. bond length

The maximum debonding load is graphically represented in Fig. 3-11, considering different models: EL, DM, RL, and RF. In this figure, the effective bond length for each model is shown by red lines. Additionally, in Fig. 3-11 (a), the limit for the bond length λ_{lim} related to the EL model is highlighted by a green line.

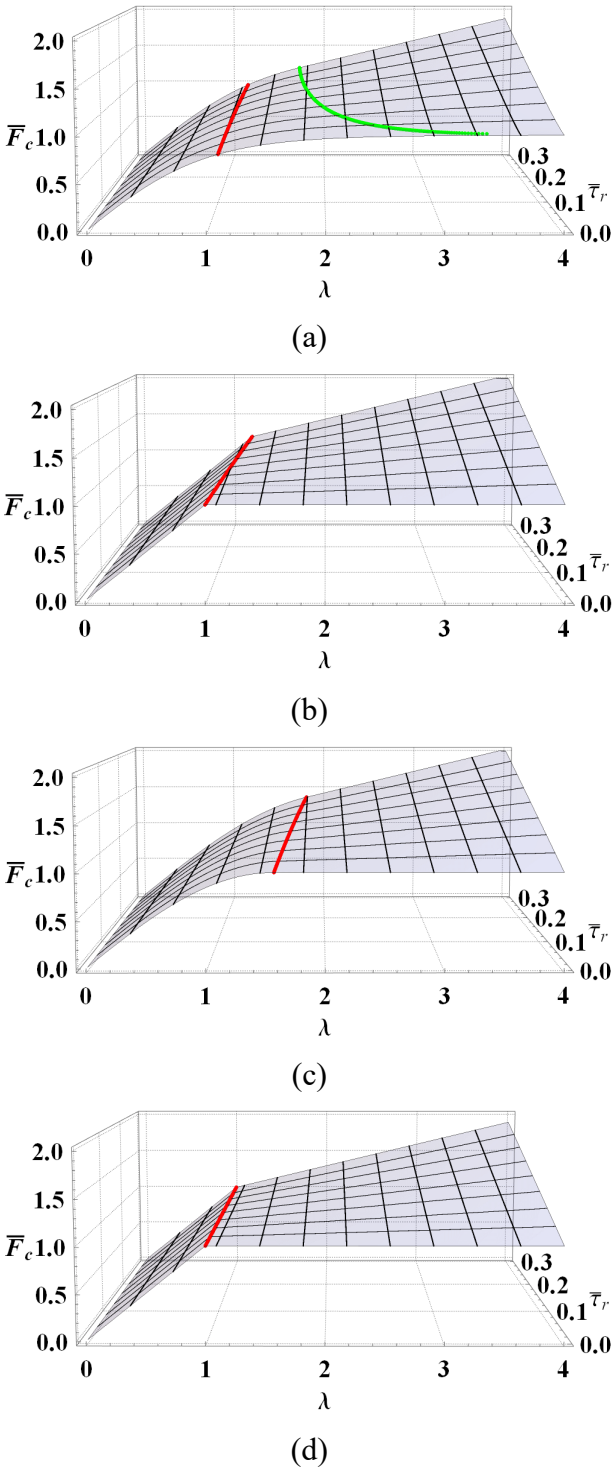

Fig. 3-11. Comparison of maximum debonding load against bond length and residual strength as per EL (a), DM (b), RL (c), RF (d). Effective bond lengths are indicated. For the EL model, $\beta = 0.8$, and the limit bond length is also emphasized.

In the scenario of $\bar{\tau}_r = 0$ and long bond lengths, the DM, RL, and RF models predict a normalized maximum debonding load of $\bar{F}_c = 1$. On the other hand, the EL model demonstrates an asymptotic behavior that approaches unity. Moreover, in the context of the EL model, the critical bond length parameter λ_{lim}, which distinguishes between short and long bond solutions, tends toward infinity by diminishing the residual strength. As a result, λ_{lim} is not an effective metric for estimating the effective bond length for the EL model.

In summary, Fig. 3-11 illustrates that each graph can be segmented into two distinct regions by λ_{eff}. In the region to the left of λ_{eff}, an increase in bond length results in a significant rise in the load. Conversely, in the region to the right, the increment in load with respect to bond length is relatively modest. Additionally, the influence of residual strength on the maximum debonding load is stronger for long bond lengths compared to short ones.

To perform a comparative analysis, estimations of the maximum debonding load using different models are depicted in Fig. 3-12(a) for a constant value of residual strength $\bar{\tau}_r = 0.15$. As observed, all models yield similar predictions for the maximum debonding load in the case of very short bond lengths. For long bond lengths, DM and RL provide nearly identical estimates, RF offers intermediate values, while EL yields the lowest estimations for the maximum debonding load. It should also be noted that the slope of the tangent at the origin is proportional to the undamaged shear strength τ_c (represented as 1 in the dimensionless plot), whereas the slope of the linear segment during the frictional stage is proportional to τ_r (represented as $\bar{\tau}_r$ in the dimensionless plot). It can be argued that when there is no available information regarding the shape of the bond-slip law, the EL model is recommended for use, as it provides the most conservative estimates for the maximum debonding load. Utilizing other models may result in an overestimation of this parameter.

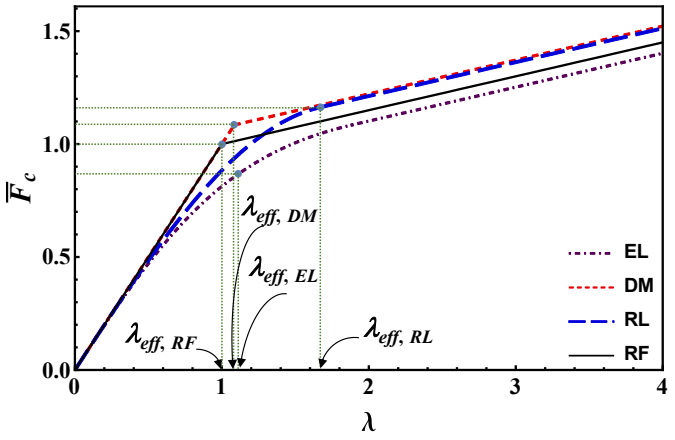

(a)

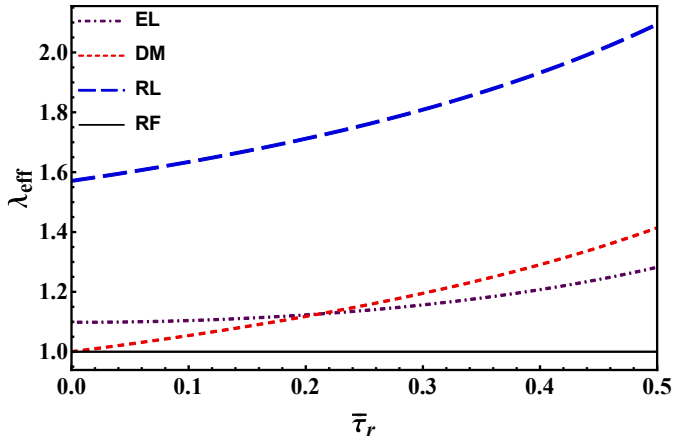

(b)

Fig. 3-12. (a) Comparison of maximum debonding load as a function of bond length for EL, DM, RM, and RF models with a constant residual strength of $\bar{\tau}_r = 0.15$. (b) effective bond length plotted against residual strength. In the case of the EL model, $\beta = 0.8$.

3.3.2 Effective bond length

For the sake of clarity, it is good to recall expressions for the effective bond length in their dimensional forms, according to the EL, DM, RL and RF models, respectively:

$$l_{eff,\,EL} = \frac{\operatorname{arctanh}\left[\beta\sqrt{1-\tau_r/\tau_c}\right]}{1-\tau_r/\tau_c}\,\frac{1}{\tau_c}\sqrt{\frac{2\mathcal{G}_c E_p A_p}{(1+\rho)L_p}} \tag{3-47}$$

$$l_{eff,DM} = \frac{1}{\sqrt{1-\tau_r/\tau_c}} \frac{1}{\tau_c} \sqrt{\frac{2 G_c E_p A_p}{(1+\rho) L_p}} \tag{3-48}$$

$$l_{eff,RL} = \frac{\arccos[\tau_r/\tau_c]}{1-\tau_r/\tau_c} \frac{1}{\tau_c} \sqrt{\frac{2 G_c E_p A_p}{(1+\rho) L_p}} \tag{3-49}$$

$$l_{eff,RF} = l_{ch} = \frac{1}{\tau_c} \sqrt{\frac{2 G_c E_p A_p}{(1+\rho) L_p}} \tag{3-50}$$

As mentioned before, according to Eq. (3-47), the effective bond length for the EL model depends on the parameter β. Given that arctanh[1] is infinite, selecting high β values close to one can lead to unrealistic estimates of effective bond lengths. To obtain reasonable estimates for effective bond lengths across any value of residual strength, we opted for β = 80%, as illustrated in Fig. 3-12(b).

It should be emphasized that Eq. (3-49) serves as an extended version of the formula mentioned in the Italian Standards CNR-DT 200 R1/2013 [125], considering the residual strength and the mechanical properties of reinforcement. Specifically, by tending τ_r and ρ to zero, and incorporating the plate thickness t_p = A_p / L_p, one can revert to the effective bond length expression as defined in CNR-DT 200 R1/2013.

$$l_{eff,CNR\text{-}DT} = \frac{\pi}{\tau_c} \sqrt{\frac{G_c E_p t_p}{2}} \tag{3-51}$$

In Fig. 3-12(a), the estimated effective bond lengths, derived from Eq. (3-47) to (3-50), was illustrated for four different models. Furthermore, these estimates are presented as functions of the normalized residual strength in Fig. 3-12(b). Except for the RF, all other models indicated an increase in effective bond length with rising residual strengths, while the estimates by RF remain constant. Among the presented models, RL was the most conservative, offering the highest estimated values for effective bond length.

A concluding remark considering the effect of residual strength, which could be significantly high, particularly for FRCMs is that neglecting it leads to an underestimation of both the debonding load and the effective bond length. Consequently, when employing equations such as Eq. (3-51), the full potential of the strengthening system is not optimally utilized.

3.3.3 Debonding load vs. relative crack length

Fig. 3-13 presents the load during the debonding process for long bond lengths, using different models as described by Eqs. (3-16), (3-27), (3-34) (3-37), and (3-45). It is observed that all models, except the RF, predict a normalized load greater than one when $\alpha = 0$, indicating the presence of residual strength even at the onset of debonding. Both the DM and RF models exhibit similar trends during the debonding process: initially a linear increase in load, followed by a linear decrease. However, it is worth noting that the RF model predicts lower values in the stable debonding phase. The RL model demonstrates a linear increase in load within the stable branch, culminating in a sharp drop after reaching the maximum load. In contrast, the EL predicts the lowest maximum load, accompanied by a gradual variation in load through the debonding process.

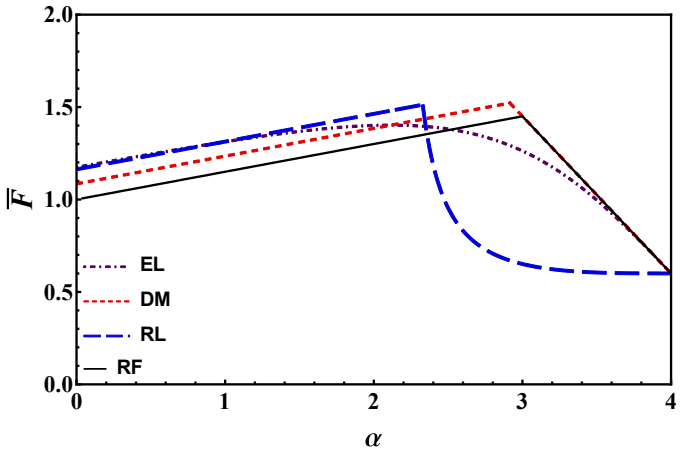

Fig. 3-13. Variation of debonding load with respect to crack length α for $\lambda = 4$ and $\bar{\tau}_r = 0.15$.

Fig. 3-13 confirms the trend observed in Fig. 3-12(a). Specifically, when arranging the models in descending order based on their estimated maximum load values, the sequence is DM, RL, RF, EL. This trend is also evident in Fig. 3-12(a) for a fixed long bond length.

3.3.4 Comparison with experimental data

To validate the models presented, experimental data for direct single lap shear tests on joints between polyparaphenylene benzobisoxazole (PBO) fiber-reinforced cementitious matrix (FRCM) and concrete were taken from existing literature [118] (the geometry is the one presented in Fig. 3-1(d)). The tests employed concrete blocks with a cross-section of 125 mm × 125 mm. Each fiber in the FRCM net featured a cross-section approximately 5 mm × 0.092 mm and had an elastic modulus of 206 GPa. These fibers were sandwiched between two layers of cementitious matrix, each with a 4 mm thickness. While the elastic modulus of the

matrix was not specified in the cited reference, it was assumed to be 30 GPa for the purpose of this study.

To evaluate the accuracy of the models in estimating the maximum debonding load, experimental results were analyzed considering three distinct bond widths – 43 mm, 60 mm, and 80 mm – as well as six different bond lengths – 100 mm, 150 mm, 200 mm, 250 mm, 330 mm, and 450 mm. Failure predominantly happened due to debonding between the PBO net and the cementitious matrix. Therefore, the area of the PBO fibers in contact with the matrix (A_p) was approximated as n×5 mm×0.092 mm and the length of the contact perimeter (L_p) as n×2×5 mm, where n represents the number of PBO longitudinal fibers. The number of longitudinal fibers n was found to be 5, 7, and 9 for reinforcement-to-substrate widths of 43 mm, 60 mm, and 80 mm, respectively.

In four specimens, all having a bond length of 330 mm, the central PBO fiber was equipped with strain gauges. Utilizing these measurements, D'Antino et al. [117,118] subsequently derived an average bond-slip law characterized by the following parameters: $\mathcal{G}_c$ = 0.481 N/mm, τ_c = 0.77 MPa and τ_r = 0.06 MPa. It is noteworthy that the Authors employed a distinct definition for fracture energy, specifically, the total area under the τ-s curve up to s_f. Consequently, their reported fracture energy corresponds to a value of 0.387 N/mm when the presented framework is considered. Based on the experimental data and utilizing Eqs. (3-13) through (3-15), the derived values are: $\bar{\tau}_r$ = 0.078, $F_c^{\infty}/n = 819.3$ N and l_{ch} = 106.4 mm.

A comparison between experimental data and analytical predictions with respect to failure load per unit fiber as a function of bond length is presented in Fig. 3-14. In the figure, theoretical outcomes are depicted through lines, while the experimental results for bond widths of 43 mm, 60 mm, and 80 mm are represented by squares, circles, and triangles, respectively. It is noteworthy that all the models exhibit good alignment with the experimental data. The agreement between theoretical predictions and experimental observations gains additional importance when considering that the interface parameters were not specifically fitted for this comparison. Instead, they were derived from strain and displacement measurements conducted on a single geometry, specifically one with a bond length of 330 mm. This implies that by examining just one bond length, the models possess the capability to predict failure across varying bond lengths and thicknesses. This serves as a sample of the robustness of the approaches presented, in addition to the high accuracy of the experimental measurements provided in [117].

Furthermore, for bond lengths in proximity to the transition length l_{ch}, the predictions from the DM and RF models are slightly less accurate. Experimental data indicates a smooth transition between short and long bond lengths, a feature better captured by the EL and RL models. Specifically, the EL model offers superior

predictions for short bond lengths, while the RF model aligns more accurately with experimental data for long bond lengths. This observation, coupled with the model's simplicity, attests to the efficacy of the FFM approach in addressing the problem under study. Lastly, concerning data associated with varying reinforcement widths, Fig. 3-14 demonstrates that despite being one-dimensional, the models account for the width effect with reasonable accuracy.

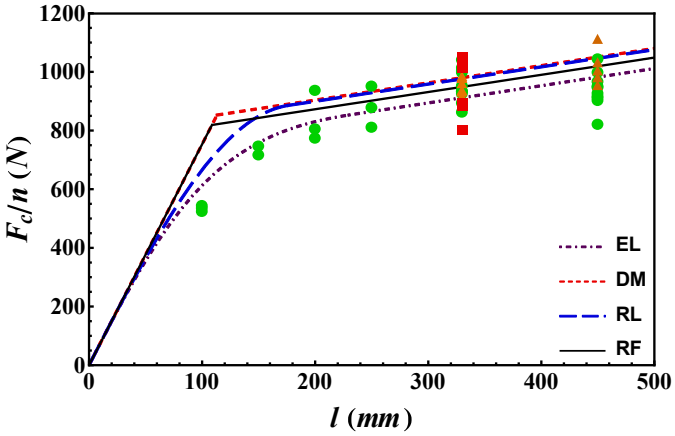

Fig. 3-14. Representation of maximum debonding load across various bond lengths and widths. The dot-dashed purple line, short-dashed red line, long-dashed blue line, and solid black line correspond to estimations obtained using the EL, DM, RL, and RF models, respectively. Experimental data sourced from [118] **are indicated by markers, the shapes of which denote different bond widths.**

Chapter 4

Extension of FFM to Assess Lifetime of Notched Structures[2]

4.1 Introduction

Stress concentrators, such as cracks, notches, or holes, are incorporated into structures for design purposes or can arise from wear and environmental exposure. These features can amplify stress, influencing the component's load-bearing capability and lifetime. Regarding the loading condition of structures, fatigue stands out as particularly prominent. Generally, deformations under fatigue conditions can be categorized into two groups: low-cycle and high-cycle fatigue. The former involves materials undergoing substantial plastic deformation within each cycle, resulting in changes to their microstructure. On the other hand, high-cycle fatigue is characterized by lower stress levels, primarily in the domain of elastic deformation. The distinction between high and low-cycle fatigue is typically determined by the number of cycles, usually set around10^3-10^4 cycles. It is crucial to note that the extension of the FFM model here is not reliable when addressing low-cycle fatigue since the modeling employs the Basquin equation.

In Chapter 2, the fundamentals of FFM within static scenarios were mentioned. Its utility was further validated when assessing the failure of structures weakened by cracks, sharp and blunt V-notches, as supported by references [66,126]. Then, the criterion was adapted to tackle the fatigue limit in scenarios involving uniaxial loadings. Several studies on fatigue limit have delved into areas like crack and notch sensitivity [21], the effects of U- and blunt V-notches [22], fatigue characteristics of welded T-joints considering residual stress [127], and the size effect of spheroidal voids and corrosive pits [128]. To support the accuracy of prediction by FFM, Shen et al. [73] and Liu et al. [74] compared its results with those obtained using the TCD approach for different notched geometries. It was found that both criteria produced similar results; however, FFM exhibits higher accuracy when

[2] Some parts of this chapter have been adapted from our work previously published as "Mirzaei, A. M., Cornetti, P., and Sapora, A., 2023, A Novel Finite Fracture Mechanics Approach to Assess the Lifetime of Notched Components, Int. J. Fatigue, p. 107659."

dealing with blunter notches, as the critical distance is influenced by the curvature radius.

Having the extension of FFM for static and fatigue limit loading conditions, in this chapter, FFM is expanded to predict the lifetime of notched components subjected to constant amplitude uniaxial loadings, following [129]. The emphasis is on the high-cycle fatigue domain, grounded in the assumption that stage II, marked by crack propagation perpendicular to the loading direction, governs the fatigue lifetime of the component. Therefore, the discussion remains limited to Mode I loading scenarios. Given the negligible size of the plastic zone in the high-cycle fatigue domain, linear elastic mechanics is utilized to extract the stress and energy release rate fields (required for FFM implementation) near the notch tip.

4.2 Extension of FFM to finite fatigue life regime

Previously, in Chapter 1, it was discussed that FFM can be utilized to evaluate the failure behaviour of notched components (Fig. 4-1) when specific material properties are given: σ_c and K_{Ic} for the static scenario according to Eq. (1-12), and $\Delta\sigma_0$ and ΔK_{th} for situations concerning the fatigue limit as outlined by Eq. (1-13). To extend the applicability of FFM for fatigue life predictions, which falls between the static and fatigue limit cases, a new set of material properties is introduced, namely σ_f and K_{If} [129]. These represent the critical cycle stress and the stress intensity factor amplitude, respectively. It is supposed that each of these properties is a function of number of cycles N, following a power law relationship [16,130].

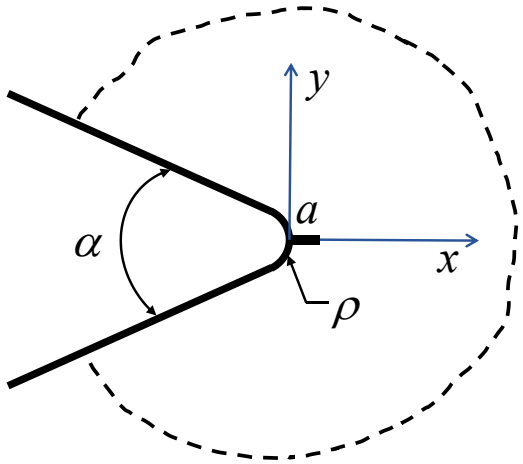

Fig. 4-1. Blunt V-notch geometry and Cartesian coordinate system located at the notch tip.

$$\sigma_f = \sigma_f(N) = a_s \; N^{-b_s} \tag{4-1}$$

$$K_{If} = K_{If}(N) = a_k \; N^{-b_k} \tag{4-2}$$

where a_s, b_s and a_k, b_k are positive functions of material properties and of loading conditions. Their variation can be calculated by fitting experimental fatigue data with 50% survival probability, obtained from both plain and cracked test samples (similar to static loading) under uniaxial loading with a constant loading ratio. It is worthwhile to mention that Eqs. (4-1) and (4-2) are in the form of Basquin equation [2]. The applicability of Eq. (4-1) is widely accepted. On the other hand, to justify Eq. (4-2), it is observed that SN data for a cracked design tend to align linearly on a log-log graph, as demonstrated in various studies [17,131–133]. It is important to note that creating sharp cracks is often a challenging task. A comprehensive discussion on calibrating a_s, b_s (from Eq. (4-1)) and a_k, b_k (from Eq. (4-2)) will be developed in the following section.

In summary, to determine the lifetime of notched components, the FFM criterion can be recast as follows:

$$\begin{cases} \dfrac{1}{l}\displaystyle\int_0^l \sigma_y(x)\,\mathrm{d}x \geq \sigma_f(N) \\ \dfrac{1}{l}\displaystyle\int_0^l K_I^2(a)\,\mathrm{d}a \geq K_{If}^2(N) \end{cases} \tag{4-3}$$

Substituting Eqs. (4-1) and (4-2) into Eq. (4-3) yields:

$$\begin{cases} \dfrac{1}{l}\displaystyle\int_0^l \sigma_y(x)\,\mathrm{d}x \geq a_s \; N^{-b_s} \\ \dfrac{1}{l}\displaystyle\int_0^l K_I^2(a)\,\mathrm{d}a \geq a_k^2 \; N^{-2b_k} \end{cases} \tag{4-4}$$

It is essential to emphasize that the Basquin equation is predominantly valid within the medium range of fatigue cycles, specifically within the finite fatigue life domain. Consequently, Eq. (4-4) is not applicable to the extreme cases such as static and fatigue limit regimes. Nonetheless, the streamlined representation of Eq. (4-4) provides a useful framework for analytical derivation. Indeed, by considering the normal stress and the SIF as products of the nominal (gross-section) stress amplitude σ_a multiplied by a geometric shape function, such that $\sigma_y(x) = \sigma_a \, g_s(x)$ and $K_I(a) = \sigma_a \, g_k(a)$, Eq. (4-4) can be recast in the subsequent form [129]:

$$\begin{cases} N \geq l^{1/b_s}\left[\dfrac{\sigma_a}{a_s}\displaystyle\int_0^l g_s(x)\,\mathrm{d}x\right]^{-1/b_s} \\ N \geq \sqrt{l^{1/b_k}\left[\left(\dfrac{\sigma_a}{a_k}\right)^2\displaystyle\int_0^l g_k^2(a)\,\mathrm{d}a\right]^{-1/b_k}} \end{cases} \tag{4-5}$$

According to Eq. (4-5), the two variables that should be determined within the FFM framework are the number of cycles to failure, N_f and the critical crack advancement, l_f. Within the proposed methodology, it is essential to recognize that N_f represents the number of cycles at which a crack of length l_f appears. Given a material and loading ratio, equating the right sides of the equations, and solving the resultant implicit equation with respect to l yields the critical length l_f for distinct stress amplitudes, σ_a. Subsequently, the determined value of l_f should be incorporated into one of the equations in Eq. (4-5) to calculate the number of cycles to failure, N_f.

It should be noted that the proposed approach can be also expressed by employing a "pointwise" stress criterion, as originally presented by Leguillon [20]:

$$\begin{cases} \sigma_y(x=l) \geq \sigma_f(N) \\ \dfrac{1}{l}\displaystyle\int_0^l K_I^2(a)\,\mathrm{d}a \geq K_{If}^2(N) \end{cases} \tag{4-6}$$

Simple analytical manipulations to Eq. (4-5) lead to:

$$\begin{cases} N \geq \left[\dfrac{\sigma_a}{a_s}g_s(l)\right]^{-1/b_s} \\ N \geq \sqrt{l^{1/b_k}\left[\left(\dfrac{\sigma_a}{a_k}\right)^2\displaystyle\int_0^l g_k^2(a)\,\mathrm{d}a\right]^{-1/b_k}} \end{cases} \tag{4-7}$$

It is crucial to clarify that the descriptor *pointwise* may not be entirely accurate, as the condition $\sigma_a > \sigma_f$ should be satisfied across the entire length l. However, since the stress field is monotonically decreasing, this condition is consistent with the first equation in Eq. (4-6).

4.3 Calibration of the model's free parameters

To determine the values of a_s and b_s, a best fitting procedure can be utilized on the experimental data from plain specimens. Such tests are typically conducted for different material and loading ratios/conditions, following specific standards. The calibration process should focus on the medium/high cycle domain, since for some materials, the linear elastic hypothesis might not hold true for $N < 10^3$-10^4, and relying on stress based methods within this span might result in significant error. While a pair of SN data points can be sufficient to calibrate a_s and b_s, the inherent variability in fatigue experimental results suggests using an expanded dataset (spanning the entire desired range), to enhance the accuracy. Next section will address this through an interpolation method rooted in linear least squares on a log-log scale.

Conversely, for the determination of a_k and b_k, experiments associated with cracked sample are required, or potentially a sharp V-notch. It is useful to recall Williams' eigenvalues remain relatively stable over the amplitude range of $0° \leq \alpha \leq 90°$ [134]. In scenarios where experimental data on sharp cracks or V-notches is missing, or when the root radius is significant (common in many notched designs), an alternative methodology can be introduced. This method involves a reverse calibration of Basquin equation (Eq. (4-2)), focusing on experimental results related to a notched specimen. It is worth noting that when data from different notch geometries are accessible, it is suggested to select the most sharp geometry for the calibration of a_k and b_k, in line with prior findings in [15,16,135]. In more detail, once applied stress and the number of cycles to failure are experimentally established, l_f can be derived from the first equation of system (4-3); subsequently, the second equation yields K_{If}. By iterating this process across several stress amplitudes (again, using an extensive dataset is recommended for comprehensive coverage), $K_{If} = K_{If}(N)$ can be specified, enabling the calibration of a_k and b_k via a straightforward interpolation method rooted in linear least squares. To encapsulate, Fig. 4-2 provides a flowchart demonstrating the steps necessary for FFM to estimate fatigue life of notched components.

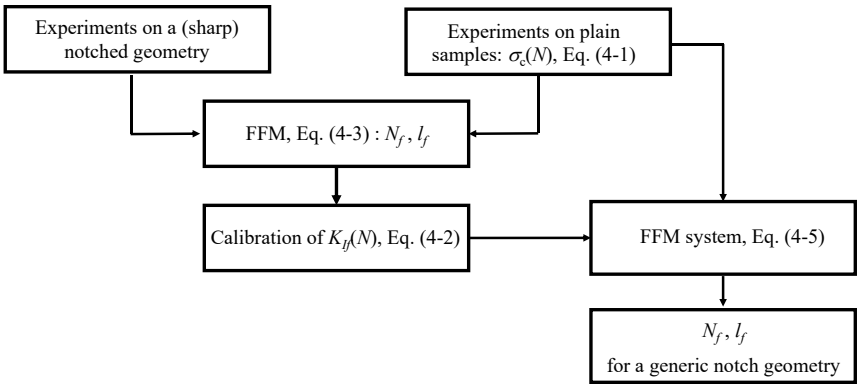

Fig. 4-2. Flowchart of the procedure for employing the FFM model for a given material and loading ratio [129]**.**

4.4 FFM validation

In this section, the FFM model is validated through experimental data, encompassing a variety of notch shapes and sizes, loading conditions, and materials [15,136,137]. To compute the shape function $g_s(x)$ associated with the normal stress σ_y (x) across all geometries, the asymptotic stress methodology presented by Mirzaei et al. [138] is utilized. The method facilitates the determination of the stress field around different notch shapes across relatively long distances from notch tip, taking into account the influence of higher order terms [139]. On the other hand, finite element analyses are undertaken for each configuration using Abaqus® software to obtain the shape function g_k (a) related to $K_I(a)$. For this purpose, the specimens are meshed using 8-node biquadratic elements. A detailed convergence analysis is subsequently executed to ensure that the numerical outcomes are not affected by variations in mesh size.

4.4.1 Different notch shapes

The validation process for the FFM model begins by utilizing experimental data presented in [15], which are related to a plain sample as well as single edge notched plates made of EN3B steel. The notched plates encompass the following configurations: a V-notch characterized by an opening angle $\alpha = 60°$ and a notch tip radius $\rho = 0.12$ mm; a U-notch ($\alpha = 0°$) with $\rho = 1.5$ mm; a central circular hole with two distinct radii, $\rho = 1.75$ and 4 mm. Testing was carried out under tension-compression loading conditions (with a loading ratio $R = -1$), and the failure cycle number N_f was identified as 50% reduction in initial stiffness. Further specifics regarding this process are elaborated in [15]. An optimal fitting method applied to the experimental data for plain specimens resulted in $\sigma_f = 935\ N^{-0.107}$ MPa, following Eq. (4-1). Conversely, when taking into account all data related to the V-notch geometry (as it is the sharpest one) to calibrate a_k and b_k in accordance with

Eq. (4-2), the findings are as follows: K_{If} = 1530 $N^{-0.381}$ MPa√m for average FFM (Eq. (4-3)), and K_{If} = 504 $N^{-0.300}$ MPa√m for the pointwise version (Eq. (4-6)).

In order to evaluate the performance of FFM, Fig. 4-3a plots the fatigue life predictions utilizing the FFM average version (Eq. (4-5)) against the related experimental data. One the other hand, Fig. 4-3b refers to the pointwise version, Eq. (4-7). Within Fig. 4-3, the horizontal axis shows the predicted lifetime, while the vertical axis represents the experimental one. Consequently, the region above the solid black line refers conservative estimations.

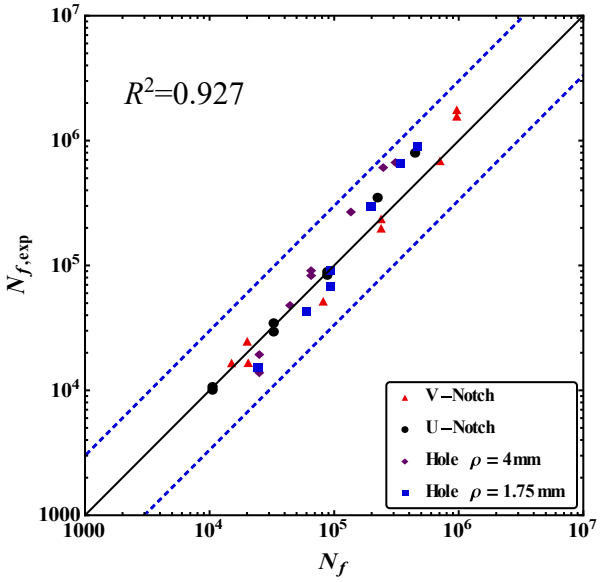

(a)

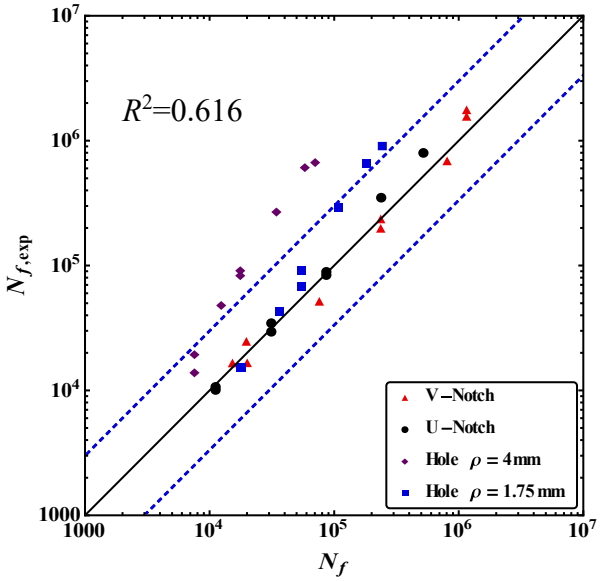

(b)

Fig. 4-3. Comparison of failure cycle counts for various notched EN3B steel samples ($R = -1$): experimental results [15] versus FFM estimates using both averaged (a) and pointwise (b) approaches. Dotted lines indicate 1/3 and 3 scatter bands.

Considering Fig. 4-3, the predictions of fatigue life by FFM across different geometries appear promising, particularly when the range of fatigue lives spans from 10^4 to 10^6 cycles. All predictions stemming from the average stress FFM

formulation, as represented by Eq. (4-5), fall within the scatter band of 1/3 and 3. However, results obtained from the pointwise FFM equation, Eq. (4-7), show slightly lower accuracy, tend to fall in the conservative range. To further evaluate the accuracy of the model, the R-squared error (often shown as R^2 or the coefficient of determination) is utilized, resulting in 0.702 and 0.649 for the averaged and pointwise FFM, respectively. Given these results, only the averaged FFM approach expressed by Eq. (4-3) will be considered hereafter.

To illustrate the predictions for each notch geometry in more detail, Fig. 4-4, showcases the amplitude of the nominal stress (gross-section) alongside its corresponding number of cycles to failure (SN diagram).

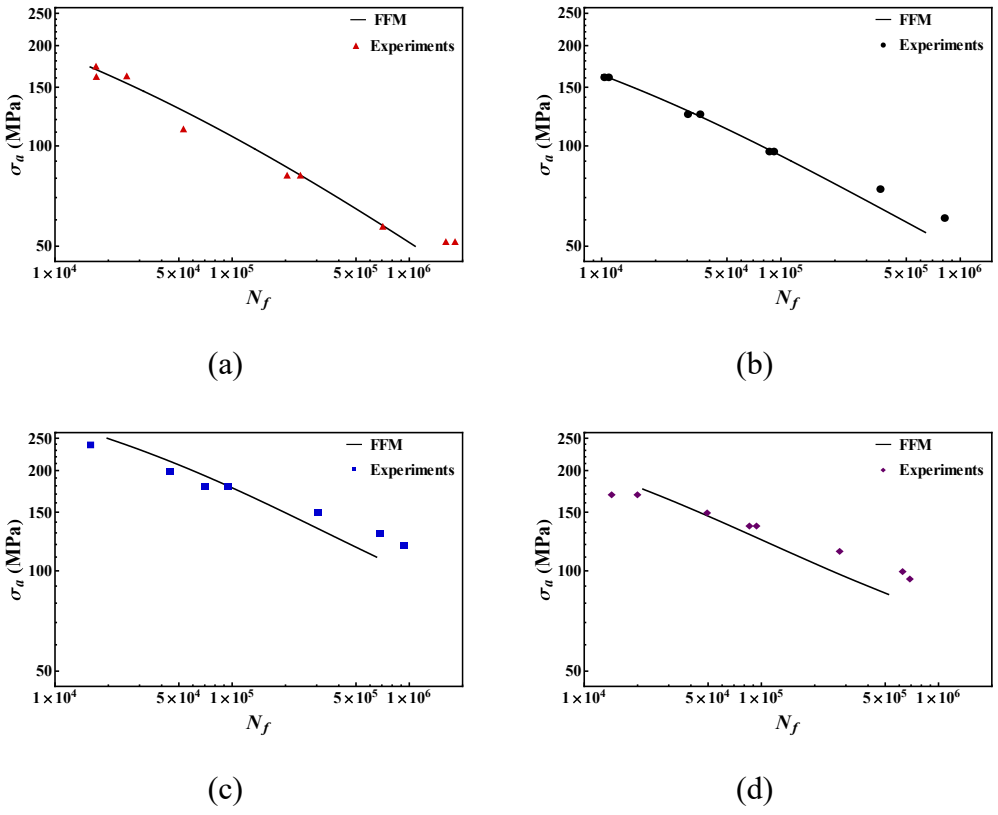

Fig. 4-4. Comparison of the predictions by average FFM (Eq. (4-7)) with experimental data: nominal (gross-section) stress amplitude vs. number of cycles to failure for different notched EN3B steel samples ($R = -1$), a) V-notch, b) U-notch, c) Hole ρ=1.75 mm, d) Hole ρ = 4 mm.

Upon examination of this experimental dataset, the model demonstrates promising accuracy for V- and U-notches. However, when applied to holed configurations, it exhibits a tendency to be slightly unconservative for lower cycle intervals.

Before moving forward, it is advisable to deepen the understanding of the FFM system, (Fig. 4-5). This illustration is based on an arbitrary example of a specimen weakened by a circular hole with a notch radius of 4 mm under σ_a =150 MPa. Fig. 4-5 shows that the stress condition is monolithically increasing, while the energy condition is monolithically decreasing, and the intersection point shows the outputs of the FFM system, l_f = 3.54 mm and N_f = 44478 cycles.

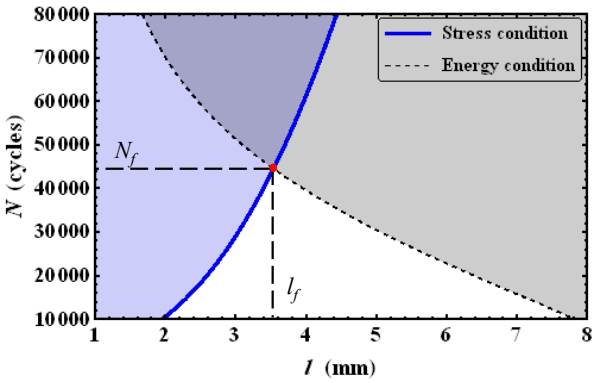

Fig. 4-5. A graphical representation of the FFM system for an arbitrary case of holed sample with ρ= 4 mm and σ_a =150 MPa.

After analyzing the performance of the model, it is useful to illustrate the other outcome of the FFM system, the critical crack advancement l_f. For this purpose, the variation of l_f as a function of number of cycles to failure is illustrated in Fig. 4-6 for the V-notched configuration. A linear regression approximation for l_f results in the relationship: l_f =245 $N^{-0.406}$.

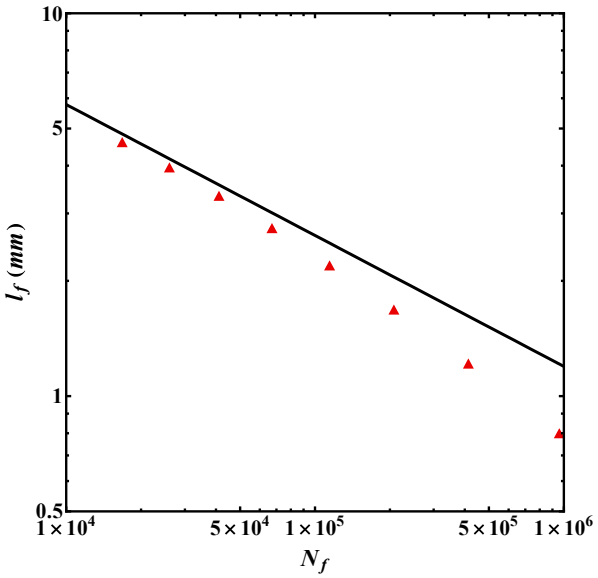

Fig. 4-6. Crack progression (critical distance) l_f plotted against cycle count for the V-notched design [15]: Representations from FFM (markers) compared with TCD predictions (continuous line).

On the other hand, the critical distance by TCD is represented by $l_{f,LM} = 134.8\ N^{-0.342}$ (as referenced in Eq. (17) of [15]), is shown. As anticipated, the crack advancement determined from both approaches exhibits a similarity, especially in the realm of lower cycle domains. Again, it is essential to emphasize that $l_{f,LM}$ is assumed to vary based on a power law equation dependent on N, thereby serving as an input parameter for the model. In contrast, within the framework of the FFM methodology presented, l_f is an outcome generated by the system, as outlined in Eq. (4-4).

4.4.2 Different (uniaxial) loading conditions

To validate the applicability of the FFM model for predicting fatigue life across various notch geometries under different uniaxial loading conditions, an additional set of experimental data concerning EN3B steel is now examined [15]. This dataset encompasses six distinct notched samples that underwent tension-tension testing with a loading ratio $R = 0.1$. Both tensile and bending loading conditions were considered. The specimens under tensile loading maintain identical geometrical properties as those described in the previous subsection. In contrast, the bending specimens, which were approximately four times thicker than tensile ones, were comprised of an edge V-notched plate weakened by an opening angle $\alpha = 45°$ and a radius $\rho = 0.383$ mm, as well as an edge U-notched plate with an angle $\alpha = 0°$ and a radius $\rho = 5$ mm.

From an examination of this dataset, we get: $\sigma_f = 1920\ N^{-0.178}$ MPa according to Eq. (4-1). Furthermore, by calibrating the parameters a_k and b_k utilizing the

tensile V-notched configuration (specifically, the sharpest design) as outlined in Eq. (4-2), $K_{If} = 436\ N^{-0.312}$ MPa√m is obtained.

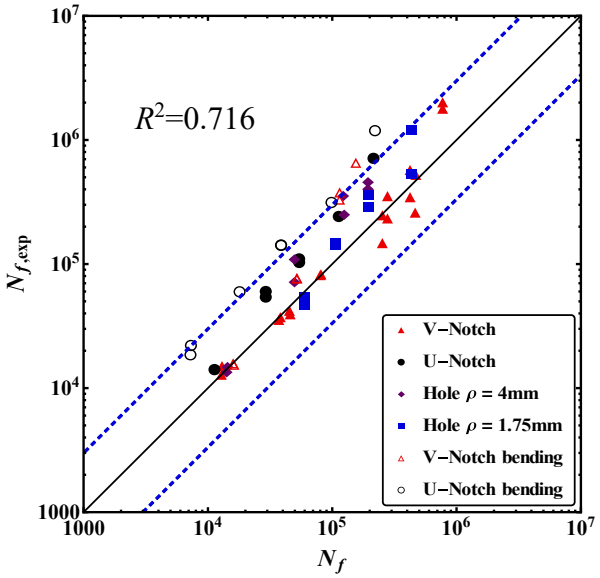

Fig. 4-7. Number of cycles to failure for various notched geometries made of EN3B steel (R = 0.1): experimental data [15] vs. predictions by FFM. The dashed lines represent 1/3 and 3 scatter bands.

Fig. 4-7 shows that the theoretical predictions closely match the experimental data. Notably, the results tend to be more conservative for samples subjected to bending. This observation can be understood by recognizing that SN data for unnotched specimens vary when shifting from tensile to bending loading conditions, as highlighted in [140,141]. Specifically, within the cycle range of 10^4 and 10^6, plain specimens under bending display a longer fatigue life, with a difference ranging from 18 percent to 10 percent, based on the results presented in [15]. To improve prediction accuracy, it might be beneficial to determine the strength parameters (specifically, calibrating a_s and b_s) by focusing on data related to bending loading conditions. Moreover, the significant difference in thickness (more than four times) between the sample sets, might affect the model's accuracy: such a variance might arise from neglecting 3D effects, as underscored in [142–144].

4.4.3 Size effect in fatigue

The study of size effects on failure in solid mechanics has been a crucial topic for researchers, given its significance in the engineering design of structures moving from small to large scales, and vice versa. To evaluate the FFM's ability in capturing size effect within fatigue life estimations, data related to plates with circular holes of varying radii (ρ = 0.12, 0.25, 0.5, 1.5 mm) is examined [137]. Tests were conducted under tension-compression loading conditions, with a loading ratio

of $R = -1$. The recorded fatigue lives range from 10^4 to 10^8 cycles, making this dataset ideal for assessing the model's performance over a broad cycle range. The material used was a high-strength aluminum alloy, designated as Al 2024-T351. From the analysis, $\sigma_f = 1380\ N^{-0.146}$ MPa is determined based on Eq. (4-1). By utilizing all the data corresponding to the hole with $\rho = 1.5$ mm for calibration, a value of $K_{If} = 64.7\ N^{-0.205}$ MPa√m is inferred. Alternatively, if the smallest hole is selected as the reference (a possible option in situations without a sharp geometry), the resultant value would be $K_{If} = 26.6\ N^{-0.170}$ MPa√m, leading to a minor shift in predictions.

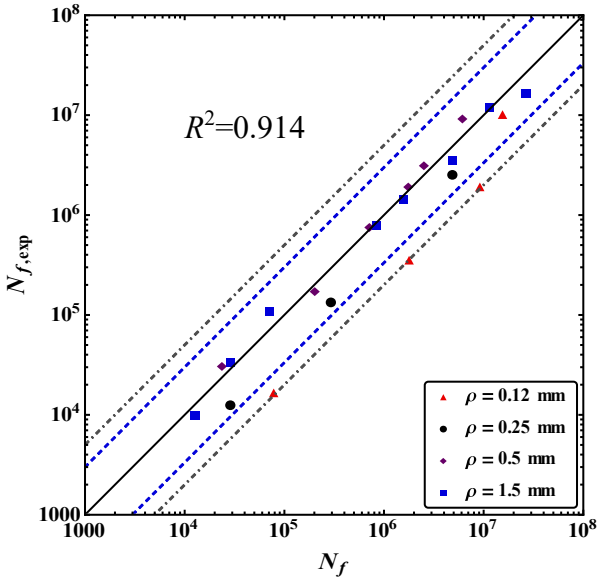

Fig. 4-8. Number of cycles to failure for various radii of holes in samples made of Al 2024-T351 ($R = -1$): experimental data [137] **vs. predictions by FFM. The dashed blue lines represent the scatter bands of 1/3 and 3, whereas the dotted-dashed gray lines illustrate the scatter bands of 1/5 and 5.**

From Fig. 4-8, it is evident that FFM's predictions align fairly well with the experimental data. The model's estimations stay within the scatter bands marked by life factors of 1/3 and 3 for hole sizes of $\rho = 0.5$ and 0.25 mm, representing size reductions by factors of 3 and 6, respectively. On the other hand, for the smallest considered hole, characterized by $\rho = 0.12$ mm, which is 12.5 times smaller than the reference $\rho = 1.5$ mm, the fatigue life predictions reach scatter bands marked by life factors of 1/5 and 5. It is essential to highlight that while some studies have achieved slightly higher accuracy in their predictions for this specific dataset [75,76], they required the calibration of additional parameters, leading to a more complex model.

Since the results by the proposed model can be obtained quite fast, a parametric analysis illustrating the impact of hole radius on the lifetime of notched samples is presented in Fig. 4-9.

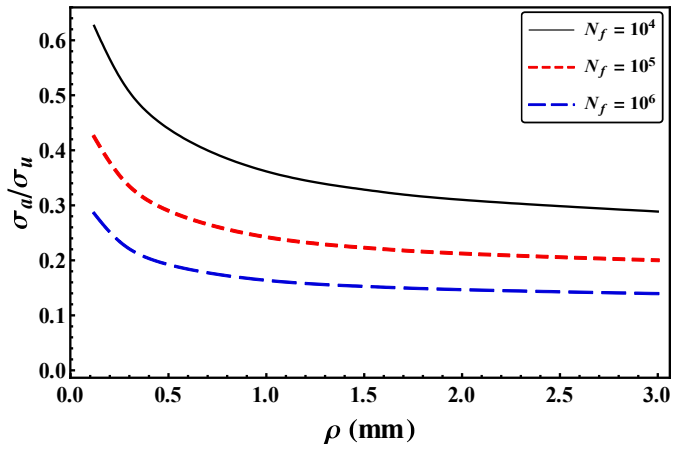

(a)

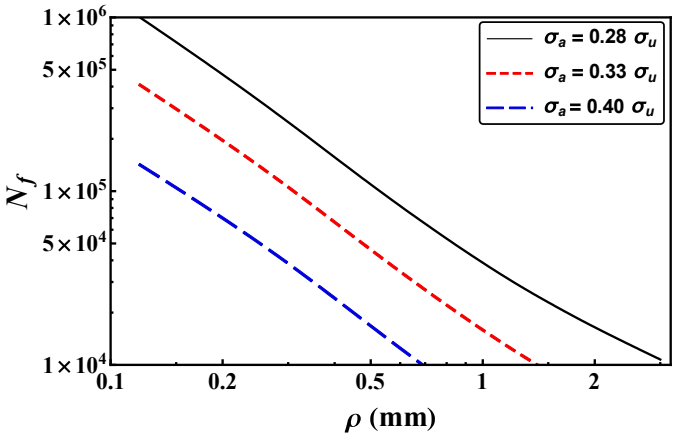

(b)

Fig. 4-9. (a) Influence of hole size on the nominal stress amplitude maintaining a consistent fatigue lifetime. (b) Variation in fatigue life due to hole radius under a steady stress, showcased in a logarithmic scale. Data pertains to Al 2024-T351 specimens [137] **under tension-compression load scenarios ($R = -1$).**

Fig. 4-9a reveals a diminishing impact of the notch radius with an increase in fatigue life. In contrast, Fig. 4-9b demonstrates an amplified notch effect for lower applied stress conditions, typical of high-cycle fatigue scenarios.

4.4.4 Additively manufactured samples

To further validate the model, attention is directed towards a non-metallic material, specifically polylactide (PLA) [136]. The tested specimens were double-edge notched plates, featuring V-notches characterized by $\alpha = 35°$ and $\rho = 0.383$ mm, as well as U-notches with $\rho = 1$ mm. These specimens had widths of 12.5 mm and net widths of 3 mm. Tests were carried out under zero-tension loading

conditions ($R = 0$). The samples were fabricated using Fused Deposition Modeling technology with three distinct manufacturing angles: $\theta_p = 0°$, 30°, and 45°. Here, θ_p represents the angle between the specimen's longitudinal axis and the primary manufacturing direction. Stress-strain curves confirmed the suitability of adopting a linear-elastic model. Furthermore, the material was assumed to exhibit homogeneous and isotropic behavior, consistent with the comprehensive assessment by Ezeh and Susmel [145]. Considering the unnotched specimen, σ_f is determined to be 47.8 $N^{-0.161}$ MPa, while the data associated with the sharpest notch geometry lead to $K_{If} = 25.9\ N^{-0.195}$ MPa$\sqrt{m}$.

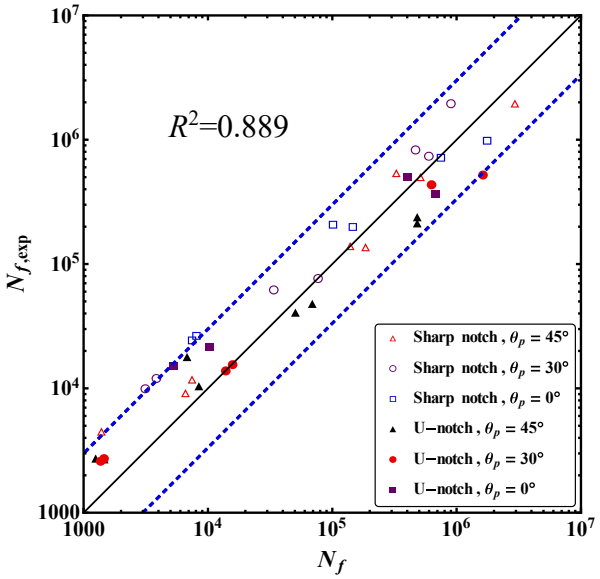

Fig. 4-10. Number of cycles to failure for various notch geometries and manufacturing angles in samples made of PLA ($R = -1$): experimental data [136] **vs. predictions by FFM. The dashed blue lines represent the scatter bands of 1/3 and 3.**

Considering the inherent simplifications, FFM effectively predicts the fatigue lives of additively manufactured specimens across various manufacturing angles, falling within the 1/3 and 3 life factor ranges, as shown in Fig. 4-10. Moreover, this dataset highlights a distinctive attribute of the coupled approach: the crack advancement is not solely function of material properties but also of geometrical factors. In practice, the averaged version of TCD does not apply in this context, as the critical distance exceeds the geometry's net width [136]. This characteristic was previously manifested in static failure scenarios for both uncracked and cracked specimens [18,128].

Subsequently, focus is shifted to another dataset related to materials produced through additive processes, specifically Inconel 718 [146]. The specimens were double-edged notched plates, which were produced using selective laser melting with a manufacturing angle θ_p set at 0°. Samples were tested under zero-tension

loading conditions (R = 0). The notch geometries include a V-notch with α = 90° and two distinct radii, ρ = 0.1 and 1 mm, in addition to a semi-circular notch with ρ = 5 mm. Note that consistent with previous assumptions, the material behavior is again considered homogeneous and isotropic. Based on results derived from the plain geometry and the sharpest V-notch (ρ = 0.1 mm), input parameters are deduced as $\sigma_f = 13000\ N^{-0.272}$ MPa and $K_{If} = 555\ N^{-0.319}$ MPa√m.

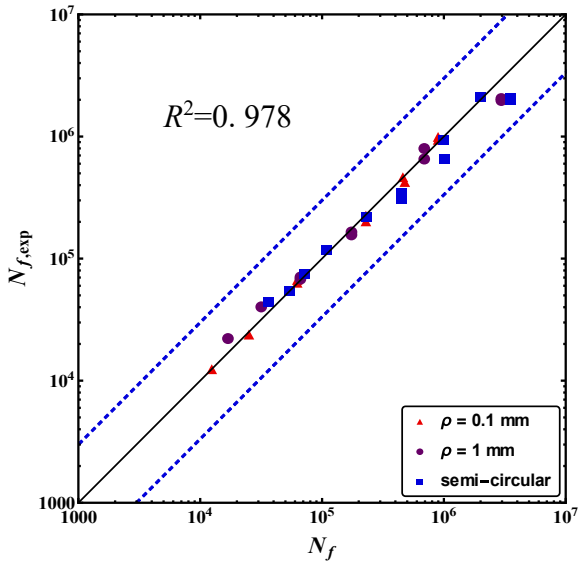

(a)

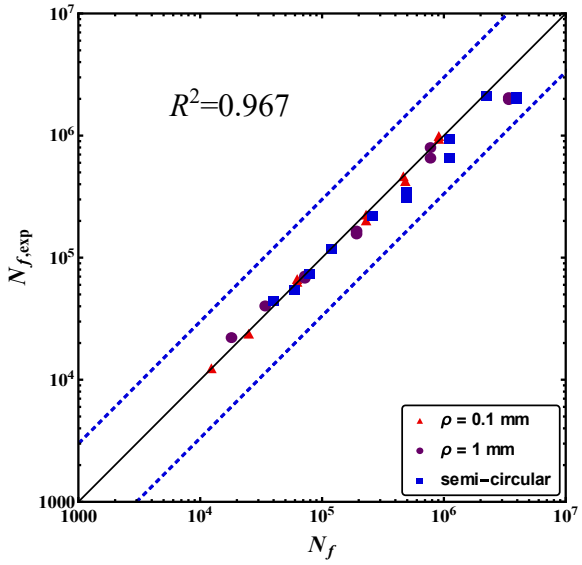

(b)

Fig. 4-11. Number of cycles to failure for various notched samples made of Inconel 718 (R = 0): experimental data [146] **vs. predictions by a) FFM, and b) TCD. The dashed blue lines represent the scatter bands of 1/3 and 3.**

Fig. 4-11a displays a strong correlation between FFM predictions, Eq. (4-5), and experimental data. For this dataset, the TCD in its averaged version [15] is also implemented, and the corresponding results are presented in Fig. 4-11b. Interestingly, the two approaches provide close predictions for this specific dataset.

Chapter 5

Extension of FFM for Lifetime Analysis of Laminates[3]

5.1 Introduction

Fiber-reinforced polymeric laminated composites have become viable substitutes for conventional materials in several engineering applications, owing to their exceptional mechanical performance and the capacity for tailoring specific material characteristics [147–150]. Yet, the structural integrity of such composite laminates can be markedly compromised by the presence of geometric discontinuities, such as cracks or notches. Considering the presence of notches in engineering structures [138,151–153], coupled with the predominance of fatigue as a primary failure mechanism [154,155], an in-depth comprehension of the fatigue behavior of notched composite laminates is essential for assuring the structural reliability and safety [156–159].

The origins of investigations into the notch failure behavior of composite materials, utilizing the coupling of linear elastic mechanics with a material length scale, date back to the pioneering work of Whitney and Nuismer [160]. Accordingly, failure happens when an effective stress at/along a critical distance from the notch tip reaches the ultimate strength. The critical distance was empirically ascertained, through a theoretical dependence on fracture toughness, utilizing a fitting procedure that accounted for the influence of both sharp notches and circular holes. This model has been a foundation for numerous studies probing the failure of notched components in both static [148,161–166] and fatigue [167] regimes. The work by Whitney and Nuismer [160] essentially laid the groundwork for the TCD, that was formalized nearly three decades later by Taylor [53]. Taylor's significant contribution [168] lays in articulating the critical distance as a function of the material properties, specifically through the squared ratio of tensile strength to fracture toughness. As a material property, this length serves as an intrinsic model

[3] Some parts of this chapter have been adapted from our work previously published as "Mirzaei, A. M., Mirzaei, A. H., Shokrieh, M. M., Sapora, A., and Cornetti, P., 2024, Fatigue Life Assessment of Notched Laminated Composites: Experiments and Modelling by Finite Fracture Mechanics, Compos. Sci. Technol., 246, p. 110376."

input. Under monotonic loading, TCD has proven to be an effective tool in estimating the notch effect in long-fiber composites [169] and short glass fiber reinforced polyamide 6 (SGFR-PA6) [170,171]. However, its application to the prediction of fatigue lifetime in notched composite laminates remains an unexplored problem.

As mentioned in Chapter 2, to eliminate the limitation of neglecting geometrical properties in critical distance, works by Leguillon [20] and Cornetti et al. [18] introduced FFM. Specifically, in the context of composite materials under monotonic loading, Camanho et al. [85] employed FFM to study the failure of open-holed composite laminates, thereby demonstrating its proficiency in accurately aligning with experimental data.

The principal objective of the present study is the extension and validation of the FFM approach for evaluating the fatigue life of notched composite laminates, based on the FFM extension to finite fatigue life derived from homogeneous materials [129], which was presented in the previous chapter. The present approach has been recently published in [172].

5.2 Linear elastic analysis of laminated composites

As mentioned in the previous chapter, the determination of fatigue life in notched structures requires an understanding of both the stress distribution and energy release rate within the components.

Let us now consider a composite laminate of width W, weakened either by a central circular hole of radius ρ (Fig. 5-1a) or by a crack of length $2a$ perpendicular to the loading direction (Fig. 5-1b). This laminate is subjected to a cyclic uniaxial tensile remote stress with an amplitude σ_a.

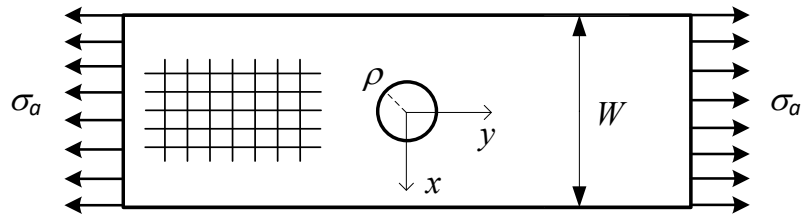

(a)

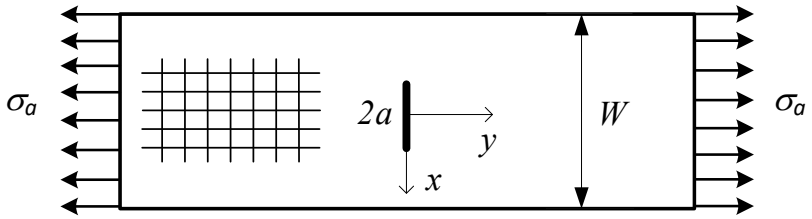

(b)

Fig. 5-1. Schematic view of a sample with: (a) a circular hole and (b) a crack, under cyclic remote uniaxial loading conditions.

In the current study, it is assumed the failure mode of the composite laminate is based on the fiber behavior, either as a brittle failure characterized by fiber fracture with minimal sub-critical damage or through a process involving fiber pull-out, which is indicative of significant subcritical damage [151,173]. Given this understanding of the failure behaviour, it is reasonable to assume that failure initiation and propagation occur along the *x*-axis. Consequently, the analysis will be oriented toward an investigation of mode I fracture, which is validated with the observed failure characteristics of the laminated composites.

5.2.1 Stress field ahead of a circular hole

Konish and Whitney [174] introduced an analytical expression to articulate the distribution of normal stress perpendicular to the loading direction (i.e., $y = 0$) in the region ahead of a circular hole within an infinite orthotropic plate. The solution accounts for the finite width of the specimens by implementing a correction factor, R_K, allowing the stress field to be analytically approximated for $x \geq \rho$:

$$\sigma_y(x) = \sigma_a \frac{R_k}{2}\left\{2+\left(\frac{\rho}{x}\right)^2+3\left(\frac{\rho}{x}\right)^4-\left(K_T^{\infty}-3\right)\left[5\left(\frac{\rho}{x}\right)^6-7\left(\frac{\rho}{x}\right)^8\right]\right\} = \sigma_a\, f_s(x) \tag{5-1}$$

where

$$K_T^{\infty} = \frac{\sigma_y(\rho)}{\sigma_a} = 1 + \sqrt{\frac{2}{A_{22}}\left(\sqrt{A_{11}\,A_{22}} - A_{12} + \frac{A_{11}\,A_{22} - A_{12}^2}{2A_{66}}\right)} \tag{5-2}$$

$$R_K = \frac{K_T}{K_T^{\infty}} = \left\{\frac{3(1-2\rho/W)}{2+(1-2\rho/W)^3} + \frac{1}{2}\left(\frac{2\rho}{W}M\right)^6\left(K_T^{\infty}-3\right)\left[1-\left(\frac{2\rho}{W}M\right)^2\right]\right\}^{-1} \tag{5-3}$$

$$M = \sqrt{\frac{\sqrt{1-8\left[\frac{3(1-2\rho/W)}{2+(1-2\rho/W)^3}-1\right]}-1}{2(2\rho/W)^2}} \tag{5-4}$$

Here, K_T^{∞} and K_T represent the stress concentration factor at the opening edge for an infinite-width and a finite-width laminate, respectively. The components of the in-plane stiffness matrix of the laminate, A_{ij}, can be ascertained based on the properties is presented in Table 5-1.

5.2.2 Stress intensity factor for holed samples

In a specimen similar to the one depicted in Fig. 5-1a, failure is observed to initiate and propagate through two symmetric cracks along the x-axis, based on experimental findings [175]. It is noteworthy that, according to both references [85,176] and comparison with numerical analyses, the influence of anisotropy on the SIF is considered to be marginal and can be disregarded for the configuration under investigation.

Additionally, the finite width of the specimen must be taken into consideration when approximating the SIF. As described in literature [177,178], the SIF at the tip of crack with length a originated from the circular hole can be analytically represented as:

$$K_I = \sigma_a F_h F_w \sqrt{\pi a} = \sigma_a \sqrt{\pi a}\ \ f_k(a) \tag{5-5}$$

$$F_h = 1 + 0.358\frac{\rho}{a+\rho} + 1.425\left(\frac{\rho}{a+\rho}\right)^2 - 1.578\left(\frac{\rho}{a+\rho}\right)^3 + 2.156\left(\frac{\rho}{a+\rho}\right)^4 \tag{5-6}$$

$$F_w = \sqrt{\sec\left[\frac{\pi\rho}{W}\right]\sec\left[\frac{\pi(a+\rho)}{W}\right]} \tag{5-7}$$

It is important to emphasize that the accuracy of Eq. (5-5) has been confirmed to be within 2% of the results obtained through boundary-collocation methods [178]. The analyses presented in this section provide a robust basis for understanding the behavior of holed samples under various loading conditions, contributing to the broader understanding of composite laminate failure mechanisms.

5.2.3 Stress intensity factor for cracked samples

In analyzing the cracked geometry as shown in Fig. 5-1b, the material's orthotropy, represented by $Y(\xi)$, and the finite width of the plate, denoted by $F(a/W)$, must be considered. Accordingly, the SIF for a center crack with length $2a$ can be expressed based on the following mathematical relations [179]:

$$K_I = \sigma_a \sqrt{\pi a}\, Y(\xi)\, F(a/b) \tag{5-8}$$

$$Y(\xi) = 1 + 0.1(\xi - 1) - 0.016(\xi - 1)^2 + 0.002(\xi - 1)^3 \tag{5-9}$$

$$F(a/W) = [1 - 0.025(a/W)^2 + 0.06(a/W)^4]\sqrt{\sec\frac{\pi(a/W)}{2}} \tag{5-10}$$

Here, the dimensionless parameter ξ is specifically defined in terms of the engineering elastic constants of the material [179,180]:

$$\xi = \frac{(E_1 E_2)^{1/2}}{2G_{12}} - (\nu_{12}\nu_{21})^{1/2} \tag{5-11}$$

It should be noted that the error associated with the utilization of Eq. (5-8) has been quantified as being under 5%.

5.3 Fatigue failure criteria

In order to estimate the fatigue lifetime of notched laminated composites, FFM and TCD models are employed, and their results are compared. To recall, Section 1.4.1 discussed the extension of the TCD model for finite fatigue life estimation of notched specimens made of homogeneous materials, according to Susmel and Taylor's approach [15]. Moreover, Chapter 4 presented the extension of the FFM model to the finite fatigue life regime [129].

The only distinction in formulation is that, in composite materials, the ultimate tensile strength is denoted by X_c (insteat of σ_c), and thus, the critical cyclic stress for composite materials is represented as $X_f(N)$. Section 5.6.1 elaborates further on the input material properties of the models. Before proceeding, two notable distinctions regarding TCD and FFM should be highlighted:

1. According to TCD, the critical crack advancement is presumed to follow a power law function of the number of cycles to failure.
2. In scenarios of static loading, the FFM approach necessitates solving a system of two equations, indicating a more complex analysis compared to TCD. However, in the context of fatigue loading, both methodologies

entail solving nonlinear equations. Consequently, they are comparable from a computational cost perspective.

5.4 Experimental campaign

An experimental investigation is conducted on composite laminates, with two different stacking sequences. The campaign encompasses static tests to obtain the elastic properties, as well as fatigue tests on specimens with various geometrical configurations, namely plain, cracked, and notched specimens. The notched specimens are specifically created with drilled circular holes of two distinct radii [172].

5.4.1 Materials and fabrication of samples

The experimental specimens are fabricated from carbon fiber (T300-12K, 200 g/m^2) combined with a low-viscosity epoxy resin (Araldite LY 5052), and cured with Aradur 5052 Hardener at a weight fraction of 100:38. Utilizing the vacuum-assisted resin injection method, the composite laminates undergo an initial curing at 23°C for 24 hours, followed by a post-curing phase at 100°C for 4 hours, adhering to the supplier's recommendations.

Following the curing process, the composite laminate plates are sectioned into specimens using a waterjet machine. For the holed samples, central holes are reamed to the final size with a drill press at a controlled speed of 300 RPM. This specific methodology is employed to mitigate delamination at the hole perimeter – a common phenomenon with the waterjet machine, particularly for smaller diameters. To introduce cracks, a central slit measuring 12 mm in length and 2 mm in width is created in each sample using waterjet cutting. Subsequently, cracks of 1.7 mm in length are meticulously crafted on both sides of the slit using a thin razor blade, resulting in a total crack length of a = 15.4 mm. All lateral and hole surfaces are then finely polished using sandpaper.

The final stage of preparation involved equipping the specimens with quasi-isotropic glass/epoxy tabs, having $[0/90/45/-45]_s$ configuration. A schematic illustration of the fabricated notched specimens is presented in Fig. 5-2. Additionally, Table 5-1 provides a detailed presentation of the geometrical properties of the specimens both with and without stress concentration, enabling a thorough characterization and evaluation of the proposed theoretical models. Notably, the ratio of the width to hole radius for the notched specimens is consistently maintained at approximately 6.

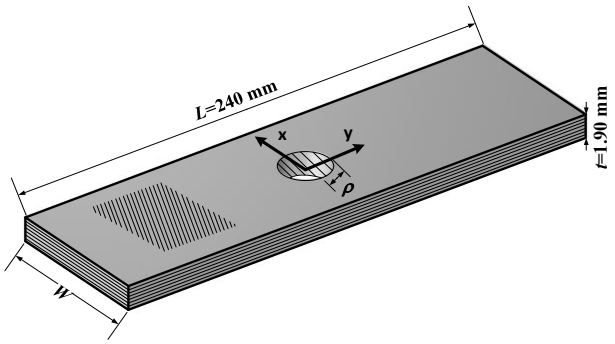

(a)

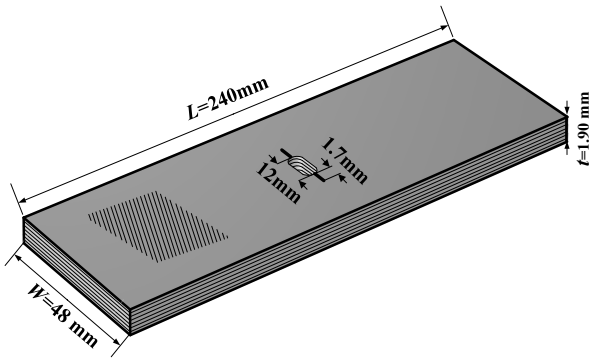

(b)

Fig. 5-2. Schematic view of the fabricated notched specimens. (a) Holed (W = 24, 36 mm and ρ = 2.1, 3.25 mm) and (b) cracked geometry.

Table 5-1. Specifications of the performed experimental tests.

	Specimen configuration	Layup	W (mm)	L (mm)	t (mm)	Aim	Type of loading	Number of tests
1	Longitudinal loading	$[0_6]_t$	15	250	1.44	Material characterization	Static	4
2	Transverse loading	$[90_{10}]_t$	25	175	2.2	Material characterization	Static	4
3	Shear loading	$[45/-45]_{4s}$	25	200	3.53	Material characterization	Static	4
4	Cross-ply, plain	$[0/90]_{2s}$	25	240	1.9	Model characterization	Fatigue	10
5	Cross-ply, cracked, a = 15.4 mm	$[0/90]_{2s}$	48	240	1.9	Model characterization	Fatigue	8
6	Cross-ply, drilled, ρ = 2.1mm	$[0/90]_{2s}$	24	240	1.9	Model validation	Fatigue	8
7	Cross-ply, drilled, ρ = 3.25mm	$[0/90]_{2s}$	36	240	1.9	Model validation	Fatigue	7
8	Cross-ply, plain	$[90/0]_{2s}$	25	240	1.9	Model characterization	Fatigue	9
9	Cross-ply, cracked, a = 15.4 mm	$[90/0]_{2s}$	48	240	1.9	Model characterization	Fatigue	7
10	Cross-ply, drilled, ρ = 2.1mm	$[90/0]_{2s}$	24	240	1.9	Model validation	Fatigue	8
11	Cross-ply, drilled, ρ = 3.25mm	$[90/0]_{2s}$	36	240	1.9	Model validation	Fatigue	11

5.4.2 Testing setup and experimental details

The comprehensive experimental campaign contains both static and fatigue testing, utilizing the Santam SAF-50 machine equipped with hydraulic grips. To eliminate the risk of self-heating and temperature increase in the specimens during fatigue tests, a controlled frequency of 5 Hz was applied [158,181]. A concerted effort is made to minimize the influence of out-of-plane stresses and the probability of delamination within the composite laminates. This is systematically achieved by establishing the stress ratio (minimum stress to maximum stress) at 0.1 and selecting low-thickness specimens for the tests [182]. Fig. 5-3 illustrates the experimental setup employed in the testing procedure.

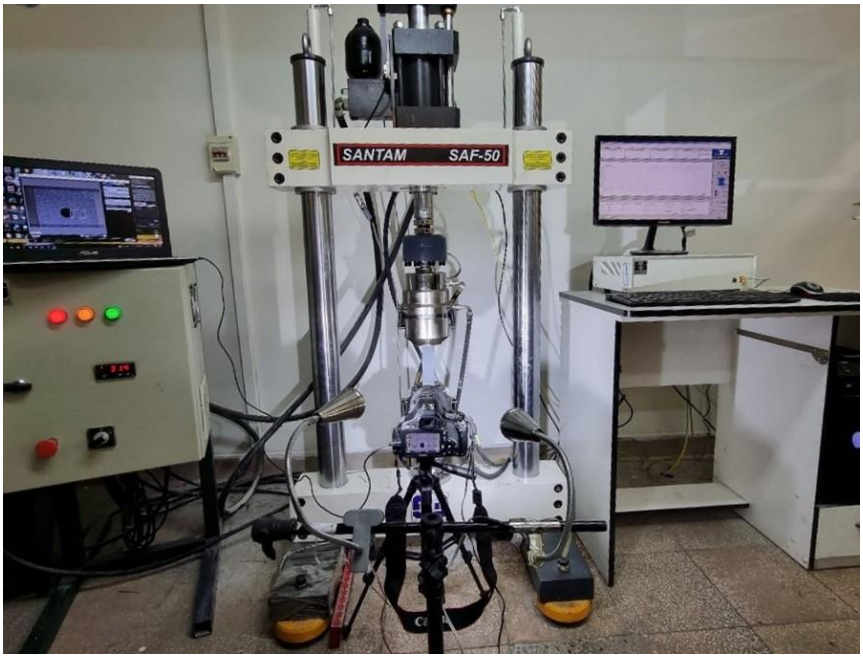

Fig. 5-3. Experimental setup employed to conduct the static and fatigue tests.

The notch sensitivity in a laminate is governed by a multifaceted interplay of factors such as size, thickness, ply orientation, notch geometry, and the composite material's intrinsic constituents [183]. Research by Harris and Morris [184], as well as by Vaidya et al. [185], has demonstrated the relationship between increased laminate thickness and strength, finding that a bigger thickness typically confines damage near the surface, thereby changing the failure mechanism to delamination. Consequently, ensuring that the failure mode in the samples aligns with either a brittle failure or a pull-out mechanism is vital for the accurate application of the models to laminated composites.

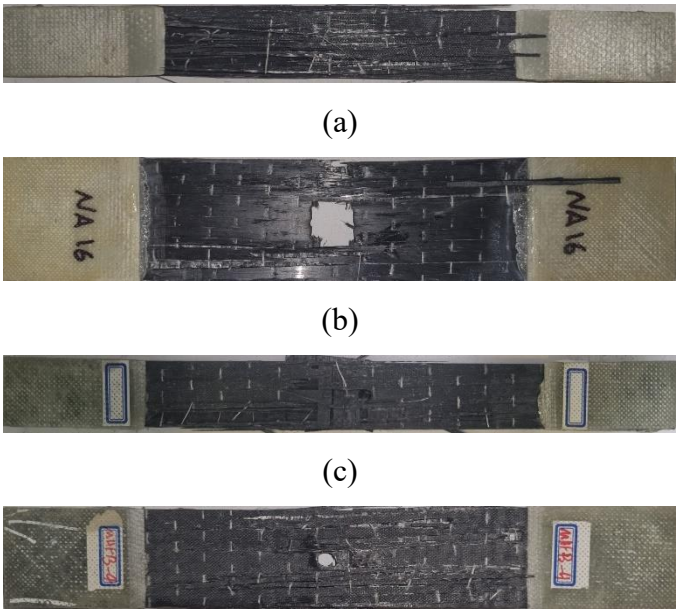

(a)

(b)

(c)

(d)

Fig. 5-4. Specimens post-fatigue failure in pull-out mode: (a) plain, (b) cracked, (c) holed with ρ = 2.1 mm, (d) holed with ρ = 3.25 mm.

5.4.3 Static tests: material characterization

The mechanical properties of the materials are determined in accordance with standardized testing protocols. The longitudinal and transverse properties, encompassing elastic moduli, ultimate tensile strength, and Poisson's ratio, are obtained using the ASTM D3039 standard [186]. In addition, in-plane shear properties are determined in line with the ASTM D3518 standard [187]. Table 5-2 displays the results of the quasi-static tests (average of four tests) conducted to obtain the material properties. It should be mentioned that the fiber-to-matrix volume fraction is accurately determined utilizing the burn-out method as suggested in the ASTM D3171 standard [188].

Table 5-2. Material properties of T300/LY5052 unidirectional composites.

Property	Symbol	Magnitude
Tensile modulus	E_1	42 GPa
Transverse modulus	E_2	8.5 GPa
In-plane shear modulus	G_{12}	6 GPa
Poisson's ratio	ν_{12}	0.31
Ultimate tensile strength	X_c	914 MPa
Transverse strength	Y_t	17 MPa
In-plane shear strength	S_{xy}	78 MPa
Ply thickness	t	0.235 mm
Fiber volume fraction	v_f	56%

The measured ply thickness for the material is equal to $t = 0.235$ mm. As shown in Fig. 5-4, the primary failure mode observed across the specimens is predominantly associated with the pull-out effect, with no instances of brittle failure noted.

5.4.4 Fatigue tests

The fatigue performance of the composite laminates is thoroughly investigated for two different layup configurations: $[90/0]_{2s}$ and $[0/90]_{2s}$, with the corresponding stress-life (SN) diagrams presented in Fig. 5-5 and Fig. 5-6, respectively. These diagrams illustrate the experimental data for both plain and cracked specimens, which are used as inputs of models. Additionally, specimens featuring holes with radii of $\rho = 2.10$ and 3.25 mm are employed for blind predictions. According to the detailed information in Table 5-1, the comprehensive fatigue evaluation consists of a total of 33 samples for the $[0/90]_{2s}$ configuration and 35 samples for the $[90/0]_{2s}$ configuration, with each individual notch geometry being represented by 7 to 11 specimens. The SN diagrams are constructed in a log-log format, showing the nominal (gross-section) stress amplitude, σ_a, in relation to the number of cycles to failure, N_f, where failure is explicitly defined as the complete detachment of the specimens. Within the experimental framework, fatigue loading amplitudes were selected to span a wide range of stress levels, facilitating a comprehensive evaluation of material behavior under varying fatigue conditions. The SN diagrams include solid black lines, representing the best-fitting curves derived from the experimental data, which correspond to a Probability of Survival (PS) of 50%. Complementing these, scatter bands are restricted by dashed red lines, symbolizing

PS values of 97.7% and 2.3%, thereby providing a statistical context to the fatigue performance of the specimens.

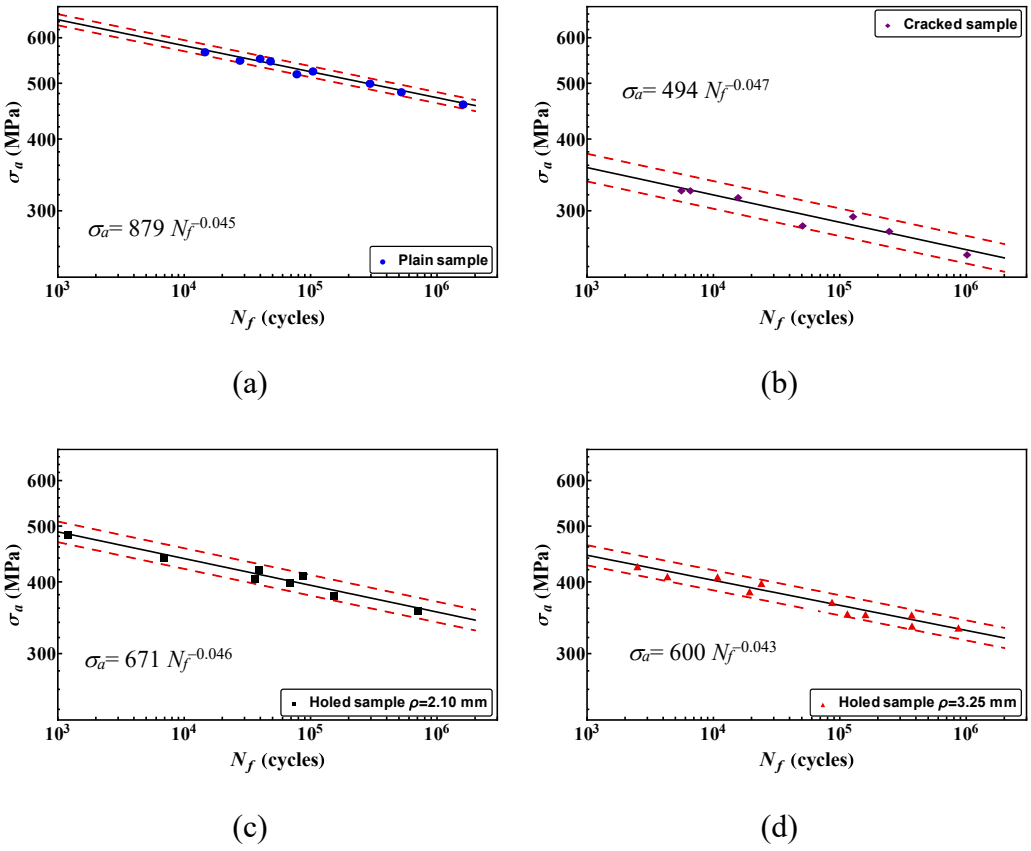

Fig. 5-5. Stress-life diagrams for $[90/0]_{2s}$ composite laminate: (a) plain sample, (b) cracked sample, (c) samples weakened by a hole with radius ρ = 2.1 mm and (d) ρ = 3.25 mm. The dashed red lines represent a PS of 97.7% and 2.3%.

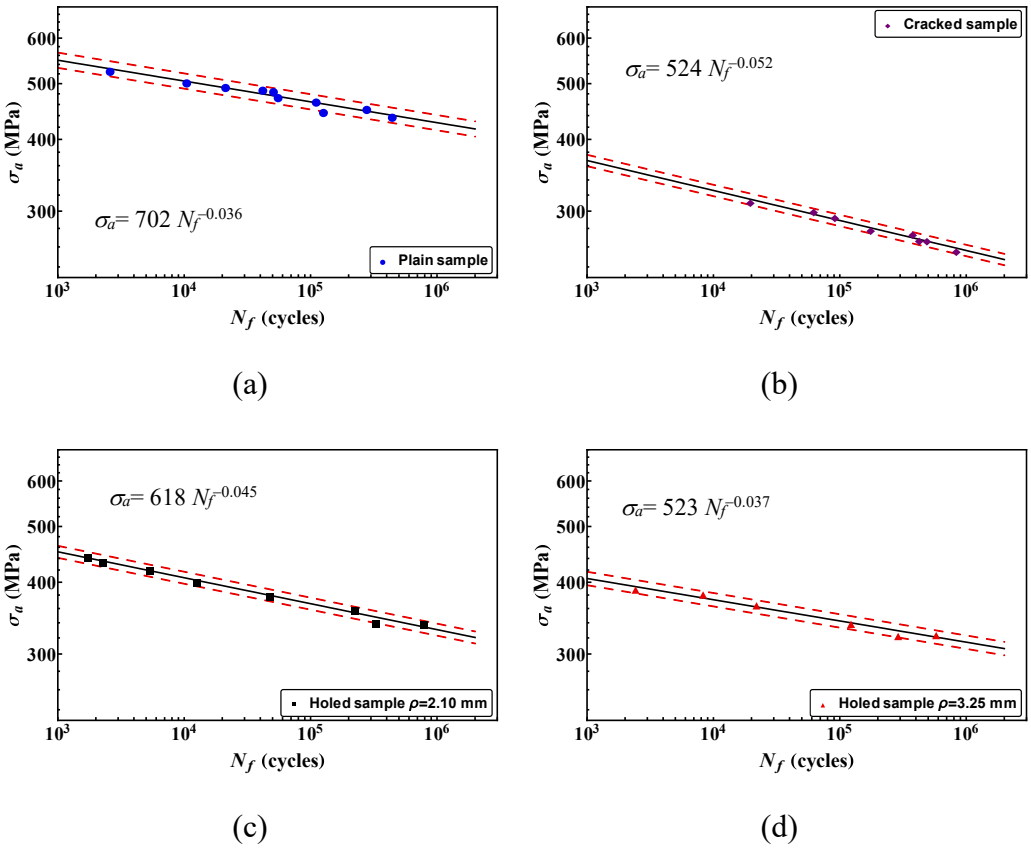

Fig. 5-6. Stress-life diagrams for $[0/90]_{2s}$ composite laminate: (a) plain sample, (b) cracked sample, (c) sample weakened by a hole with radius ρ = 2.1 mm and (d) ρ = 3.25 mm. The dashed red lines represent a PS of 97.7% and 2.3%.

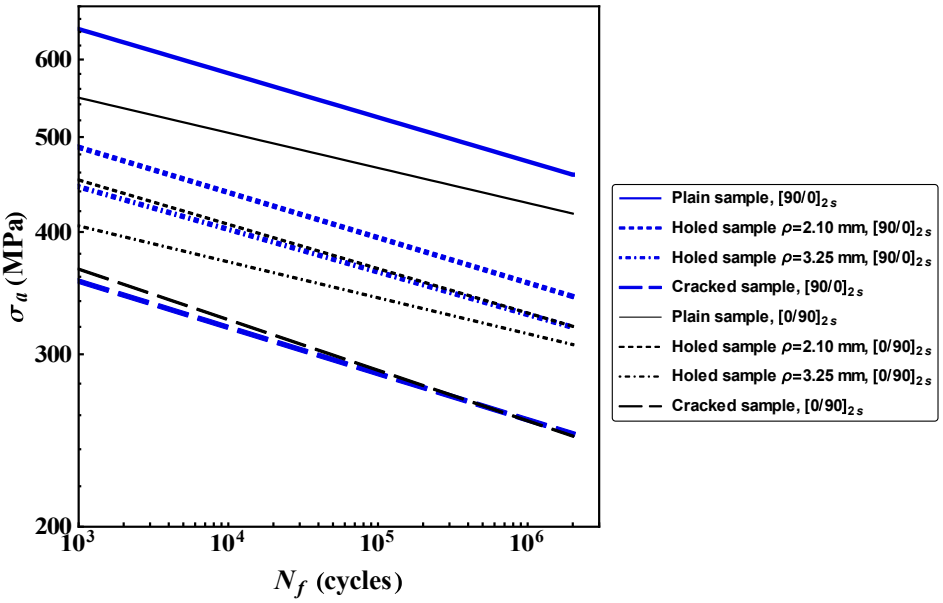

Fig. 5-7. Stress-life diagrams for all investigated composite laminates represented by power-law best-fitting curves for the eight experimental datasets.

To assess and compare the fatigue behavior of laminated composites, the best-fitting curves representing all the studied cases are delineated in Fig. 5-7. This illustration provides a proper insight into the fatigue performance of laminates, encompassing those with and without stress concentrators, subjected to varying loading regimes. An examination of these trends yields the following observations:

I) The $[90/0]_{2s}$ layup exhibits a higher fatigue resistance in comparison to the $[0/90]_{2s}$ layup.

II) With an increase in stress concentration, there is a decrease in the critical stress amplitude for the same number of cycles to failure. Furthermore, the disparity in critical stress amplitude between the two layups decreases.

III) In the case of holed specimens, the strength decreases – with a constant number of cycles – as the hole's radius increases. This behavior is consistent with the conventional size effect observed in isotropic materials [85], confirming the assumption that the primary failure mechanism in these samples is pull-out rather than delamination.

5.5 Results and discussion

Within this section, data obtained from fatigue tests concerning both plain and cracked structures are employed to define the free parameters of the model. Specifically, this involves deriving the two functions $X_f(N)$ and $K_{If}(N)$ to

characterize the model. Following this characterization, predictions are obtained for the two structures containing circular holes, utilizing both the TCD and FFM methods. Additionally, a comprehensive parametric study is performed to analyze the influence of the hole radius on fatigue lives.

5.5.1 Model characterization and validation

As mentioned, the models rely on functions $X_f(N)$ and $K_{If}(N)$ as inputs. Utilizing the best-fitting procedure on the stress-life data of plain specimens (as depicted in Fig. 5-5a and Fig. 5-6a, values of a_s and b_s in Eq. (4-1) are determined and are summarized in Table 5-3 for each respective stacking sequence. Similarly, the SIF-life data from cracked specimens (Fig. 5-5b and Fig. 5-6b) lead to the derivation of a_k and b_k values, as outlined in Eq. (1-9) or Eq. (4-2). The calculated values for these input parameters are reported in Table 5-3.

Table 5-3. The computed values of a_s, b_s, a_k and b_k for both layups.

Layup	$X_f(N) = a_x\ N^{-b_x}$ [MPa]	$K_{If}(N) = a_k\ N^{-b_k}$ [MPa $\sqrt{\text{m}}$]
$[90/0]_{2s}$	a_s = 879 [MPa]	a_k = 98 [MPa$\sqrt{\text{m}}$]
	b_s= 0.045	b_k = 0.047
$[0/90]_{2s}$	a_s = 702 [MPa]	a_k = 107 [MPa$\sqrt{\text{m}}$]
	b_s = 0.036	b_k = 0.052

Given $X_f(N)$ and $K_{If}(N)$, blind predictions can be formulated for the fatigue data of specimens with holes. In employing the TCD method, Eq. (1-11) must be solved. However, in order to solve the equation, first the critical distance should be determined based on Eq. (1-10). In contrast, to obtain the predictions by FFM approach, Eq. (4-5) should be solved.

To further evaluate the behaviors of both TCD and FFM models, Fig. 5-8 depicts the relationship between the crack advance (critical distance) and N_f, as predicted for both the $[0/90]_{2s}$ and $[90/0]_{2s}$ stacking sequences. Within this figure, the solid line represents the critical distance, as computed via Eq. (1-10), while the finite crack advance is calculated through the solution of the system expressed in Eq. (4-5). Additionally, the triangular data points in the plot are correlated with a value of ρ = 2.1 mm, and the circular data points are corresponded to a ρ value of 3.25 mm.

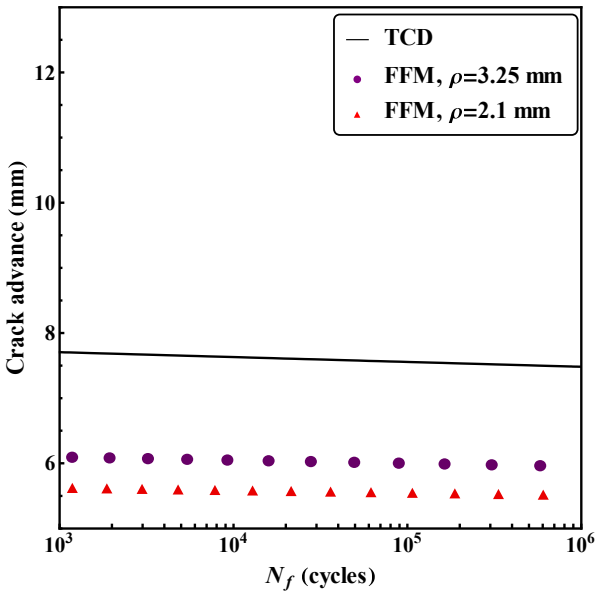

(a)

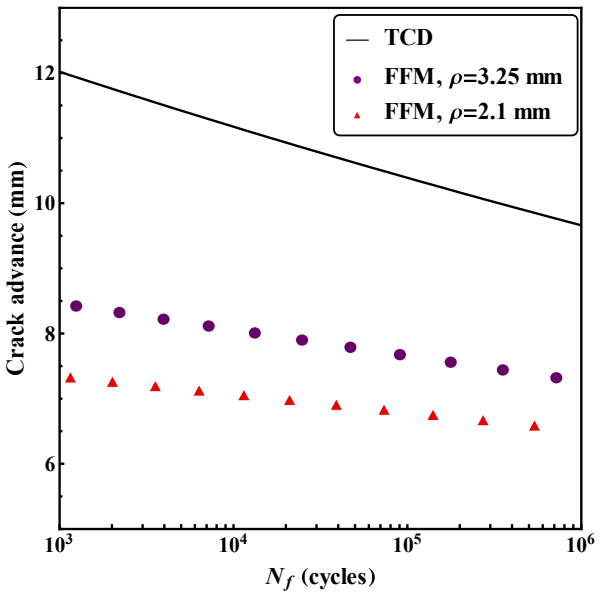

(b)

Fig. 5-8. Depiction of the crack advance in relation to N_f for (a) $[90/0]_{2s}$ and (b) $[0/90]_{2s}$ layups, presented on a linear-logarithmic scale. The solid line serves to denote the critical distance, while the triangular markers are associated with $\rho = 2.1$ mm. The circular data points, conversely, correspond to $\rho = 3.25$ mm.

The figure presents a clear understanding that the finite crack advance, as calculated by FFM, is a function of both the inherent material properties and the specific geometric features. In this scenario, a reduction in the notch radius leads to a smaller finite crack advance, which consistently stays below the TCD critical distance. Furthermore, when keeping N_f constant, the relationship between the critical distance and finite crack advance for the $[0/90]_{2s}$ layup is found to be greater than that for the $[90/0]_{2s}$ layup, with a more noticeable difference in the number of cycles. It can therefore be concluded that the $[0/90]_{2s}$ layup's damage zone is more extensive than that of the $[90/0]_{2s}$ layup, resulting in the latter's increased strength, as previously illustrated (Fig. 5-7).

Another observation worth noting is related to the $[90/0]_{2s}$ layup for a sample with a 2.1 mm notch radius. Here, the critical distance exceeds the sample's ligament. To solve this issue in the TCD method, a fixed critical distance of 10.4 mm is applied to this specific sample, under the assumption that this span encompasses the entire ligament. However, this assumption might influence TCD method's capability to accurately predict fatigue life.

For a thorough assessment, Fig. 5-9 reports the SN diagrams, as predicted by both the TCD and FFM models, supported by experimental data for each type of notched geometry and stacking sequence.

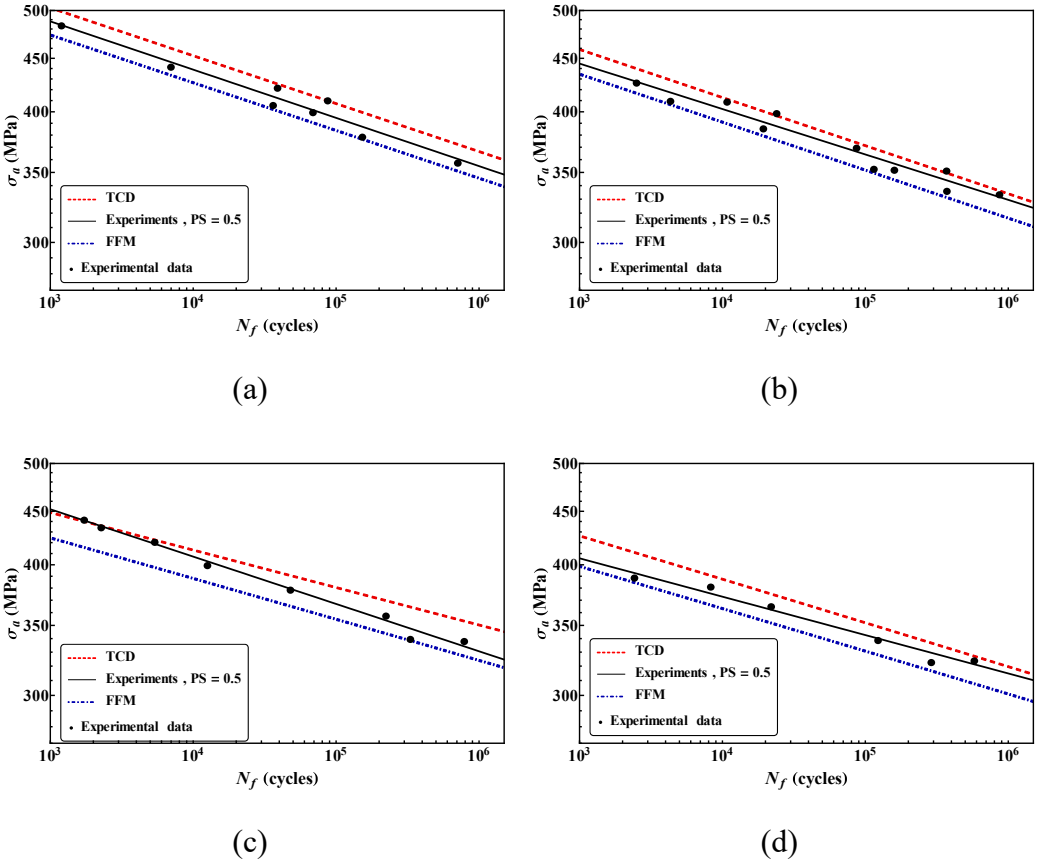

Fig. 5-9. SN Diagrams, featuring both experimental data and forecasts from the TCD and FFM models, for the following configurations: (a) $[90/0]_{2s}$ layup with a notch radius $\rho = 2.1$ mm, (b) $[90/0]_{2s}$ layup with $\rho = 3.25$ mm, (c) $[0/90]_{2s}$ layup with $\rho = 2.1$ mm, and (d) $[0/90]_{2s}$ layup with $\rho = 3.25$ mm.

From an examination of Fig. 5-9, it becomes apparent that the theoretical fatigue life predictions align closely with the median fit line (with PS equal to 0.5) observed in the experimental data. Notably, the outcomes from FFM are consistently located beneath this median line across all the considered scenarios, reflecting an inherent tendency towards conservative estimations. Conversely, the TCD predictions are found to be greater than the median line, thus leading to predictions that are typically less conservative. It is of significance to underline that in Fig. 5-9c (corresponding to the $[0/90]_{2s}$ layup with $\rho = 2.1$ mm), a constant critical distance of 10.4 mm is adopted, in agreement with prior discussions.

Furthermore, Fig. 5-10 and Fig. 5-11 showcase the theoretical versus experimental comparison in a different manner, specifically comparing the predicted fatigue life N_f and the actual experimental values $N_{f,exp}$. Fig. 5-10 shows the results obtained by TCD, whereas Fig. 5-11 provides a presentation of the outcomes by FFM. Within both figures, a solid black line (angled at 45°) illustrates the precise estimations, with the region above referring to conservative predictions.

Dashed blue lines are representative of the 1/3 and 3 scatter bands, while the dotted-dashed gray lines denote the 1/5 and 5 scatter bands.

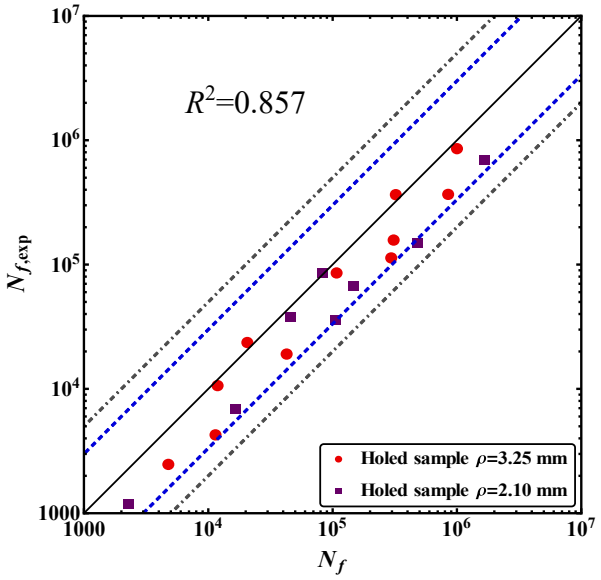

(a)

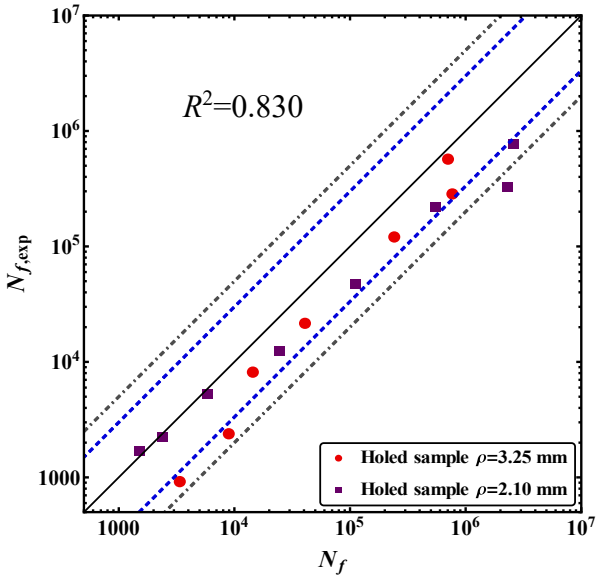

(b)

Fig. 5-10. A comparison of the number of cycles to failure between experimental data, denoted as $N_{f,exp}$, and TCD predictions, denoted as N_f, for two configurations: (a) $[90/0]_{2s}$, and (b) $[0/90]_{2s}$. Dashed blue lines delineate the scatter bands of ratios 1/3 and 3, while dotted-dashed gray lines depict the scatter bands corresponding to ratios 1/5 and 5.

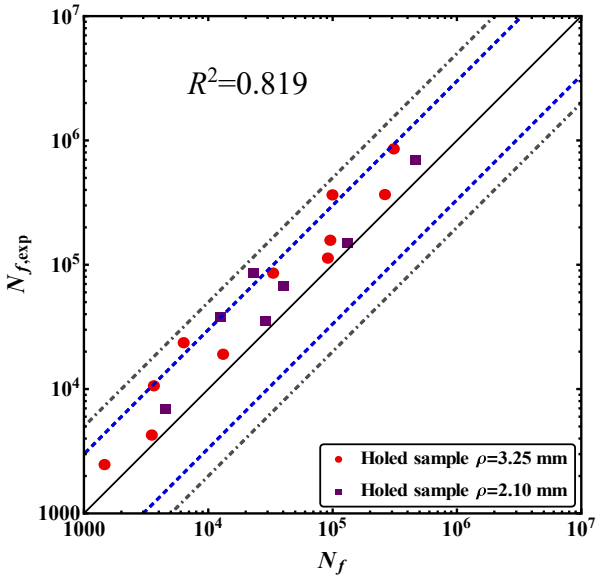

(a)

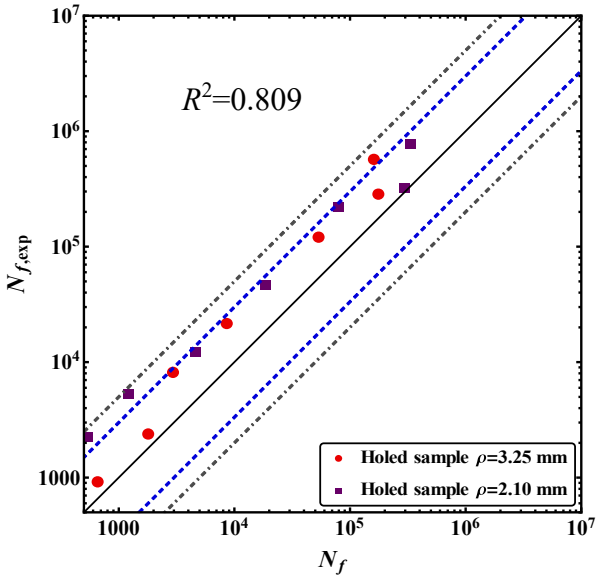

(b)

Fig. 5-11. A comparison of the number of cycles to failure between experimental data, denoted as $N_{f,exp}$, and FFM predictions, denoted as N_f, for two configurations: (a) $[90/0]_{2s}$, and (b) $[0/90]_{2s}$. Dashed blue lines delineate the scatter bands of ratios 1/3 and 3, while dotted-dashed gray lines depict the scatter bands corresponding to ratios 1/5 and 5.

Both TCD and FFM approaches show a remarkable capability in forecasting the fatigue life of laminated composite materials. The correlation coefficients, R^2 (already introduced in Chapter 4), determined from a natural logarithm transformation of the collected data, lie within a range of 0.81 to 0.86. This range underscores the effectiveness of the employed models. Here, the TCD approach appears to be more precise, whereas FFM outcomes are consistently inclined towards the conservative side.

5.5.2 Examination of radius impact in holed samples

A detailed parametric investigation has been performed to understand the influence of the hole radius on the lifetime of $[90/0]_{2s}$ and $[0/90]_{2s}$ layups. This study presents only the findings derived from the FFM model, which was proved to be more conservative. The examination extends to cyclic loadings what was previously done in a static framework by Camanho et al. [85]. To overcome numerical problems and sidestep potential physical complications tied to finite width, the width of all specimens has been held constant to $W = 1000$ mm (a value noticeably greater than the largest hole radius). Fig. 5-12a elucidates the connection between hole radii and the nominal stress amplitude, denoted as σ_a, for specific lifetimes N_f, on the other hand, Fig. 5-12b presents the influence of hole radius on the lifetime for designated stress amplitudes σ_a. It is pertinent to note that the stress amplitudes in Fig. 5-12b are scaled according to the strength of unnotched samples for 1000 cycles (with differing values for each stacking sequence). Moreover, the selection of stress amplitude values has been carried out to facilitate a comparative assessment of the size effect behavior between the two layups, both for a uniform absolute value and a consistent relative value, in relation to their unnotched strength for 1000 cycles.

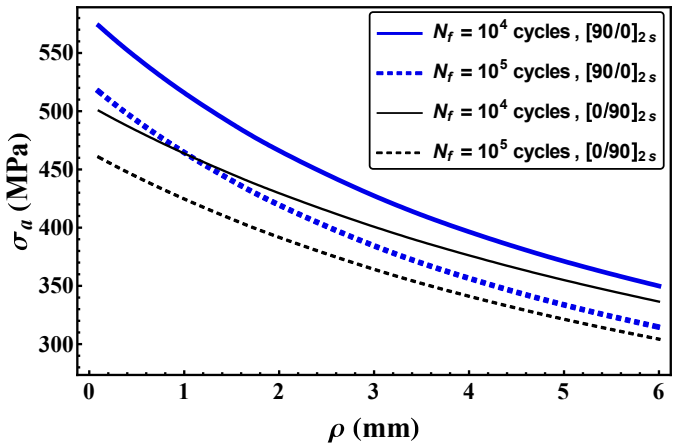

(a)

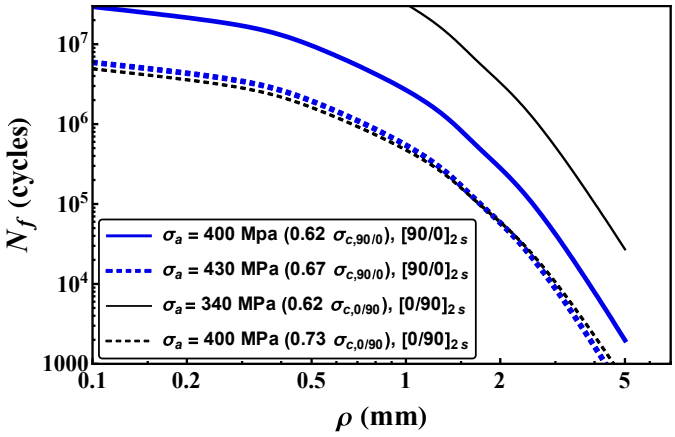

(b)

Fig. 5-12. (a) Illustration of the relationship between the hole radius and nominal stress amplitude (considering the gross-section) for specific fatigue lives. (b) Depiction of the influence of the hole radius on fatigue life, given constant stress amplitudes, presented on a logarithmic scale for both axes.

From Fig. 5-12 the following observations can be outlined:

I) An increase of the hole radius results in a corresponding reduction in the required stress amplitude to reach an equivalent fatigue life (as depicted in Fig. 5-12a); Conversely, at a constant stress amplitude, the fatigue lifetime diminishes with the expansion of the hole radius (as shown in Fig. 5-12b).

II) For fixed fatigue lifetimes, differences in performance between the layups become more pronounced with smaller hole dimensions, or conversely, both layups tend to demonstrate analogous behavior with an increase in notch radius.

III) The $[90/0]_{2s}$ layup shows superior fatigue endurance relative to the $[0/90]_{2s}$ layup, in coordinate with the observations in Fig. 5-7.

IV) The $[90/0]_{2s}$ layup is slightly more sensible to notches, which is apparent from the steeper gradient of the corresponding curves.

Chapter 6

Implementation of Phase Field to Model Fatigue Failure[4]

6.1 Introduction

The study of fatigue failure is still a critical problem across various industrial and research domains, primarily due to its significant role in the failure of engineering structures. A notable advancement in this area is the application of the Phase Field method to fatigue phenomena, starting from its origins in brittle fracture modeling. This method, fundamentally based on Griffith's criterion within a variational framework, was revolutionized by Francfort and Marigo [23], later extended by Bourdin et al. [24] through regularization techniques proposed by Ambrosio and Tortorelli [189]. Such regularization facilitates modeling without predefined crack paths, enabling the capture of crack nucleation and propagation without the need for remeshing.

Efforts to adapt the Phase Field method for fatigue involve either modifying the critical energy release rate over time or introducing an additional energy term to represent fatigue damage accumulation. Among the first ones to adapt Phase Field models for fatigue were Alessi et al. [104] and Carrara et al. [105], focusing on fracture energy degradation. Alternative models, such as those by Grossman-Ponemon et al. [190] and Seiler et al. [107,108], employ continuous cycle counting or the local strain approach to circumvent cycle-by-cycle analysis, aiming for efficient fatigue lifetime prediction. Boldrini et al. [101] and Schreiber et al. [110] represent another strategy by integrating fatigue-specific driving forces, a concept that enhances the model's fidelity to microscopic fatigue effects. Despite these advancements, the high computational demand of accurately simulating millions of loading cycles remains a significant challenge, impeding the practical application of Phase Field models in high cycle fatigue regimes. To address computational efficiency, several strategies have been proposed, including adaptive mesh refinement [191–193], specialized elements [194,195], and modified solution

[4] Some parts of this chapter have been adapted from our work currently under review as "Heinzmann, J., Carrara, P., Ambati, M., Mirzaei, A. M., and De Lorenzis, L., An Adaptive Acceleration Scheme for Phase-Field Fatigue Computations, Comput. Mech."

algorithms [17, 24, 39, 71]. Notably, the cycle jump method, introduced by Lemaitre and Doghri [41] and further developed by Seleš et al. [196], and Haveroth et al. [101], offers a promising avenue for reducing computation times by skipping explicit cycle resolutions through predictive modeling.

This chapter outlines the core concepts of the Phase Field approach to fatigue failure, based on studies [104,105]. It then briefly introduces an innovative, fully adaptive cycle jumping method that significantly lowers computational demands while ensuring minimal errors [197]. Following this, the model is rigorously validated against available experimental data to accurately establish the Paris curve.

6.2 Extension of Phase Field model to fatigue

Considering that the foundational theory of Phase Field models, as laid down by Griffith concerning crack propagation, posits that a crack can only expand when the energy release rate surpasses a certain threshold, a contradiction emerges when one considers the nature of fatigue crack growth, which notably occurs under sub-critical load conditions. To adjust this within the Phase Field approach, one can consider two distinct, yet sophisticated avenues of adaptation for the model in the context of fatigue. The first approach would involve a gradual, history dependent reduction of the critical energy release rate, i.e. effectively lowering the threshold for crack advancement. Alternatively, the second approach involves the incorporation of an extra contribution of energy dissipation specifically related to fatigue, therefore enhancing the driving force behind crack propagation based on same representative fatigue history variable. Following the work by Carrara et al. [105], this chapter is based on the first category of models.

To integrate the effects of fatigue, the fracture energy density (Eq. (1-16)) can be modified based on a cumulated history variable [105]:

$$\begin{aligned}\varphi_F(d,\bar{\alpha}) &= \int_0^t f(\bar{\alpha}(\tau))\,\dot{\varphi}(d)\,\mathrm{d}\tau = \int_0^t f(\bar{\alpha}(\tau))\left(\frac{\partial\varphi}{\partial d}\dot{d}+\frac{\partial\varphi}{\partial\nabla d}\nabla\dot{d}\right)\mathrm{d}\tau \\ &= \int_0^t f(\bar{\alpha}(\tau))\frac{G_c}{4c_w}\left(\frac{w(d)}{l}\dot{d}+2l\nabla d.\nabla\dot{d}\right)\mathrm{d}\tau\end{aligned} \tag{6-1}$$

In the equation above, t represents pseudo-time, $\bar{\alpha}(\tau)$ shows a cumulated history variable, and $f(\bar{\alpha}(\tau))$ is fatigue degradation function. $\bar{\alpha}(\tau)$ can be defined as an accumulation of any scalar measure α that comprehensively characterizes the fatigue history endured by the material, satisfying the requisite property of $\dot{\bar{\alpha}}(\tau)\geq 0$. For the meanings of the other parameters, please refer to Section 1.6. Given that the model presented is energy-based, it is logically coherent to take into

consideration the active part of the elastic strain energy density as the fatigue history variable, α.

Several choices are available for the mentioned parameters. Considering the effect of mean load of cycles, two different cumulative history variables can be defined. For mean load independent, we have:

$$\bar{\alpha}(\tau) = \int_0^t H(\alpha\,\dot{\alpha})\left|\dot{\alpha}\right| \mathrm{d}\tau \tag{6-2}$$

where $H(\alpha\dot{\alpha})$ shows a Heaviside function to accumulate the fatigue effect only for loading phases (it is one for loading, and zero for unloading). Considering mean load independent, one can introduced a function that has different weights for the rate of the cumulated variable, as:

$$\bar{\alpha}(\tau) = \frac{1}{\alpha_N}\int_0^t H(\alpha\,\dot{\alpha})\,\alpha\,\dot{\alpha}\,\mathrm{d}\tau \tag{6-3}$$

Furthermore, the function $f(\bar{\alpha}(\tau))$, known as the fatigue degradation function, mathematically describes the intensity of reducing the fracture toughness during fatigue loading. It can be defined by a general function as:

$$f(\bar{\alpha}) = \begin{cases} 1, & \bar{\alpha} > \bar{\alpha}_{th} \\ \left(1 - q\dfrac{\bar{\alpha} - \bar{\alpha}_{th}}{\bar{\alpha} + \bar{\alpha}_{th}}\right)^p, & \bar{\alpha} > \bar{\alpha}_{th} \end{cases} \tag{6-4}$$

where p and q should be calibrated based on experimental data. $\bar{\alpha}_{th}$ demonstrates the point at which the fatigue effect is triggered and is also obtained based on experimental data. It should be noted that Eq. (6-4) is chosen to encompass a wide range of degradation functions, however, any non-increasing function that varies between 1 and 0 is applicable.

Finally, to obtain the governing equations, the initial step involves considering the total energy functional.

$$
\begin{aligned}
E_l(\boldsymbol{u}, d, \bar{\alpha}) = & \int_{\Omega} g(d)\psi^{+}_{el,0}(\boldsymbol{\varepsilon}) + \psi^{-}_{el,0}(\boldsymbol{\varepsilon})\mathrm{d}\boldsymbol{x} \\
& + \int_0^t \int_{\Omega} f(\bar{\alpha}(\tau)) \frac{\mathcal{G}_c}{4c_w}\left(\frac{w'(d)}{l}\dot{d} + 2l\nabla\dot{d}\nabla d\right)\mathrm{d}\boldsymbol{x}\,\mathrm{d}\tau \\
& - \int_{\Omega} \rho\boldsymbol{b}.\boldsymbol{u}\,\mathrm{d}\boldsymbol{x} - \int_{\partial\Omega_N} \boldsymbol{t}.\boldsymbol{u}\,\mathrm{d}a
\end{aligned}
\tag{6-5}
$$

Note that the last two terms are potential energy of body force, $\boldsymbol{b}$, and traction vectors, $\boldsymbol{t}$, where ρ represents the mass density. Furthermore, considering the introduction of $\bar{\alpha}(\tau)$ that brings in a history-dependency, the formulation diverges from the brittle fracture model where the energy dissipation could be neatly categorized as a state function. In this context, the energy loss becomes intricately linked to the sequence of events that have unfolded, implying that it is influenced by all the previous states the system has gone through.

Employing integration by parts technique, then, first-order stability principle, and finally, standard arguments of variational calculus, one can obtain the following governing equations related to the damage and mechanical problems:

$$
\frac{\partial\psi_e}{\partial d} - \frac{\mathcal{G}_c\, l}{2c_w}\left[f(\bar{\alpha})\left(\Delta d - \frac{w'(d)}{2l^2}\right) + \nabla f(\bar{\alpha}).\nabla d\right] = 0, \qquad \mathrm{div}\,\boldsymbol{\sigma} + \boldsymbol{b} = 0 \quad \text{in}\,\Omega
\tag{6-6}
$$

and these boundary conditions:

$$
\boldsymbol{\sigma}.\boldsymbol{n} = \boldsymbol{t}_n \quad \text{on}\,\partial\Omega_N, \qquad \boldsymbol{u} = \bar{\boldsymbol{u}} \quad \text{on}\,\partial\Omega_D, \qquad \nabla d.\boldsymbol{n} = 0 \quad \text{on}\,\partial\Omega_D
\tag{6-7}
$$

In the context of numerical implementation of Eq. (6-6), the most common schemes for solving the Phase Field equations are the monolithic and staggered approaches. However, advancements in computational methodologies and the need for more efficient and robust solutions have led to the exploration and development of alternative strategies. The staggered scheme in the context of Phase Field modeling represents a pivotal computational strategy aimed at solving the coupled partial differential equations (PDEs) that govern the evolution of fracture and damage in materials. This approach systematically segregates the solution of the mechanical and phase field problems into separate, sequential steps, thereby simplifying the computational complexity inherent in simultaneously resolving the coupled system. Specifically, the mechanical problem is solved first to update the displacement and stress fields, followed by the resolution of the Phase Field problem, which updates the damage based on the newly computed mechanical state. This decoupling facilitates the use of different solvers or numerical techniques tailored to the specific characteristics of each sub-problem, enhancing computational efficiency and stability. For further information, see [32].

To determine the numerical results, Eq. (6-6) which is written in weak form should be solved. Following this, they are discretized employing linear finite elements and subsequently reformulated into incremental form. Once prepared, Eq. (6-6) is solved through a staggered scheme as in [32].

In the context of time-discretized framework, the fatigue history variable can be presented as follows:

$$\bar{\alpha}_{n+1} = \bar{\alpha}_n + \int_{t_n}^{t_{n+1}} \dot{\bar{\alpha}}\, \mathrm{d}\tau = \bar{\alpha}_n + \Delta\bar{\alpha} \tag{6-8}$$

For mean load independent accumulation function (Eq. (6-2)), we have:

$$\Delta\bar{\alpha} = \left|\alpha_{n+1} - \alpha_n\right| H\left(\frac{\alpha_{n+1} - \alpha_n}{\Delta t}\right) \tag{6-9}$$

While for mean load dependent accumulation function (Eq. (6-3)), we have:

$$\Delta\bar{\alpha} = \frac{\left(\alpha_{n+1} - \alpha_n\right)}{\alpha_n}\left(\frac{\alpha_{n+1} - \alpha_n}{2}\right) H\left(\frac{\alpha_{n+1} - \alpha_n}{\Delta t}\right) \tag{6-10}$$

This section briefly (since the model is well-developed in the literature and is not the aim of this chapter) discusses the fundamentals of extending the Phase Field approach to fatigue. In the following section, these equations are used to obtain numerical results.

6.3 1D bar case study

In order to have a better insight into how the model works, and the effects of each parameter, it is advisable to start the analyses with the simplest case: a one-dimensional problem.

Consider an unstretched and undamaged one-dimensional continuum bar, fixed at one end and subjected to a time-varying displacement, $\bar{u}(t)$, at the other end, as shown in Fig. 6-1. The displacement boundary conditions establish a clear definition of how the bar is constrained and how it is expected to deform over time.

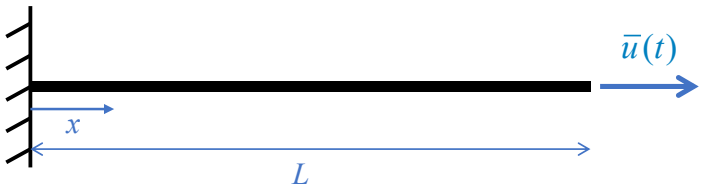

Fig. 6-1. One-dimensional fatigue test setup.

Consider the following values and inputs for numerical modeling of the problem: $L = 2$ m, $\bar{u}_{max} = 0.85$, $E = 1$ Pa, $\mathcal{G}_c = 0.071$ J/m^2. Regarding the mesh size, following the literature [105], a spatial discretization of $l/5$ was employed. For the AT1 model, $l = 0.177$ m was used (Eq. (1-24)), while, to maintain equivalent ultimate strength across both models, $l = 0.05$ m was adopted for the AT2 model (Eq. (1-25)), for more information, see [28]. Moreover, for the sake of simplicity, the mean load independent accumulation function (Eq. (6-2)) was used. Fig. 6-2 presents numerical results based on AT1 model while Fig. 6-3 is related to AT2 model. In each figure, parts a) show accumulated history variable, parts b) illustrate the growth of damage localization for entire bar at each cycle and parts c) present stress-displacement diagram.

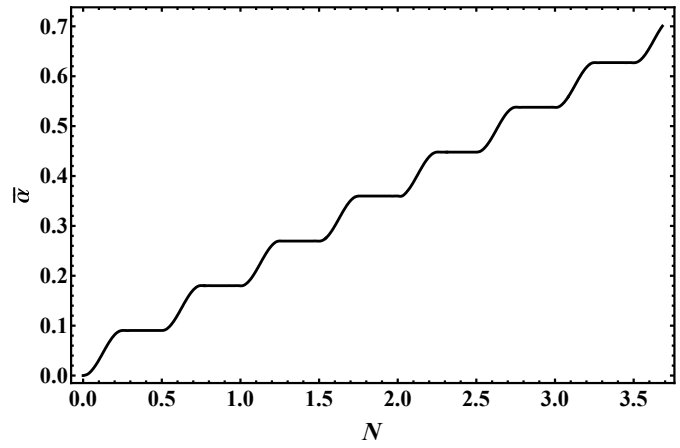

(a)

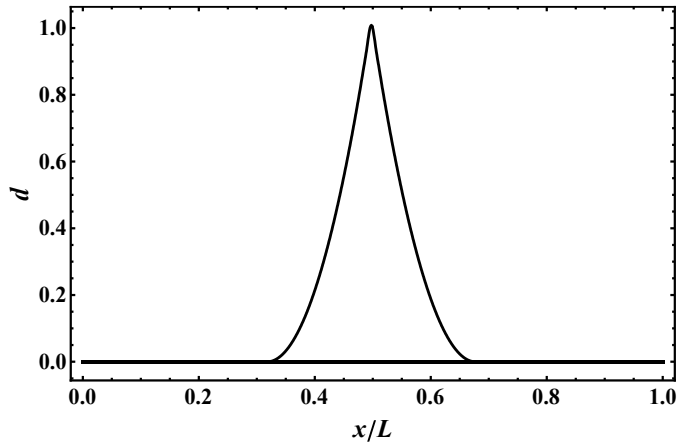

(b)

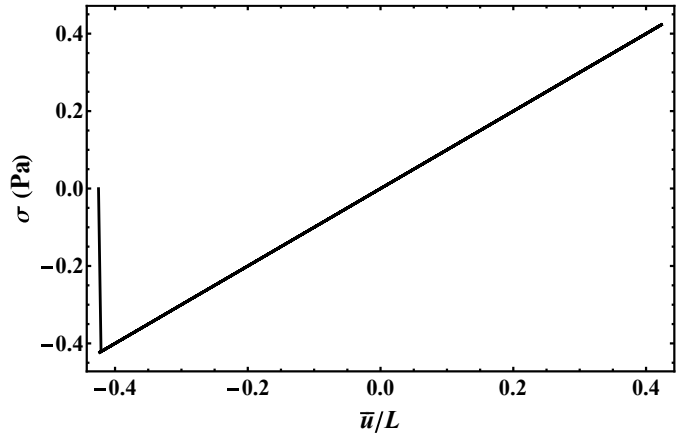

(c)

Fig. 6-2. Numerical response of a bar subjected to a cyclic loading based on AT1 model. (a) accumulated history variable at the end of all cycles, (b) damage localization growth for entire bar at each cycle and (c) stress-displacement diagram.

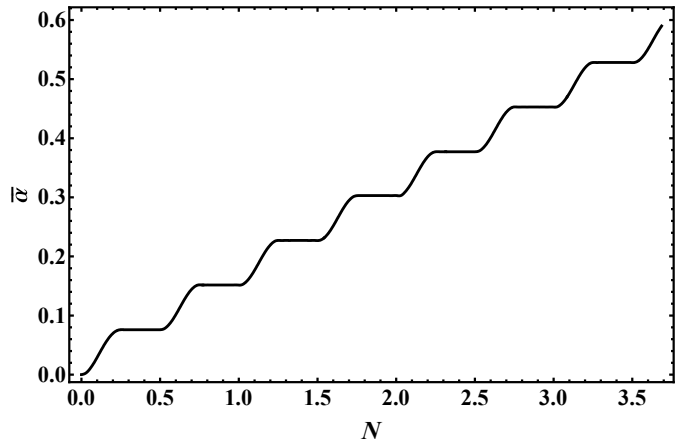

(a)

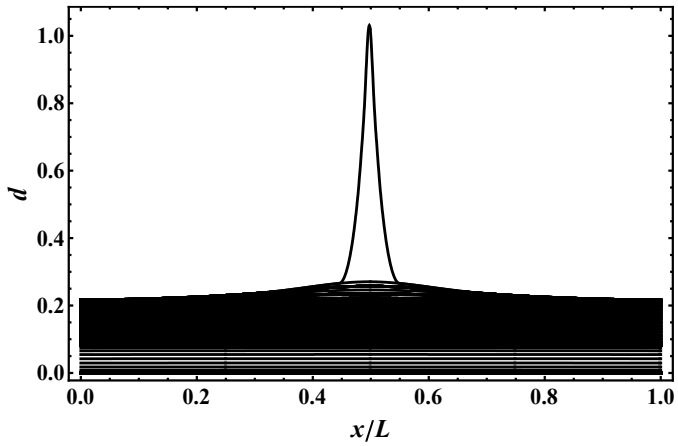

(b)

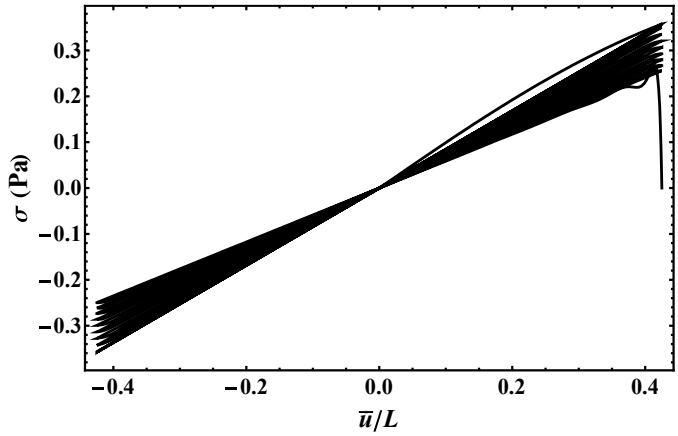

(c)

Fig. 6-3. Numerical response of a bar subjected to a cyclic loading based on AT2 model. (a) accumulated history variable at the end of all cycles, (b) damage localization growth for entire bar at each cycle and (c) stress-displacement diagram.

Considering the accumulated history variable, part a), it can be seen that it considers four different stages of loading and unloading during a cycle, while it only increases during two loading phases. Comparing this parameter for both AT1 and AT2 models, it can be seen that although they are quite similar, the accumulated history variable is slightly higher for the AT1 model. Based on part b), for the cyclic damage profile, it is clear that the results are quite different; for AT2, damage increases uniformly along the bar for some cycles, then localization starts, and by increasing the damage at the localized point, failure happens. In contrast, for AT1, as soon as the threshold is met, failure occurs and there are no cyclic damage growth stages. This behavior of the AT1 model can be observed in Fig. 6-2 part c), since no cyclic stress softening can be seen, and the stress suddenly drops to zero. While for the AT2 model, as shown in Fig. 6-3 part c), the stress decreases due to cyclic loading, and failure occurs. It should be noted that, similar to the static loading, the stress-displacement relationship for AT1 is linear, while for AT2, as soon as we load the sample, the damage starts. This might justify the slightly lower accumulated history variable for the AT2 model. It should be noted that for AT1, the bar fails after 4 cycles, while it is 13 cycles for the AT2 model. The number of cycles to failure was intentionally chosen to be low to show the different stages of fatigue modeling by the Phase Field in more detail.

Finally, it is worth to note that since the fatigue extension model shares the basics with the standard (static) Phase Field, the effect of mesh size and length scale is not studied here. On the other hand, regarding one-dimensional analyses of fatigue failure using the Phase Field approach, the reader can refer to [104]. However, it worth to mention that in [104], the Authors employed strain as the fatigue history variable, while it was later shown that employing strain for two-dimensional cases results in mesh-dependent simulations since it is singular around the crack tip, as seen in [105]. Therefore, the results for one-dimensional analyses are original.

6.4 2D case study

6.4.1 A brief introduction on the cycle jump approach

While the study of Phase Field models for fatigue analysis in one-dimensional (1D) settings has been relatively straightforward, extending these models to two-dimensional (2D) applications significantly increases computational demands, typically requiring several days for a single analysis. To enhance the efficiency of this approach, the introduction of a cycle jump technique seems advantageous. This computational strategy accelerates fatigue simulations by skipping a specified number of load cycles, effectively decreasing the total count of cycles necessary for a comprehensive analysis. It is important to mention that the principal objective of this chapter is to extend the application of the Phase Field approach to the domain of fatigue analysis. This involves a detailed examination of critical parameters and

the subsequent validation of the model against a set of experimental data to derive the Paris curve. However, a concise overview of the cycle jump methodology, set to be detailed in an upcoming publication in collaboration with researchers from ETH, is provided. This overview offers a preliminary insight into the method's contribution to the field. For an in-depth discussion, the reader is referred to [197].

The development of the adaptive acceleration strategy is inspired by a key observation: fatigue effects are most pronounced around the crack tip. This insight is crucial, as it directs our focus towards improving the accuracy of system state forecasts during cycle jumps, which is vital for understanding the dynamic nature of fatigue without overburdening the computational resources. A key aspect of this approach is the adaptive determination of the cycle jump size (ΔN), intended to ensure a balance between predictive accuracy and computational efficiency.

A point-wise finite difference (FD) method is employed to forecast system evolution, primarily since it has a light computational load, and lends to the necessary adaptation. This method works by using a Taylor series expansion to predict the state of a variable $\Theta(\boldsymbol{x},N)$ at the most recently resolved cycle before making a jump, which gives:

$$\Theta(\boldsymbol{x},N+\Delta N)=\Theta(\boldsymbol{x},N)+\Theta'(\boldsymbol{x},N)\Delta N+\Theta''(\boldsymbol{x},N)\frac{(\Delta N)^2}{2}+\mathrm{O}\left[(\Delta N)^3\right] \tag{6-11}$$

Here, $\Theta'(\boldsymbol{x},N)$ and $\Theta''(\boldsymbol{x},N)$ represent the first and second cycle count derivatives, respectively, approximated using backward finite differences from recent cycle data. For this approach, we select a stencil size of 4, which means we explicitly calculate four cycles between each cycle jump. Consequently, the formula for predicting $\Theta(\boldsymbol{x},N+\Delta N)$ is derived as follows:

$$\begin{aligned}\Theta(\boldsymbol{x},N+\Delta N)\approx{}&\Theta(\boldsymbol{x},N)\\&+\frac{-2\Theta(\boldsymbol{x},N-3)+9\Theta(\boldsymbol{x},N-2)-18\Theta(\boldsymbol{x},N-1)+11\Theta(\boldsymbol{x},N)}{6}\Delta N\\&+\frac{-\Theta(\boldsymbol{x},N-3)+4\Theta(\boldsymbol{x},N-2)-5\Theta(\boldsymbol{x},N-1)+2\Theta(\boldsymbol{x},N)}{2}(\Delta N)^2\end{aligned} \tag{6-12}$$

This FD-based extrapolation scheme is distinguished by its direct application to discrete nodal or Gauss point locations, facilitating the efficient storage of state variable histories and ensuring negligible CPU time involvement.

In order for the model to calculate the proper number of cycles to jump, an adaptive scheme is chosen. The adaptation of cycle jump size is governed by a criterion aiming to constrain system evolution within specified limits, thereby maintaining the non-linearity and prediction errors at manageable levels. This

process is informed by monitoring a state variable $\Lambda(N)$, which reflects the system's fatigue progression. The "cycle jump criterion" is established as:

$$\Lambda(N+\Delta N)=\Lambda(N)+(\Delta\Lambda)_{allowed} \tag{6-13}$$

This criterion ensures that the system evolution during a jump matches a predetermined increment, leading to an explicit formula for ΔN based on potential non-linear evolutions:

$$\Delta N=\frac{-\tilde{\Lambda}_1+\sqrt{(\tilde{\Lambda}_1)^2-4\tilde{\Lambda}_2\left[\tilde{\Lambda}_0-\Lambda(N)-(\Delta\Lambda)_{allowed}\right]}}{2\tilde{\Lambda}_2} \tag{6-14}$$

In this formula, $\tilde{\Lambda}_1$, $\tilde{\Lambda}_2$, and $\tilde{\Lambda}_0$ serve as fitting parameters, facilitating an exact determination of the optimal number of cycles to be skipped. This innovative cycle jump criterion and prediction method collectively enhance the computational efficiency of fatigue analysis, allowing for the acceleration of simulations without compromising the precision required for accurate fatigue life assessments. Further details can be found in [197].

6.4.2 Validation with experimental data

In order to validate the model with available experimental data, the presented Phase Field approach in two-dimensional form is employed. This validation focuses on Al7075, a metal widely utilized in the fields of aerospace and automotive engineering. According to [198], the material properties are characterized by the elastic modulus (E) of 71700 MPa, Poisson's ratio (ν) of 0.33, and fracture toughness (K_{Ic}) of 18.75 MPa$\sqrt{\text{m}}$ which results in a critical energy release rate ($\mathcal{G}_c$) of 4.9 MPa mm. Through a series of trail and error steps, we determined that setting the parameters $q = 1$, $p = 3.3$, and $\bar{\alpha}_{th} = 15500$ J mm^{-3} optimally describes the fatigue degradation function, Eq. (6-4), and closely matched the Paris curve with $\mathrm{d}a/\mathrm{d}N = 2.268 \times 10^{-8}\,(\Delta K)^{3.16}$. The experimental setup in [198] adopted a mean load ratio (R) of 0.1 for the three-point bending test. The sample specified a geometry with a width of 40 mm and a thickness of 1 mm, under plane stress conditions. The computational mesh, finely detailed around the anticipated crack path, consists of 27,738 bilinear quadrilateral elements and 27,833 nodes, with a discretization parameter of $l/h = 5$. In terms of boundary conditions, the model fixes one node at the bottom left in all directions and another node at the bottom right in the direction of the load to emulate the support structure. The load is applied as a concentrated force at a node on the upper boundary, incorporating the strain tensor's spectral decomposition as suggested by Miehe et al. in [32]. The AT1 model, with $l = 0.2$ mm, was selected for conducting this analysis. The crack propagation rate curves, derived using the introduced cycle jumping approach, are depicted across different

loading intensities in Fig. 6-4, alongside the curve fitted to the Paris law based on the experimental findings reported in [198]. In the figure, experimental points are marked by red dots, the solid black line indicates the most accurate fit to these data, and various loading amplitudes are represented by differently colored lines showing the rate of crack expansion.

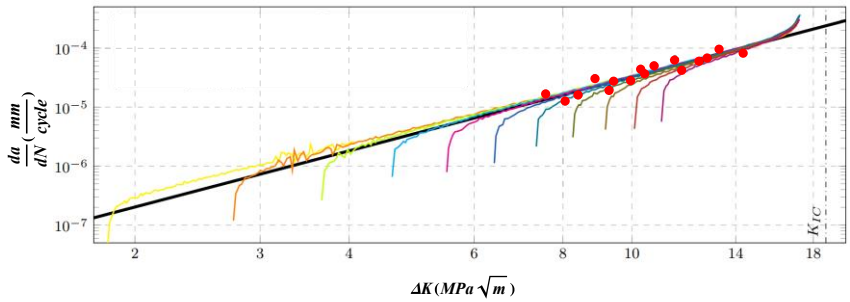

Fig. 6-4. Crack growth rate curves by Phase Field for the three-point bending test: The solid black line represents the best fitting line for experimental data, while the red dots depict the experimental points [198]**, and the colored lines illustrate crack growth rate curves for different loading amplitudes**

Based on Fig. 6-4, the proximity of the Phase Field model curves to the fitted line for the experimental data indicates a reasonable agreement between the theoretical predictions and the experimental observations. On the other hand, as ΔK increases, the crack growth rate (da/dN) also increases, which is consistent with the expected physical behavior of materials under fatigue loading. At lower levels of ΔK, the crack growth rate is relatively slow, which corresponds to the threshold region where cracks do not propagate significantly. Furthermore, by approaching ΔK to the material's fracture toughness (K_{IC}), the rate of crack growth increases sharply, ensuring failure would occur before reaching K_{IC}.

Chapter 7

Conclusions and Future Work

7.1 Conclusions

This thesis investigated the application of Finite Fracture Mechanics and Phase Field models for the study of debonding and fatigue failure in composite structures. This work addressed the critical need for efficient and comprehensive methodologies to predict the strength and durability of composite structures, especially under different complex loading conditions.

Chapter 3 examined the mechanics of debonding in direct shear by means of four one-dimensional interface models. These comprise three CZM models and the FFM approach. The closed-form solutions of these models provided important insights into the influence of different parameters on the debonding response in direct shear test configurations. The need for consideration of residual strength (friction) at the interface, even at the onset of debonding, was shown to be crucial. The models also showed high agreement in predicting the failure load in experimental data based on interface mechanical properties obtained from a single test, thus providing significant advantage for design and optimization.

Chapter 4 introduced a novel FFM model for finite life estimation of notched components under uniaxial cyclic loading. The model employed the Basquin equation to capture the variation in cyclic strength and SIF at failure calibrated from SN data to predict the life of various notch geometries under different loading amplitudes. The robustness of the model was demonstrated through agreement with a wide spectrum of experimental data from various notched configurations and materials. Furthermore, the FFM approach was used to describe the size effect of notched components. Similar to static loading, the model showed reliable results even for structures in which the TCD exceeds the net width of the specimen (making the TCD inapplicable in this case).

Chapter 5 extended TCD and FFM methodologies to address finite fatigue life of orthotropic materials containing drilled holes under tension-tension cyclic loading. These methodologies, in conjunction with the use of semi-analytical relationships for stress field and SIF calculations provided a framework for rapid and accurate fatigue life estimation. To validate the models, an extensive ad hoc

fatigue testing campaign on notched laminated composites was performed, encompassing four different specimens and two different layups, $[90/0]_{2s}$ and $[0/90]_{2s}$. Two geometries were utilized to determine the model input parameters, while the remaining ones served to validate the blind predictions by FFM and TCD models. The results were more than satisfactory; although the TCD model proved slightly more accurate, it was slightly less conservative compared to the FFM model. General observations revealed that the $[90/0]_{2s}$ layup exhibited superior fatigue strength compared to the $[0/90]_{2s}$ layup. However, this difference in strength decreased as stress concentration increased from plain to cracked specimens. This phenomenon was consistent with the conventional hole size effect, where the number of cycles to failure decreases as the hole radius increases. Further investigations through parametric studies showed the impact of hole radius on the fatigue lifetime of both configurations. The results indicated that as the hole size increased, the differences between the two layups decreased. This led to the observation that the $[90/0]_{2s}$ layup becomes more sensitive to notch size.

Chapter 6 explored the Phase Field method for fatigue in brittle materials. The method consists of modifying the standard phase-field free energy functional to account for a fatigue history variable that reduces the fracture toughness of the material. The choice of fatigue history variable along with the fatigue degradation function allows one to tailor the model to different materials. The chapter showed the capability of the approach to replicate the Paris curve for fatigue crack growth in brittle materials, while displaying the ability to capture effects beyond the Paris regime including nucleation and unstable crack propagation. An efficient “cycle jump” approach was also outlined aiming to accelerate simulations.

This research contributed to the field of composite structures by:

I) Developing new and efficient methodologies for debonding and fatigue failure of composite structures. The closed-form solutions from FFM and CZM models provide engineers a useful tool for predicting and understanding debonding behavior in externally bonded systems.

II) Demonstrating the FFM’s effectiveness in predicting the finite fatigue life of notched components. The model presented in Chapter 4 establishes a robust and accurate framework for estimating the life of notched components under a variety of notch geometries.

III) Extending the TCD and FFM methodologies to analyze the fatigue life of orthotropic materials with drilled holes. This development, discussed in Chapter 5, provides valuable insights into the behavior of composite laminates, ultimately leading to more reliable design strategies.

IV) Adapting the Phase Field method for fatigue analysis of real tests. The framework presented in this thesis provides a promising approach to analyzing

fatigue crack growth and failure in brittle materials, with potential applications to a variety of brittle composite systems.

V) These findings have important implications to a number of industries, including aerospace, automotive, and civil engineering, where the reliable, safe operation of composite structures is critical. The methods developed in this work provide engineers with a set of tools that can be used to:

- Design composite structures for maximum strength and durability

- Develop and implement efficient maintenance and inspection protocols,

- Improve the overall safety and reliability of composite structures in a wide range of applications.

7.2 Future work

This thesis represents a significant step towards leveraging FFM and Phase Field modeling to investigate the fatigue and fracture behavior of composite structures. However, realizing a comprehensive understanding and predictive capabilities require further exploration of the following key areas.

In the current work, it was shown that FFM is effective in analyzing debonding in direct shear tests. Future work should endeavor to:

I) Expand the scope of geometries and loading conditions: Real-world applications typically involve complex geometries and a variety of loading scenarios beyond the direct shear test. Extending the FFM framework to adhesively bonded joints that are subjected to complex loading, such as combined tension, shear, and/or bending, is critical for practical implementation.

II) Incorporate environmental effects: The influence of environmental factors, such as moisture and temperature, on debonding behavior should not be neglected. Future research should seek to incorporate these effects into the FFM model through environmentally dependent material properties.

The established FFM-based model for fatigue life estimation of notched components has set the stage for advancing to the next level through various avenues:

I) Incorporating crack propagation mechanisms: The current model is limited to estimating the final fatigue life based on FFM for a given material. Future work will involve aligning this with classical approaches by incorporating various crack propagation mechanisms (e.g., Paris law, exponential models, etc.) within the FFM framework.

II) Extending to multiaxial fatigue: Real-world applications often involve multiaxial loading conditions, where stresses act in multiple directions simultaneously.

III) Material heterogeneity and anisotropy: Composite materials generally exhibit inherent heterogeneity and anisotropy in their mechanical properties. The FFM modeling approach for fatigue damage in composite laminates was developed to work with such material complexities. Future research will involve incorporating other failure mode than brittle or pull out into the FFM model to extend the model for “thick” composite laminate materials under cyclic loading.

IV) Probabilistic and stochastic modeling: Fatigue life is inherently probabilistic due to inherent material variability and manufacturing imperfections. Introducing a probabilistic and/or stochastic paradigm into the FFM framework will enable the provision of fatigue failure predictions that are more realistic and reliable.

V) Variable amplitude loading: Most engineering structures experience variable amplitude loading profiles in real-world service conditions.

Further works related to Phase Field approach to study fatigue failure can be:

I) Computational efficiency and scalability: The “cycle jump” approach presented in this work alleviates the computational cost associated with the growth of complex and highly entangled 3D crack geometries, opening the door to the treatment of even larger volumes and crack networks. Despite this advance, even further improvement will be necessary to carry out large-scale simulations including complex geometries and intricate crack propagation paths. This development will involve exploring adaptive meshing techniques, more efficient solvers, and parallelization strategies, all of which can significantly reduce the computational cost and enable the analysis of more realistic engineering problems.

II) Experimental validation and calibration: Given the wide options for different functions withing Phase Field model, the accuracy of it must be rigorously assessed across various materials, loading conditions, and crack geometries to find the best combination of functions and modeling.

III) Conjugating Phase Field with Machine Learning: Integrating Phase Field methodologies with Machine Learning (ML) techniques can lead to significant acceleration in fatigue life predictions and enhanced efficiency of the overall simulation process.

IV) Conjugating Phase Field with FFM: As discussed in Section 1.8, the FFM can be integrated into Phase Field formulations to replace the internal length with

the material strength. This methodology can be further investigated for applications under fatigue loading.

7.3 Final thoughts

The future of fatigue and fracture analysis in composite structures anticipates a transition towards a comprehensive methodology that can handle complexities in material behavior and loading conditions. This work has endeavored to adapt the FFM model to more complex loading conditions and processes such as fatigue and debonding (with emphasis on the role of friction). Thus, FFM may be recognized as a powerful tool for failure analysis of composite structures that can embrace a spectrum of failure mechanisms. Moreover, by implementing sophisticated computational strategies, notably the Phase Field model, and proposing a methodology to properly validate the approach, one manifests a robust computational capability for analyzing fatigue processes. This approach not only can be used to predict the final life of materials but exploited to allow insight into the various stages of fatigue life, that amplifies the depth and strength of the research. Furthermore, the experimental investigation of the fatigue behavior of notched laminated composites has revealed a number of important insights into the complexity of the relationships that determine fatigue behavior.

All in all, the present work has laid a solid foundation for the application of advanced computational methodologies for analyzing the fatigue and fracture behavior of composite structures. However, the perpetuation for deeper insights and more accurate predictions will necessitate continual exploration and innovation on multiple fronts. By embracing the future directions articulated above researchers can unlock the potential of composite materials and ensure their safe and efficient application in a variety of engineering fields.

References

[1] Wöhler A. Versuche zur Ermittlung der auf die Eisenbahnwagenachsen einwirkenden Kräfte und die Widerstandsfähigkeit der Wagen-Achsen. Zeitschrift Für Bauwes 1860;10:583–614.

[2] Basquin OH. The exponential law of endurance tests. Proc Am Soc Test Mater, vol. 10, 1910, p. 625–30.

[3] Kloth W. Krafte, Beanspruchungen und Sicherheiten in den Landmaschinen. Z-VDI 1936;80:85.

[4] Paris P, Erdogan F. A Critical Analysis of Crack Propagation Laws. J Basic Eng 1963;85:528–33.

[5] Hutchison K. W. J. M. Rankine and the Rise of Thermodynamics. Br J Hist Sci 1981;14:1–26.

[6] Hillerborg A, Modéer M, Petersson P-E. Analysis of crack formation and crack growth in concrete by means of fracture mechanics and finite elements. Cem Concr Res 1976;6:773–81.

[7] Neuber H. Theory of notch stresses: principles for exact calculation of strength with reference to structural form and material. 1961:293p.

[8] Novozhilov V. On a necessary and sufficient condition for brittle strength. Prik Mat Mek 1969;33:212–22.

[9] Pugno NM, Ruoff RS. Quantized fracture mechanics. Philos Mag 2004;84:2829–45.

[10] Carpinteri A. Static and energetic fracture parameters for rocks and concretes. Matériaux Constr 1981;14:151–62.

[11] Blom AF, Hedlund A, Zhao W. Short fatigue crack growth behaviour in Al 2024 and Al 7475. Mech Eng Publ Behav Short Fatigue Cracks, 1986:37–66.

[12] Kinloch AJ, Shaw SJ, Tod DA, Hunston DL. Deformation and fracture behaviour of a rubber-toughened epoxy: 1. Microstructure and fracture studies. Polymer (Guildf) 1983;24:1341–54.

[13] Hazenberg JG, Taylor D, Clive Lee T. Mechanisms of short crack growth at constant stress in bone. Biomaterials 2006;27:2114–22.

[14] Taylor D, Cornetti P, Pugno N. The fracture mechanics of finite crack extension. Eng Fract Mech 2005;72:1021–38.

[15] Susmel L, Taylor D. A novel formulation of the theory of critical distances to estimate lifetime of notched components in the medium-cycle fatigue regime. Fatigue Fract Eng Mater Struct 2007;30:567–81.

[16] Ciavarella M, D'Antuono P, Demelio GP. Generalized definition of "crack-like" notches to finite life and SN curve transition from "crack-like" to "blunt notch" behavior. Eng Fract Mech 2017;179:154–64.

[17] Carpinteri A, Paggi M. A unified interpretation of the power laws in fatigue and the analytical correlations between cyclic properties of engineering materials. Int J Fatigue 2009;31:1524–31.

[18] Cornetti P, Pugno N, Carpinteri A, Taylor D. Finite fracture mechanics: A coupled stress and energy failure criterion. Eng Fract Mech 2006;73:2021–33.

[19] Leguillon D, Yosibash Z. Crack onset at a v-notch. Influence of the notch tip radius. Int J Fract 2003;122:1–21.

[20] Leguillon D. Strength or toughness? A criterion for crack onset at a notch. Eur J Mech 2002;21:61–72.

[21] Sapora A, Cornetti P, Campagnolo A, Meneghetti G. Fatigue limit: Crack and notch sensitivity by Finite Fracture Mechanics. Theor Appl Fract Mech 2020;105:102407.

[22] Sapora A, Cornetti P, Campagnolo A, Meneghetti G. Mode I fatigue limit of notched structures: A deeper insight into Finite Fracture Mechanics. Int J Fract 2021;227:1–13.

[23] Francfort GA, Marigo J-J. Revisiting brittle fracture as an energy minimization problem. J Mech Phys Solids 1998;46:1319–42.

[24] Bourdin B, Francfort GA, Marigo J-J. Numerical experiments in revisited brittle fracture. J Mech Phys Solids 2000;48:797–826.

[25] Mielke A, Roubiček T. Rate-independent systems. Appl Math Sci 2015;193.

[26] Alessi R, Marigo J-J, Vidoli S. Gradient damage models coupled with

plasticity: Variational formulation and main properties. Mech Mater 2015;80:351–67.

[27] Steinke C, Kaliske M. A phase-field crack model based on directional stress decomposition. Comput Mech 2019;63:1019–46.

[28] Tanné E, Li T, Bourdin B, Marigo J-J, Maurini C. Crack nucleation in variational phase-field models of brittle fracture. J Mech Phys Solids 2018;110:80–99.

[29] Pham K, Amor H, Marigo J-J, Maurini C. Gradient Damage Models and Their Use to Approximate Brittle Fracture. Int J Damage Mech 2011;20:618–52.

[30] Ambati M, Gerasimov T, De Lorenzis L. A review on phase-field models of brittle fracture and a new fast hybrid formulation. Comput Mech 2015;55:383–405.

[31] Amor H, Marigo J-J, Maurini C. Regularized formulation of the variational brittle fracture with unilateral contact: Numerical experiments. J Mech Phys Solids 2009;57:1209–29.

[32] Miehe C, Welschinger F, Hofacker M. Thermodynamically consistent phase-field models of fracture: Variational principles and multi-field FE implementations. Int J Numer Methods Eng 2010;83:1273–311.

[33] Freddi F, Royer-Carfagni G. Regularized variational theories of fracture: A unified approach. J Mech Phys Solids 2010;58:1154–74.

[34] Irwin GR. Analysis of Stresses and Strains Near the End of a Crack Traversing a Plate. J Appl Mech 2021;24:361–4.

[35] Rice JR. Mathematical analysis in the mechanics of fracture. Fract an Adv Treatise 1968;2:191–311.

[36] Dugdale DS. Yielding of steel sheets containing slits. J Mech Phys Solids 1960;8:100–4.

[37] Barenblatt GI. The Mathematical Theory of Equilibrium Cracks in Brittle Fracture. In: Dryden HL, von Kármán T, Kuerti G, van den Dungen FH, Howarth L, editors. vol. 7, Elsevier; 1962, p. 55–129.

[38] Otsuka K, Date H. Fracture process zone in concrete tension specimen. Eng Fract Mech 2000;65:111–31.

[39] Huo X, Luo Q, Li Q, Zheng G, Sun G. On characterization of cohesive zone model (CZM) based upon digital image correlation (DIC) method. Int J Mech Sci 2022;215:106921.

[40] Geubelle PH, Baylor JS. Impact-induced delamination of composites: a 2D simulation. Compos Part B Eng 1998;29:589–602.

[41] Dávila CG, Rose CA, Camanho PP. A procedure for superposing linear cohesive laws to represent multiple damage mechanisms in the fracture of composites. Int J Fract 2009;158:211–23.

[42] Needleman A. An analysis of tensile decohesion along an interface. J Mech Phys Solids 1990;38:289–324.

[43] Rose JH, Ferrante J, Smith JR. Universal Binding Energy Curves for Metals and Bimetallic Interfaces. Phys Rev Lett 1981;47:675–8.

[44] Wu J-Y. A unified phase-field theory for the mechanics of damage and quasi-brittle failure. J Mech Phys Solids 2017;103:72–99.

[45] Wu J-Y, Nguyen VP. A length scale insensitive phase-field damage model for brittle fracture. J Mech Phys Solids 2018;119:20–42.

[46] Wells GN, Sluys LJ. A new method for modelling cohesive cracks using finite elements. Int J Numer Methods Eng 2001;50:2667–82.

[47] Wu J-Y, Li F-B. An improved stable XFEM (Is-XFEM) with a novel enrichment function for the computational modeling of cohesive cracks. Comput Methods Appl Mech Eng 2015;295:77–107.

[48] Mandal TK, Nguyen VP, Wu J-Y. Length scale and mesh bias sensitivity of phase-field models for brittle and cohesive fracture. Eng Fract Mech 2019;217:106532.

[49] Molnár G, Doitrand A, Estevez R, Gravouil A. Toughness or strength? Regularization in phase-field fracture explained by the coupled criterion. Theor Appl Fract Mech 2020;109:102736.

[50] Doitrand A, Molnár G, Estevez R, Gravouil A. Strength-based regularization length in phase field fracture. Theor Appl Fract Mech 2023;124:103728.

[51] Cornetti P, Muñoz-Reja M, Sapora A, Carpinteri A. Finite fracture mechanics and cohesive crack model: Weight functions vs. cohesive laws. Int J Solids Struct 2019;156–157:126–36.

[52] Peterson RE. Notch sensitivity. Met Fatigue 1959:293–306.

[53] Taylor D. Geometrical effects in fatigue: a unifying theoretical model. Int J Fatigue 1999;21:413–20.

[54] Susmel L, Taylor D. The theory of critical distances to predict static strength of notched brittle components subjected to mixed-mode loading. Eng Fract Mech 2008;75:534–50.

[55] Smith DJ, Ayatollahi MR, Pavier MJ. The role of T-stress in brittle fracture for linear elastic materials under mixed-mode loading. Fatigue Fract Eng Mater Struct n.d.;24:137–50.

[56] Ayatollahi MR, Torabi AR. Brittle fracture in rounded-tip V-shaped notches. Mater Des 2010;31:60–7.

[57] Susmel L, Taylor D. On the use of the Theory of Critical Distances to predict static failures in ductile metallic materials containing different geometrical features. Eng Fract Mech 2008;75:4410–21.

[58] Ng CT, Susmel L. Notch static strength of additively manufactured acrylonitrile butadiene styrene (ABS). Addit Manuf 2020;34:101212.

[59] Susmel L, Taylor D. The Modified Wöhler Curve Method applied along with the Theory of Critical Distances to estimate finite life of notched components subjected to complex multiaxial loading paths. Fatigue Fract Eng Mater Struct 2008;31:1047–64.

[60] Susmel L, Taylor D. The Theory of Critical Distances to estimate finite lifetime of notched components subjected to constant and variable amplitude torsional loading. Eng Fract Mech 2013;98:64–79.

[61] Susmel L, Taylor D. The Theory of Critical Distances to estimate lifetime of notched components subjected to variable amplitude uniaxial fatigue loading. Int J Fatigue 2011;33:900–11.

[62] Susmel L, Taylor D. Estimating Lifetime of Notched Components Subjected to Variable Amplitude Fatigue Loading According to the Elastoplastic Theory of Critical Distances. J Eng Mater Technol 2015;137.

[63] Susmel L, Taylor D. A critical distance/plane method to estimate finite life of notched components under variable amplitude uniaxial/multiaxial fatigue loading. Int J Fatigue 2012;38:7–24.

[64] Carpinteri A, Cornetti P, Pugno N, Sapora A, Taylor D. A finite fracture

mechanics approach to structures with sharp V-notches. Eng Fract Mech 2008;75:1736–52.

[65] Sapora A, Cornetti P, Carpinteri A, Firrao D. An improved Finite Fracture Mechanics approach to blunt V-notch brittle fracture mechanics : Experimental verification on ceramic , metallic , and plastic materials. Theor Appl Fract Mech 2015;78:20–4.

[66] Carpinteri A, Cornetti P, Sapora A. Brittle failures at rounded V-notches: a finite fracture mechanics approach. Int J Fract 2011;172:1–8.

[67] Priel E, Yosibash Z, Leguillon D. Failure initiation at a blunt V-notch tip under mixed mode loading. Int J Fract 2008;149:143–73.

[68] Sapora A, Cornetti P, Carpinteri A. A Finite Fracture Mechanics approach to V-notched elements subjected to mixed-mode loading. Eng Fract Mech 2013;97:216–26.

[69] Doitrand A, Leguillon D. 3D application of the coupled criterion to crack initiation prediction in epoxy/aluminum specimens under four point bending. Int J Solids Struct 2018;143:175–82.

[70] Weißgraeber P, Leguillon D, Becker W. A review of Finite Fracture Mechanics: crack initiation at singular and non-singular stress raisers. Arch Appl Mech 2016;86:375–401.

[71] Doitrand A, Duminy T, Girard H, Chen X. A review of the coupled criterion. Hal 2023;04023438.

[72] Campagnolo A, Sapora A. A FFM analysis on mode III static and fatigue crack initiation from sharp V-notches. Eng Fract Mech 2021;258:108063.

[73] Shen X, Zeng D, Lu L. Investigating the effect of notch size on critical distance and fatigue limit by coupling the theory of critical distance and finite fracture mechanics. Theor Appl Fract Mech 2022;122:103566.

[74] Liu Y, Deng C, Gong B. Discussion on equivalence of the theory of critical distances and the coupled stress and energy criterion for fatigue limit prediction of notched specimens. Int J Fatigue 2020;131:105326.

[75] Zhu S-P, He J-C, Liao D, Wang Q, Liu Y. The effect of notch size on critical distance and fatigue life predictions. Mater Des 2020;196:109095.

[76] He J-C, Zhu S-P, Liao D, Niu X-P, Gao J-W, Huang H-Z. Combined TCD and HSV approach for probabilistic assessment of notch fatigue considering

size effect. Eng Fail Anal 2021;120:105093.

[77] Leguillon D, Murer S. Fatigue crack nucleation at a stress concentration point. 4th Int. Conf. on" Crack Paths", CP, 2012.

[78] Murer S, Leguillon D. Static and fatigue failure of quasi-brittle materials at a V-notch using a Dugdale model. Eur J Mech - A/Solids 2010;29:109–18.

[79] Cornetti P, Mantič V, Carpinteri A. Finite fracture mechanics at elastic interfaces. Int J Solids Struct 2012;49:1022–32.

[80] Muñoz-Reja M, Cornetti P, Távara L, Mantič V. Interface crack model using finite fracture mechanics applied to the double pull-push shear test. Int J Solids Struct 2020;188:56–73.

[81] Dimitri R, Cornetti P, Mantič V, Trullo M, De Lorenzis L. Mode-I debonding of a double cantilever beam: A comparison between cohesive crack modeling and Finite Fracture Mechanics. Int J Solids Struct 2017;124:57–72.

[82] Muñoz-Reja M, Távara L, Mantič V, Cornetti P. A numerical implementation of the Coupled Criterion of Finite Fracture Mechanics for elastic interfaces. Theor Appl Fract Mech 2020;108:102607.

[83] Müller A, Becker W, Stolten D, Hohe J. A hybrid method to assess interface debonding by finite fracture mechanics. Eng Fract Mech 2006;73:994–1008.

[84] Doitrand A, Leguillon D. Comparison between 2D and 3D applications of the coupled criterion to crack initiation prediction in scarf adhesive joints. Int J Adhes Adhes 2018;85:69–76.

[85] Camanho PP, Erçin GH, Catalanotti G, Mahdi S, Linde P. A finite fracture mechanics model for the prediction of the open-hole strength of composite laminates. Compos Part A Appl Sci Manuf 2012;43:1219–25.

[86] Catalanotti G, Camanho PP. A semi-analytical method to predict net-tension failure of mechanically fastened joints in composite laminates. Compos Sci Technol 2013;76:69–76.

[87] Li X, Xie Z, Zhao W, Zhang Y, Gong Y, Hu N. Failure prediction of irregular arranged multi-bolt composite repair based on finite fracture mechanics model. Eng Fract Mech 2021;242:107456.

[88] Felger J, Stein N, Becker W. Mixed-mode fracture in open-hole composite plates of finite-width: An asymptotic coupled stress and energy approach. Int

J Solids Struct 2017;122:14–24.

[89] Furtado C, Arteiro A, Bessa MA, Wardle BL, Camanho PP. Prediction of size effects in open-hole laminates using only the Young's modulus, the strength, and the R-curve of the 0° ply. Compos Part A Appl Sci Manuf 2017;101:306–17.

[90] Reinoso J, Arteiro A, Paggi M, Camanho PP. Strength prediction of notched thin ply laminates using finite fracture mechanics and the phase field approach. Compos Sci Technol 2017;150:205–16.

[91] Giacomini A. Ambrosio-Tortorelli approximation of quasi-static evolution of brittle fractures. Calc Var Partial Differ Equ 2005;22:129–72.

[92] Bourdin B, Francfort GA, Marigo J-J. The Variational Approach to Fracture. J Elast 2008;91:5–148.

[93] Larsen CJ. Epsilon-stable quasi-static brittle fracture evolution. Commun Pure Appl Math 2010;63:630–54.

[94] Negri M. A comparative analysis on variational models for quasi-static brittle crack propagation 2010;3:149–212.

[95] Borden MJ, Verhoosel C V, Scott MA, Hughes TJR, Landis CM. A phase-field description of dynamic brittle fracture. Comput Methods Appl Mech Eng 2012;217–220:77–95.

[96] Mesgarnejad A, Bourdin B, Khonsari MM. Validation simulations for the variational approach to fracture. Comput Methods Appl Mech Eng 2015;290:420–37.

[97] Nguyen TT, Yvonnet J, Bornert M, Chateau C, Sab K, Romani R, et al. On the choice of parameters in the phase field method for simulating crack initiation with experimental validation. Int J Fract 2016;197:213–26.

[98] Pham K, Marigo J-J, Maurini C. The issues of the uniqueness and the stability of the homogeneous response in uniaxial tests with gradient damage models. J Mech Phys Solids 2011;59:1163–90.

[99] Pham KH, Ravi-Chandar K, Landis CM. Experimental validation of a phase-field model for fracture. Int J Fract 2017;205:83–101.

[100] Wu T, Carpiuc-Prisacari A, Poncelet M, De Lorenzis L. Phase-field simulation of interactive mixed-mode fracture tests on cement mortar with full-field displacement boundary conditions. Eng Fract Mech 2017;182:658–

88.

[101] Boldrini JL, Barros de Moraes EA, Chiarelli LR, Fumes FG, Bittencourt ML. A non-isothermal thermodynamically consistent phase field framework for structural damage and fatigue. Comput Methods Appl Mech Eng 2016;312:395–427.

[102] Caputo M, Fabrizio M. Damage and fatigue described by a fractional derivative model. J Comput Phys 2015;293:400–8.

[103] G. Amendola MF, Golden JM. Thermomechanics of damage and fatigue by a phase field model. J Therm Stress 2016;39:487–99.

[104] Alessi R, Vidoli S, De Lorenzis L. A phenomenological approach to fatigue with a variational phase-field model: The one-dimensional case. Eng Fract Mech 2018;190:53–73.

[105] Carrara P, Ambati M, Alessi R, De Lorenzis L. A framework to model the fatigue behavior of brittle materials based on a variational phase-field approach. Comput Methods Appl Mech Eng 2020;361:112731.

[106] Mesgarnejad A, Imanian A, Karma A. Phase-field models for fatigue crack growth. Theor Appl Fract Mech 2019;103:102282.

[107] Seiler M, Linse T, Hantschke P, Kästner M. An efficient phase-field model for fatigue fracture in ductile materials. Eng Fract Mech 2020;224:106807.

[108] Seiler M, Keller S, Kashaev N, Klusemann B, Kästner M. Phase-field modelling for fatigue crack growth under laser shock peening-induced residual stresses. Arch Appl Mech 2021;91:3709–23.

[109] Ulloa J, Wambacq J, Alessi R, Degrande G, François S. Phase-field modeling of fatigue coupled to cyclic plasticity in an energetic formulation. Comput Methods Appl Mech Eng 2021;373:113473.

[110] Schreiber C, Müller R, Kuhn C. Phase field simulation of fatigue crack propagation under complex load situations. Arch Appl Mech 2021;91:563–77.

[111] Loew PJ, Peters B, Beex LAA. Fatigue phase-field damage modeling of rubber using viscous dissipation: Crack nucleation and propagation. Mech Mater 2020;142:103282.

[112] Lo Y-S, Borden MJ, Ravi-Chandar K, Landis CM. A phase-field model for fatigue crack growth. J Mech Phys Solids 2019;132:103684.

[113] Volkersen O. Die Nietkraftverteilung in zugbeanspruchten Nietverbindungen mit konstanten Laschenquerschnitten. Luftfahrtfor Schung 1938;15:41–7.

[114] Yuan H, Teng JG, Seracino R, Wu ZS, Yao J. Full-range behavior of FRP-to-concrete bonded joints. Eng Struct 2004;26:553–65.

[115] Cornetti P, Carpinteri A. Modelling the FRP-concrete delamination by means of an exponential softening law. Eng Struct 2011;33:1988–2001.

[116] Biscaia HC, Borba IS, Silva C, Chastre C. A nonlinear analytical model to predict the full-range debonding process of FRP-to-parent material interfaces free of any mechanical anchorage devices. Compos Struct 2016;138:52–63.

[117] D'Antino T, Colombi P, Carloni C, Sneed LH. Estimation of a matrix-fiber interface cohesive material law in FRCM-concrete joints. Compos Struct 2018;193:103–12.

[118] D'Antino T, Carloni C, Sneed LH, Pellegrino C. Matrix-fiber bond behavior in PBO FRCM composites: A fracture mechanics approach. Eng Fract Mech 2014;117:94–111.

[119] Calabrese AS, Colombi P, D'Antino T. Analytical solution of the bond behavior of FRCM composites using a rigid-softening cohesive material law. Compos Part B Eng 2019;174:107051.

[120] Colombi P, D'Antino T. Analytical assessment of the stress-transfer mechanism in FRCM composites. Compos Struct 2019;220:961–70.

[121] Mirzaei AM, Corrado M, Sapora A, Cornetti P. Analytical Modeling of Debonding Mechanism for Long and Short Bond Lengths in Direct Shear Tests Accounting for Residual Strength. Materials (Basel) 2021;14.

[122] Mukhtar FM, Shehadah ME. Experimental verification of 2-and 3-D numerical models for bond-slip behavior of CFRP-concrete. Constr Build Mater 2021;287:122814.

[123] Leung CK, Yang Y. Energy-based modeling approach for debonding of FRP plate from concrete substrate. J Eng Mech 2006;132:583–93.

[124] Bažant ZP, Zi G, McClung D. Size effect law and fracture mechanics of the triggering of dry snow slab avalanches. J Geophys Res Solid Earth 2003;108.

[125] CNR-DT 200 R1/2013. Guide for the Design and Construction of Externally Bonded FRP Systems for Strengthening Existing Structures. 2013.

[126] Carpinteri A, Cornetti P, Pugno N, Sapora A, Taylor D. A finite fracture mechanics approach to structures with sharp V-notches. Eng Fract Mech 2008;75:1736–52.

[127] Wang D, Zhang H, Gong B, Deng C. Residual stress effects on fatigue behaviour of welded T-joint: A finite fracture mechanics approach. Mater Des 2016;91:211–7.

[128] Ferrian F, Chao Correas A, Cornetti P, Sapora A. Size effects on spheroidal voids by Finite Fracture Mechanics and application to corrosion pits. Fatigue Fract Eng Mater Struct n.d.;n/a.

[129] Mirzaei AM, Cornetti P, Sapora A. A novel Finite Fracture Mechanics approach to assess the lifetime of notched components. Int J Fatigue 2023:107659.

[130] Susmel L. Multiaxial notch fatigue. Oxford: Woodhead Publishing: Elsevier; 2009.

[131] Castillo E, Fernández-Canteli A, Siegele D. Obtaining S–N curves from crack growth curves: an alternative to self-similarity. Int J Fract 2014;187:159–72.

[132] Sanaei N, Fatemi A. Analysis of the effect of internal defects on fatigue performance of additive manufactured metals. Mater Sci Eng A 2020;785:139385.

[133] Miarka P, Seitl S, Bílek V, Cifuentes H. Assessment of fatigue resistance of concrete: S-N curves to the Paris' law curves. Constr Build Mater 2022;341:127811.

[134] Williams ML. Stress singularities resulting from various boundary conditions in angular corners of plates in extension. J Appl Mech ASME 1952;19:526–8.

[135] Taylor D, Bologna P, Bel Knani K. Prediction of fatigue failure location on a component using a critical distance method. Int J Fatigue 2000;22:735–42.

[136] Ezeh OH, Susmel L. On the notch fatigue strength of additively manufactured polylactide (PLA). Int J Fatigue 2020;136:105583.

[137] DuQuesnay DL, Topper TH, Yu MT. The effect of notch radius on the fatigue notch factor and the propagation of short cracks. Mech Eng Publ Behav Short Fatigue Cracks 1986:323–35.

[138] Mirzaei AM, Ayatollahi MR, Bahrami B, Berto F. A new unified asymptotic stress field solution for blunt and sharp notches subjected to mixed mode loading. Int J Mech Sci 2021;193:106176.

[139] Mirzaei AM, Ayatollahi MR, Bahrami B, Berto F. Elastic stress analysis of blunt V-notches under mixed mode loading by considering higher order terms. Appl Math Model 2020;78:665–84.

[140] Ranjan R, de Oliveira Miranda AC, Hui Guo S, Walbridge S, Gerlich A. Fatigue analysis of friction stir welded butt joints under bending and tension load. Eng Fract Mech 2019;206:34–45.

[141] Nakajima M, Tokaji K, Itoga H, Shimizu T. Effect of loading condition on very high cycle fatigue behavior in a high strength steel. Int J Fatigue 2010;32:475–80.

[142] Berge S. On the effect of plate thickness in fatigue of welds. Eng Fract Mech 1985;21:423–35.

[143] Guo W, Wang CH, Rose LRF. The influence of cross-sectional thickness on fatigue crack growth. Fatigue Fract Eng Mater Struct 1999;22:437–44.

[144] Kim J-K, Shim D-S. The variation in fatigue crack growth due to the thickness effect. Int J Fatigue 2000;22:611–8.

[145] Ezeh OH, Susmel L. Fatigue strength of additively manufactured polylactide (PLA): effect of raster angle and non-zero mean stresses. Int J Fatigue 2019;126:319–26.

[146] Solberg K, Berto F. Notch-defect interaction in additively manufactured Inconel 718. Int J Fatigue 2019;122:35–45.

[147] Barbero EJ. Introduction to composite materials design. CRC press; 2017.

[148] Pipes RB, Wetherhold RC, Gillespie Jr JW. Macroscopic fracture of fibrous composites. Mater Sci Eng 1980;45:247–53.

[149] Mallick PK. Fiber-reinforced composites: materials, manufacturing, and design. CRC press; 2007.

[150] Khandelwal S, Rhee KY. Recent advances in basalt-fiber-reinforced composites: Tailoring the fiber-matrix interface. Compos Part B Eng 2020;192:108011.

[151] Sihn S, Kim RY, Kawabe K, Tsai SW. Experimental studies of thin-ply

laminated composites. Compos Sci Technol 2007;67:996–1008.

[152] Qiao Y, Deleo AA, Salviato M. A study on the multi-axial fatigue failure behavior of notched composite laminates. Compos Part A Appl Sci Manuf 2019;127:105640.

[153] Rajpal D, Mitrotta FMA, Socci CA, Sodja J, Kassapoglou C, De Breuker R. Design and testing of aeroelastically tailored composite wing under fatigue and gust loading including effect of fatigue on aeroelastic performance. Compos Struct 2021;275:114373.

[154] Alam P, Mamalis D, Robert C, Floreani C, Ó Brádaigh CM. The fatigue of carbon fibre reinforced plastics - A review. Compos Part B Eng 2019;166:555–79.

[155] Mirsayar MM. A novel multiscale model for mixed-mode fatigue crack growth in laminated composites. Int J Mech Sci 2023;255:108470.

[156] Shabani P, Taheri-Behrooz F, Maleki S, Hasheminasab M. Life prediction of a notched composite ring using progressive fatigue damage models. Compos Part B Eng 2019;165:754–63.

[157] Afaghi-Khatibi A, Ye L, Mai Y-W. An experimental study of the influence of fibre–matrix interface on fatigue tensile strength of notched composite laminates. Compos Part B Eng 2001;32:371–7.

[158] Mirzaei AH, Shokrieh MM. Evolution of the temperature rise and damage in laminated composites with stress concentration under fatigue loading. Compos Part B Eng 2023;254:110607.

[159] Gaurav A, Singh KK. Fatigue behavior of FRP composites and CNT-Embedded FRP composites: A review. Polym Compos 2018;39:1785–808.

[160] Whitney JM, Nuismer RJ. Stress fracture criteria for laminated composites containing stress concentrations. J Compos Mater 1974;8:253–65.

[161] Caprino G, Halpin JC, Nicolais L. Fracture mechanics in composite materials. Composites 1979;10:223–7.

[162] Camanho PP, Maimí P, Dávila CG. Prediction of size effects in notched laminates using continuum damage mechanics. Compos Sci Technol 2007;67:2715–27.

[163] Pipes RB, Wetherhold RC, Gillespie Jr JW. Notched strength of composite materials. J Compos Mater 1979;13:148–60.

[164] Pipes RB, Gillespie Jr JW, Wetherhold RC. Superposition of the notched strength of composite laminates. Polym Eng Sci 1979;19:1151–5.

[165] Belmonte HMS, Manger CIC, Ogin SL, Smith PA, Lewin R. Characterisation and modelling of the notched tensile fracture of woven quasi-isotropic GFRP laminates. Compos Sci Technol 2001;61:585–97.

[166] Khondker OA, Herszberg I, Hamada H. Measurements and prediction of the compression-after-impact strength of glass knitted textile composites. Compos Part A Appl Sci Manuf 2004;35:145–57.

[167] Huh JS, Hwang W. Fatigue life prediction of circular notched CFRP laminates. Compos Struct 1999;44:163–8.

[168] Taylor D. The Theory of Critical Distances:A New Perspective in Fracture Mechanics. Oxford: Elsevier; 2007.

[169] Morgan D, Quinlan S, Taylor D. Using the theory of critical distances to predict notch effects in fibre composites. Theor Appl Fract Mech 2022;118:103285.

[170] Ibáñez-Gutiérrez FT, Cicero S. Fracture assessment of notched short glass fibre reinforced polyamide 6: An approach from failure assessment diagrams and the theory of critical distances. Compos Part B Eng 2017;111:124–33.

[171] Ibáñez-Gutiérrez FT, Cicero S, Carrascal IA, Procopio I. Effect of fibre content and notch radius in the fracture behaviour of short glass fibre reinforced polyamide 6: An approach from the Theory of Critical Distances. Compos Part B Eng 2016;94:299–311.

[172] Mirzaei AM, Mirzaei AH, Shokrieh MM, Sapora A, Cornetti P. Fatigue life assessment of notched laminated composites: Experiments and modelling by Finite Fracture Mechanics. Compos Sci Technol 2024;246:110376.

[173] Galos J. Thin-ply composite laminates: a review. Compos Struct 2020;236:111920.

[174] Konish HJ, Whitney JM. Approximate Stresses in an Orthotropic Plate Containing a Circular Hole. J Compos Mater 1975;9:157–66.

[175] Sapora A, Torabi AR, Etesam S, Cornetti P. Finite Fracture Mechanics crack initiation from a circular hole. Fatigue Fract Eng Mater Struct 2018;41:1627–36.

[176] Catalanotti G, Salgado RM, Camanho PP. On the Stress Intensity Factor of

cracks emanating from circular and elliptical holes in orthotropic plates. Eng Fract Mech 2021;252:107805.

[177] Newman Jr JC. A nonlinear fracture mechanics approach to the growth of small cracks. 1983.

[178] Tada H, Paris PC, Irwin GR. The stress analysis of cracks. Handbook, Del Res Corp 1973;34.

[179] Bao G, Ho S, Suo Z, Fan B. The role of material orthotropy in fracture specimens for composites. Int J Solids Struct 1992;29:1105–16.

[180] Suo Z, Bao G, Fan B, Wang TC. Orthotropy rescaling and implications for fracture in composites. Int J Solids Struct 1991;28:235–48.

[181] Mirzaei AH, Shokrieh MM, Saeedi A. Fatigue behavior of laminated composites with embedded SMA wires. Compos Struct 2022:115753.

[182] Roundi W, El Mahi A, El Gharad A, Rebière J-L. Experimental and numerical investigation of the effects of stacking sequence and stress ratio on fatigue damage of glass/epoxy composites. Compos Part B Eng 2017;109:64–71.

[183] Green BG, Wisnom MR, Hallett SR. An experimental investigation into the tensile strength scaling of notched composites. Compos Part A Appl Sci Manuf 2007;38:867–78.

[184] Harris CE, Morris DH. Role of delamination and damage development on the strength of thick notched laminates. ASTM International; 1985.

[185] Vaidya RS, Klug JC, Sun CT. Effect of ply thickness on fracture of notched composite laminates. AIAA J 1998;36:81–8.

[186] Standard test method for tensile properties of polymer matrix composite materials. ASTM D3039/DM 2008;3039.

[187] Standard test method for in-plane shear response of polymer matrix composite materials by tensile test of a ±45° laminate. ASTM D3171-22 2018.

[188] Standard test methods for constituent content of composite materials. ASTM D3171-22 2022.

[189] Ambrosio L, Tortorelli VM. Approximation of functional depending on jumps by elliptic functional via t-convergence. Commun Pure Appl Math

1990;43:999–1036.

[190] Grossman-Ponemon BE, Mesgarnejad A, Karma A. Phase-field modeling of continuous fatigue via toughness degradation. Eng Fract Mech 2022;264:108255.

[191] Freddi F, Mingazzi L. Adaptive mesh refinement for the phase field method: A FEniCS implementation. Appl Eng Sci 2023;14:100127.

[192] Gupta A, Krishnan UM, Mandal TK, Chowdhury R, Nguyen VP. An adaptive mesh refinement algorithm for phase-field fracture models: Application to brittle, cohesive, and dynamic fracture. Comput Methods Appl Mech Eng 2022;399:115347.

[193] Hennig P, Ambati M, De Lorenzis L, Kästner M. Projection and transfer operators in adaptive isogeometric analysis with hierarchical B-splines. Comput Methods Appl Mech Eng 2018;334:313–36.

[194] Ambati M, Heinzmann J, Seiler M, Kästner M. Phase-field modeling of brittle fracture along the thickness direction of plates and shells. Int J Numer Methods Eng 2022;123:4094–118.

[195] Olesch D, Kuhn C, Schlüter A, Müller R. Adaptive numerical integration of exponential finite elements for a phase field fracture model. Comput Mech 2021;67:811–21.

[196] Seleš K, Aldakheel F, Tonković Z, Sorić J, Wriggers P. A general phase-field model for fatigue failure in brittle and ductile solids. Comput Mech 2021;67:1431–52.

[197] Heinzmann J, Carrara P, Ambati M, Mirzaei AM, De Lorenzis L. An adaptive acceleration scheme for phase-field fatigue computations. Comput Mech n.d.

[198] Ayatollahi MR, Rashidi Moghaddam M, Berto F. T-stress effects on fatigue crack growth – Theory and experiment. Eng Fract Mech 2018;187:103–14.